The Pennsylvania State University
The Graduate School

MESHFREE VISCOELASTIC MODELING: TOWARD NUMERICAL SIMULATION OF PRINTING CONCRETE STRUCTURES

A Thesis in
Civil Engineering
by
Guang Chen

Submitted in Partial Fulfillment
of the Requirements
for the Degree of

Master of Science

August 2019

The thesis of Guang Chen was reviewed and approved* by the following:

Michael Hillman
Assistant Professor of Civil Engineering
Thesis Co-Advisor

Aleksandra Radlinska
Associate Professor of Civil Engineering
Thesis Co-Advisor

Pinlei Chen
Assistant Professor of Civil Engineering

Patrick Fox
Professor of Civil Engineering
Head of the Department of Civil and Environmental Engineering

*Signatures are on file in the Graduate School.

Abstract

The conventional way of construction in building industry has many disadvantages, for example, the environmental pollution, massive energy consumption, less customization, and the intense human labor involved. A new, more efficient way of manufacturing construction materials could reduce time, cost and labor intensity, while providing design freedom for complex architectural forms. Towards this end, three dimensional (3D) printing, or additive manufacturing of concrete structures offers great potential.

This technology however is still in its relative infancy, and further research is needed in order to bring this technology to the market. Specifically, the materials aspect of 3D printing pose many open research questions, such as rheological properties of the concrete that enabling effective pumping and printing, while also hardening quickly enough to support the weight of subsequent layers. In order to address these questions, two approaches can be employed: experiment and mathematical modeling. While an experiment approach alone is time consuming and costly, numerical simulation properly validated with experiments offers a far less costly and more effective alternative.

To numerically model the behavior of concrete at fresh or solidified state, a viscoelastic constitutive law for both small-strain and finite-strain are introduced based on the generalized Maxwell model. In the solidified state, a small strain version of the viscoelastic constitutive relation can be used to model phenomena like stress relaxation and creep. While for fresh state mixture, the large strain version can model the finite deformation present in the deposition process, and interface evolution in 3D printing. However, careful selection of a numerical framework is necessary, since in the traditional finite element approach, large deformations can cause mesh distortion and entanglement, and topological changes in the domain (free surface formation, closure) require computationally intensive remeshing. Meshfree methods on the other hand, do not require mesh and can deal with these aforementioned problems easily. A numerical framework based on the meshfree reproducing kernel particle method (RKPM) is developed in this work to model

the deposition process.

Several numerical examples are tested to verify the developed computational framework. It is observed that the numerical results agree well with reference results, which indicates a strong potential for the effectiveness of the numerical framework for viscoelastic modeling of extremely large deformation problems such as deposition of concrete.

Table of Contents

List of Figures

List of Tables

Acknowledgments

I would like to give my sincerely gratitude to my thesis co-advisors, Professor Michael Hillman and Professor Aleksandra Radlinska. Professor Hillman taught and trained me a lot in computational mechanics and meshfree methods. Professor Radlinska taught me much about ceramic materials and how to balance work and life. All of these is good experience and great fortune to me.

I would also like to thank Professor Pinlei Chen for serving as my thesis committee member and her suggestions on my thesis. In addition, I learned much about finite element method and advanced structural mechanics from her.

In this journey, great help is received from my colleagues who are Joe, Chris, and Sam and my friends Max, and Mehrshad. My acknowledgement also goes to them.

The support of this work by the L. Robert and Mary L. Kimball Early Career Professorship and gift by AutoDesk are greatly acknowledged.

Chapter 1 Introduction

1.1 Motivation

There is a wide consensus that current economic and industrial development is proceeding in an unsustainable manner. Population growth and urbanization pose a great pressure on the world's resources and environment in the twentieth century, as they contribute to a tremendous expansion of energy use [9]. This phenomenon is continuing, especially in developing countries. Thus, the call for more sustainable development is growing worldwide.

This trend is particularly relevant to the construction industry, as conventional construction techniques release large amounts of carbon dioxide (CO_2) into the atmosphere, which is the main greenhouse gas. Not only great amount of CO_2 emissions are produced, but waste is also produced in the form of waste water and excess building materials. Waste water is serious environmental problem which can result in severe water shortage [10], which is often overlooked.

Conventional construction is also labor insensitive due to the process of molding and demolding. Traditional construction also provides limited design freedom for architecture consisting of complex shapes.

A relatively new way of manufacturing, called additive manufacturing (AM),is becoming increasingly popular throughout the world. In contrast to subtractive manufacturing (SM) techniques such as milling and formative manufacturing (FM) (e.g. casting), additive manufacturing uses no formwork and produces little waste since the material is placed where it only needs to be for the final product. This technique has also been termed digital fabrication, digital manufacturing, rapid

prototyping, or three-dimensional (3D) printing.

Additive manufacturing is characterized by extruded, successive and layered printing of materials. Additive manufacturing technology is being increasingly adopted across various fields, from aerospace and automotive manufacturing, medical devices, and food science for aesthetics [3]. In recent decades, this new technology has been introduced to construction field for concrete structures.

3D printing of concrete and cementitious material, known as freeform fabrication has great potential to address these problems. Like other AM techniques it produces near zero waste: by using 3D printing, civil engineers can optimize structures before they are manufactured so that the final print uses a minimum amount of materials.

Presently, this technology is poorly understood, and before it can used in industry applications, identifying a printable concrete is required: the concrete mixture must simultaneously yield workability, low drying shrinkage and sufficient strength, while also avoiding weak bonds between printed layers.

Among these properties, the rheological properties are key for the actual process of printing the concrete to be successful. Laboratory experiments may identify a proper mix for desired properties, yet because of the numerous parameters involved, the possible combinations makes this approach virtually intractable. Numerical simulation combined with experimentation is potentially a far more effective approach to study these problems than a pure experimental trial-and-error approach. However, little work has been done to study this problem computationally. Thus in order to bring this technology to fruition, it is of essential importance to build a numerical framework to study this problem.

1.2 Objective and outline

The interdisciplinary nature of modeling concrete printing is illustrated in Figure 1.1. The three main ingredients are indicated, namely chemical hydration, rheology, and the computational approach. Strictly speaking, multiscale modeling should be carried out to consider all these factors.

The chemical reaction of hydration governs the development of microstructures of concrete mixtures and thus determines the macroscale hardening process and the material behaviors such as viscosity and stiffness. Simulation of hydration in

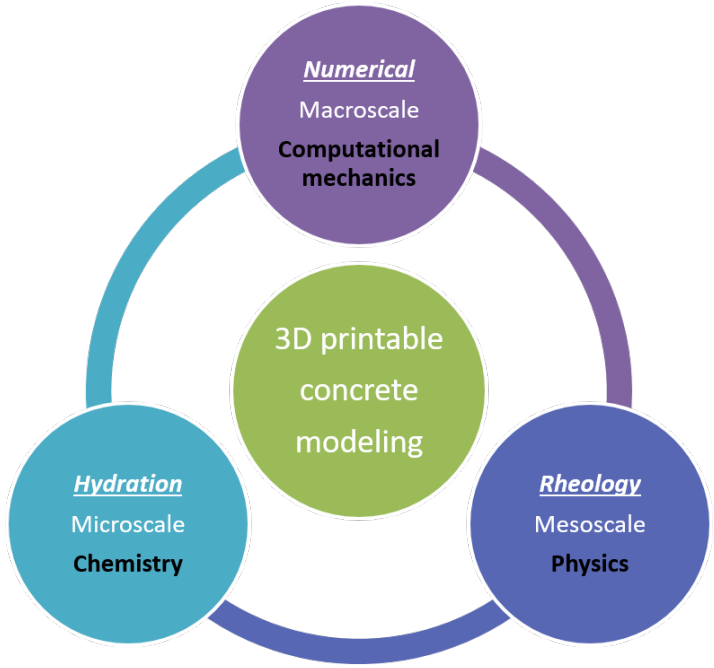

Figure 1.1: Interdisciplinary relation involved in the concrete printing modeling.

concrete has been studied [11–15], and can produce macroscale material parameters, and offers a physics-based approach rather than phenomenological or empirical. However, multiscale modeling is a computationally intensive and complex approach requiring development of a comprehensive framework for simulation. Not only does this involve the chemical processes, but it also requires the development of a numerical method capable of simulating the deposition process.

In this work, a continuum mechanics-based macroscale modeling approach is developed to this end. That is, a numerical framework is presented which has the potential to model 3D printing of concrete mixtures. In consideration of extremely large deformations involved and the presence of surface generation and closure in concrete printing, a meshfree method called reproducing kernel particle method [16] is chosen as the numerical method. Considering that concrete mixtures go through a viscous dominant phase to a solid dominant phase, an viscoelastic material law in integral form based on the generalized Maxwell model [17] is chosen as the constitutive law.

The remainder of this thesis is organized as follows. A literature review of the basics of concrete is presented in Chapter 2, which is followed by a general

overview of 3D printing with emphasis on 3D concrete printing and the challenges involved. Since the constitutive relation of the concrete flow is the essential part of concrete printing modeling, a comprehensive review of the behavior of concrete-like materials will also be given in Chapter 2. In Chapter 3, the reproducing kernel particle method will be described, and several numerical examples will be showed to verify the accuracy of this method, as well as examine the effect of the choices in the formulation on accuracy of the solution. Chapter 4 presents a small-strain meshfree framework for viscoelastic analysis where several benchmark problems are solved with good accuracy. A finite-strain version of the meshfree viscoelastic modeling is then developed in Chapter 5, with the aim toward the verifying a numerical framework for simulation of concrete printing. Finally, a concluding remarks and summary will be presented in Chapter 6.

Chapter 2
Literature review

2.1 Concrete construction

Concrete is the most widely used man-made material in the world, with about 2 billion tonnes used every year [5]. It is a mixture, made up of portland cement, fine and/or coarse aggregates, water, chemical and mineral admixtures, and up to 8% air in volume. Portland cement is created by burning clay and limestone into clinker material, while adding approximately 5% gypsum in mass. Aggregate is obtained either by cracking stone (coarse aggregate) or from river sand (fine aggregate).

There are many advantages of concrete as a construction material. The raw materials to produce concrete are cheap and readily available almost everywhere around the world. Structures built by concrete can obtain high strength. Concrete is also an inert material that is fire resistant.

Although concrete has many attractive properties in construction, it still bears some disadvantages. Producing the raw materials for example, is energy-intensive, and at the same time a large amounts of carbon dioxide are emitted. It is reported that 1 ton of clinker produced releases 1 ton of CO_2 into the atmosphere.

Since the chemical and mechanical properties are crucial for 3D printable concrete, a review is presented in detail in the following text. First, the chemistry is reviewed briefly, which is the basis of microscale physics of the hydration reaction. The rheology, or mechanical properties of concrete is then reviewed.

2.1.1 Chemistry of concrete

After the raw materials to form concrete are mixed together, a chemical reaction, called hydration reaction occurs, and the fresh concrete begins to harden. Through the so-called curing process, the concrete solidifies and becomes solid.

Before the chemical composition is presented, it is convenient to introduce the notation of oxides [18]. The shorthand forms of the chemical formula are listed in Table 2.1. The basic chemical compositions of concrete are tricalcium silicate ($3\,CaO{\cdot}SiO_2$, or C_3S), dicalcium silicate ($2\,CaO{\cdot}SiO_2$, or C_2S), tricalcium aluminate ($3\,CaO \cdot Al_2O_3$, or C_3A), and tetracalcium aluminoferrite ($4\,CaO \cdot Al_2O_3 \cdot Fe_2O_3$, or C_4AF).

These main components react with water to form the gel which is carbon silicate hydrate (C−S−H). The reaction equations forming silica gel are as follows:

$$2\,C_2S + 9\,H \longrightarrow C_3S_2H_8 + CH \tag{2.1}$$

$$2\,C_3S + 11\,H \longrightarrow C_3S_2H_8 + 3\,CH \tag{2.2}$$

where $C_3S_2H_8$ is the main product of hydration reaction, the composition of which is variable. It is an amorphous porous gel which is stable in water and acts as the "glue" to combine aggregates together.

The other two ingredients react with water and gypsum ($C\overline{S}H_2$) to generate other products. For C_3A:

$$C_3A + 3\,C\overline{S}H_2 + 26\,H \longrightarrow C_6A\overline{S}_3H_{32} \tag{2.3}$$

$$2\,C_3A + C_6A\overline{S}_3H_{32} + 4\,H \longrightarrow 3\,C_4A\overline{S}H_{12} \tag{2.4}$$

where $C_6A\overline{S}_3H_{32}$ is ettringite, and $C_4A\overline{S}H_{12}$ is called monosulfoaluminate.

For C_4AF:

$$C_4AF + 3\,C\overline{S}H_2 + 21\,H \longrightarrow C_6(A,F)\overline{S}_3H_{32} + (F,A)H_3 \tag{2.5}$$

$$C_4AF + C_6(A,F)\overline{S}_3H_{32} + 7\,H \longrightarrow 3\,C_4(A,F)\overline{S}H_{12} + (F,A)H_3 \tag{2.6}$$

In these equations, the composition of iron oxide and alumina is not fixed, so there is no particular chemical formula for them.

Table 2.1: Typical oxide and its shorthand notation.

Oxide	Common name	Shorthand notation
CaO	lime	C
SiO_2	silica	S
Al_2O_3	alumina	A
Fe_2O_3	ferric oxide	F
CO_2	carbon dioxide	$\overline{C}$
SO_3	sulfur trioxide	$\overline{S}$
H_2O	water	H

2.2 3D printing of concrete and cementitious materials

According to American Society of Testing and Materials (ASTM) definition [19], 3D printing refers to the process of joining materials to make objects from 3D model data, usually layer upon layer. In this definition, the important features of 3D printing are highlighted: the additive process of manufacturing (in contrast to the formative and subtractive way) connected with a computer-aided design (CAD) model to generate the geometry of slices for layered manufacturing.

The typical processes of 3D printing are: (1) creating a 3D model using CAD software; (2) slicing the model into a series of images, refereed to as 2.5D, since each layer has a constant height; and, (3) output of the information to a printer in order to print the 2.5D images. Post-processing is employed when supports or other materials need to be removed after the printing process.

3D printing itself involves materials, design methods, and manufacturing processes. As such, there is an inter-dependent relationship between the final product, properties of the material, overall design, and the manufacturing process [20]. A 3D printing process must consider all these factors so that an optimal product can be obtained.

3D printing of concrete or cementitious materials, also known as freeform fabrication, is in its infancy but offers great potential. It produces near zero waste since it is an additive manufacturing construction technology: materials are only placed where they need to be in their final form. It also provides design freedom, and can be customized widely. Importantly, by using 3D printing, civil engineers

can also optimize the structure before manufacturing it so that the final print uses the minimum amount of materials necessary. However, before this technology can fully be realized in the building construction industry, several issues need to be addressed. In this section, the deposition technology of concrete materials and the challenges of 3D printing in concrete materials are reviewed.

2.2.1 Deposition of concrete and cementitious materials

The previous section is the general review of deposition technologies used for a wide range of materials, not limited to concrete and ceramic materials. In this section, existing deposition technologies for concrete materials are reviewed, which are material extrusion, powder bed printing, and slip-forming.

Material extrusion is perhaps the most popular technique, for example, the so called Contour Crafting (CC) [1] in University of Southern California in the US, the Concrete Printing (CP) [2, 21] in Loughborough University in the United Kingdom, and 3D Concrete printing (3DCP) [3] in Eindhoven University of Technology in the Netherlands, to name a few. The basic components of this type of technology include a printing head to extrude the material, a mixing system to produce mixtures, a pump system to transport the material, a gantry or robot system to move the printer head, and a control system to control the process.

Figure 2.1, Figure 2.2, and Figure 2.3 depict the processes of Contour Crafting, Concrete Printing, and 3D Concrete Printing, respectively.

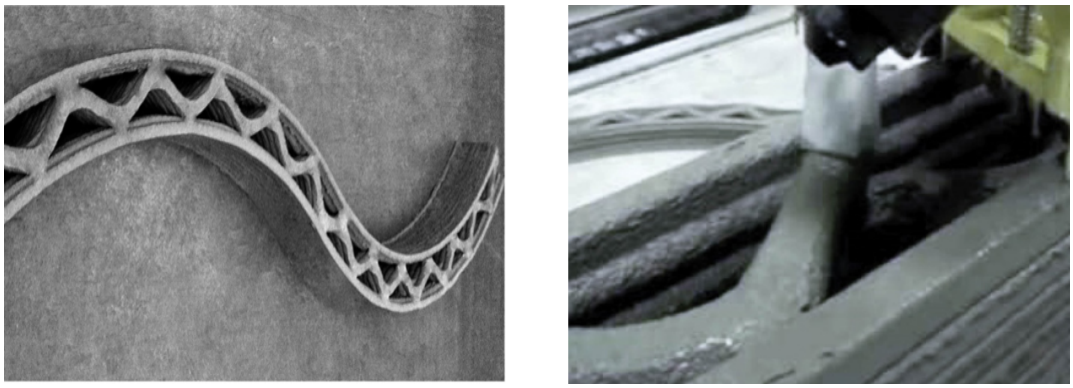

(a) Printed structure (b) Extrusion detail

Figure 2.1: Contour Crafting by USC [1].

(a) Printed structure

(b) Detail of the printed structure

Figure 2.2: Concrete Printing by Loughborough University [2].

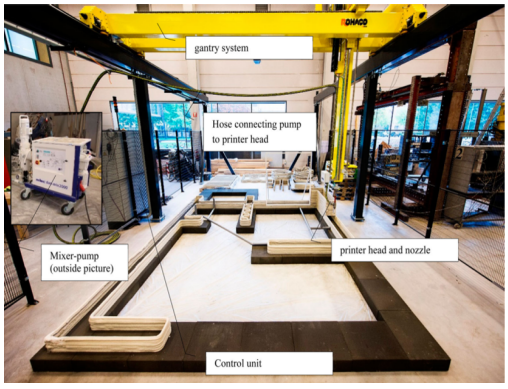

(a) Printing system

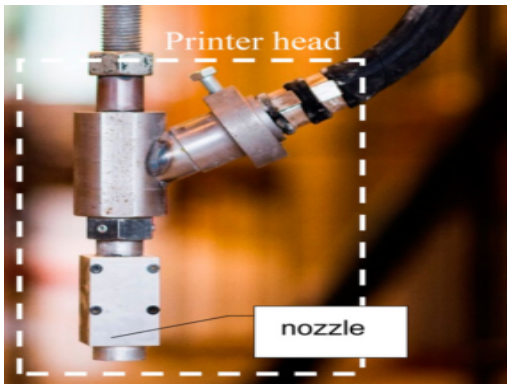

(b) Nozzle, the diameter of which is 9mm and printer head.

Figure 2.3: 3D Concrete Printing by TU/e [3].

Powder bed is another type of deposition technology, for example, the process used by D-shape [4]. Compared to extrusion-based technology, it has several differences. First, it can produce more complex structures since the remnant material serves as the supporting material. Thus there is no need to use supports for overhanging structures. It does however require much more material than the final structure consists of. Extra effort is also required to remove the remaining material. Finally, the surface is also polished after completion. Figure 2.4 shows the process of printing using the D-shape technology.

Slip-forming is the approach taken by ETH, Zurich [5]. This process employs a moving mold to cast the concrete, in which the reinforcement is included. Figure 2.5 shows the process of slipforming.

(a) Coarse prototype (b) Completed structure

Figure 2.4: Complex structures produced by the D-shape technology [4].

2.2.2 Challenges in 3D printing of concrete and cementitious materials

Due to the phase change of concrete, there exists both a fresh state and hardened state. According to Le et. al. [21], the fresh state of concrete should fulfill four standards: extrudability, workability, open time, and buildability. In the hardened state, concrete should meet the following standards: sufficient compressive strength, flexual strength, and tensile bond strength etc. [2].

The aforementioned four standards for the fresh state can be summarized as follows:

- extrudability: the capacity of concrete to pass through the necessary pipes and nozzles at the printing head.
- workability: the capacity to cast.
- open time: the time period in which the fresh mixture maintains workability and extrudability, or it is not too dry or too wet.
- buildability: the capacity of the printed filaments to be built up in vertical direction.

In other words, the material should be fluid at first to enable pumping and printing, and later it should be stiff enough to maintain the weight of subsequent layers. That is to say, there is a critical time window between consecutive printed

Figure 2.5: Printing a structure by slipforming [5].

layers: the time gap between layers needs to fall into this range. In addition, it should have sufficient strength since presently there is no reinforcement used in printed structures. Finally, as there is no mold involved, the surface area is relatively large, and the water can more easily to evaporate into the atmosphere. Thus, the material should also have low drying shrinkage, or a special curing condition should be provided.

From the standpoint of printing process, the tool path should also be considered. If the tool path is different, even for the same material and geometry, the performance of the final structure may be different. As a result, an optimal printing tool path should be considered and designed.

Since there are many factors involved, identification of the optimal process parameters in general is difficult due to the many possible permutations.

2.3 Rheological models and simulations involving concrete flow

Concrete has been termed a "miracle" material. In a fresh state, it can be considered as a dense suspension [22] and can, for example, be treated as a non-Newtonian fluid with the Bingham fluid model [23–26]. As curing process continues, it solidifies and exhibits the behavior of a solid. Obviously, there is a transition stage in which concrete has both fluid and solid characteristics, which can be described by rheology, which which is the study of materials that are characterized by both the behavior of Non-Newtonian fluids and plastic solids. A schematic of this type of behavior is shown as Figure 2.6.

Modeling this material behavior correctly is critical for effective numerical simulation. As indicated in Figure 2.6 , the stage of the concrete decides what constitutive law to use. It may be treated as a fluid when at fresh state, or a solid when at solidified state, or in between. It is reported that the first simulation of fresh concrete flow can be traced back to 1992 [27]. Since then, academic interest has grown, and in recent decades, large number of publications on fresh concrete flow have emerged. In a majority of the literature, fresh concrete is modeled as a non-Newtonian fluid. A commonly used model is the Bingham fluid model which contains two important parameters, the yield stress τ_y and plastic viscosity η. Another popular material law used is the Herschel & Bulkley (H-B) model [28], which is a Bingham-based power law.

In term of computational techniques, various computational fluid dynamics (CFD) methods have been used to model concrete flow. Patzak and Bittnar [29] used the finite element method (FEM) to study the dam break problem, the slump test, and an L-box test of concrete. They adopted the volume of fraction (VOF) method to track the free surfaces involved. Mechtcherine et.al. [30] gave a detailed description of theory and application of the discrete element method (DEM) to study the problem. In a combined effort by Roussel et.al. [27], the particle finite element method (PFEM), lattice Boltzmann method (LBM), and distinct element method (DEM) were employed out to study the slump test and the channel flow test of concrete.

Since the chosen material law is an essential component of numerical simula-

tion of concrete flow, in this section, various rheological models used for concrete simulation are presented, including viscoelastic models and viscoplastic models.

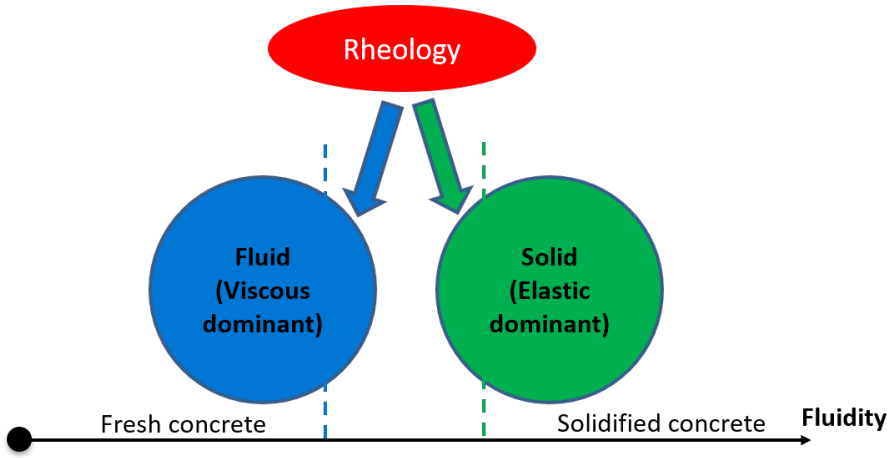

Figure 2.6: Physical models for concrete at different states.

2.3.1 Non-Newtonian fluid

A fundamental characteristic of fluids is that they cannot sustain shear stress at rest, which can be observed from, for example, Newton's law which describes a linear relation between shear stress τ and strain rate $\dot{\varepsilon}$ (or engineering strain rate $\dot{\gamma}$) as $\tau = 2\eta\dot{\epsilon} = \eta\dot{\gamma}$ where η is a constant material parameter called dynamic viscosity. Non-Newtonian fluids are the fluids that do not obey this law. Namely, for non-Newtonian fluids, the shear stress is not linearly proportional to the shear rate.

The laws between shear stress and shear rate for fluids are called constitutive laws, which can be divided into time-independent and time-dependent laws.

Shear thinning and shear thickening fluids are typical examples of time-independent Non-Newtonian fluids. In shear thinning fluids, such as toothpaste, the viscosity decreases as shear rate increases. In shear thickening fluids, such as cornstarch, the opposite is true, with viscosity increasing as the shear rate increases. The shear stress- shear rate relation for these two types are shown in Figure 2.7, along with Newtonian fluids for reference.

Viscoplastic and viscoelastic models are also employed for time-independent materials. Viscoplastic materials, as the name indicates, are materials that behave

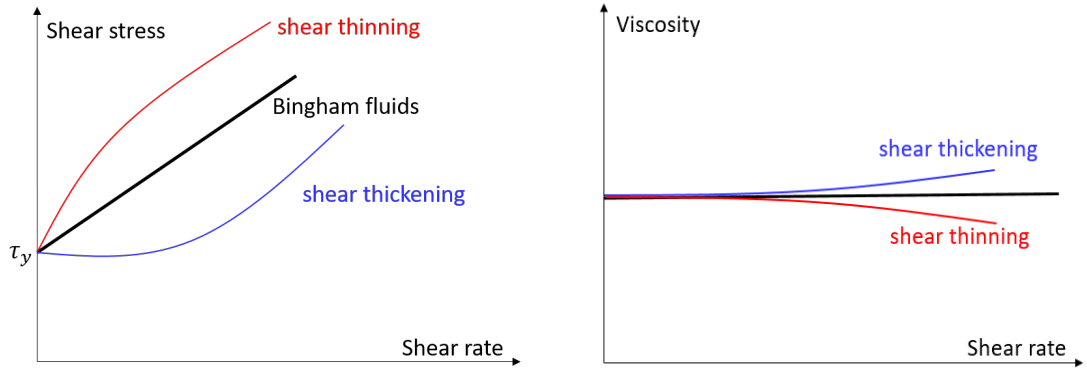

(a) Shear stress and shear rate relation (b) Viscosity and shear rate relation

Figure 2.7: Relations between shear stress, viscosity and shear rate, for various models

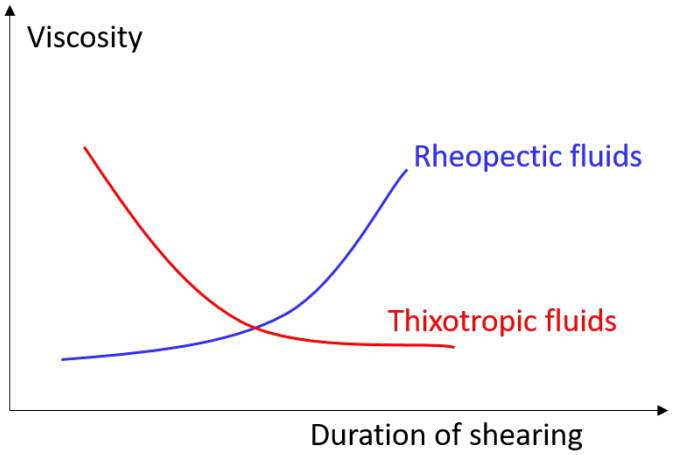

Figure 2.8: Schematic of time dependent fluids.

with both viscous and plastic characteristics, while viscoelastic materials exhibit viscous and elastic characteristics. For viscoplastic fluids, there exists a so-called yield stress, for which when the shear stress exceeds this threshold, the material behaves like a fluid.

For fluids with time dependent constitutive laws, they can be divided into thixotropic and rheopectic fluids. In thixotropic fluids, the viscosity decreases as the duration of shearing increases, while in rheopectic fluids, the opposite is true. The relation between viscosity and duration of shearing for these types of fluids is shown in Figure 2.8.

2.3.2 Plastic solid and viscoplastic solids

Solids can also be divided into elastic solids and plastic solids. Purely elastic solids fully recover the initial unloaded state after the applied force is removed. In plastic solids, irreversible deformations can occur with loading, in contrast. Depending on whether the materials are rate-independent or rate-dependent, plastic solids can be modeled by elastoplastic laws or viscoplastic laws.

Elastoplastic response can be derived using a one dimensional analogy to an elastic spring and a Coulomb friction element [31]. For a viscoplastic material, a viscous damper in parallel with the friction device can be considered to derive the material law [31].

Bingham model is possibly the most popular for simulating concrete flow, which is a viscoplastic solid law. The schematic physical model is shown in Figure 2.9. Recall that in this model, a critical stress exists called yield stress: only when the shear stress exceeds this stress can the material flow. This model can be expressed as the following relation between stress τ, yield stress τ_y , and shear rate $\dot{\gamma}$:

$$\tau = \begin{cases} \tau_y + \eta\dot{\gamma} & \text{if} \quad \tau > \tau_y \\ G\gamma & \text{if} \quad \tau \leq \tau_y \end{cases} \tag{2.7}$$

where G is the elastic modulus of the spring.

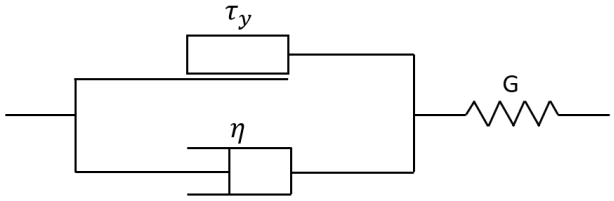

Figure 2.9: Schematic of viscoplastic model.

2.3.3 Viscoelastic solid

For materials with both solid and fluid characteristics like concrete, the viscoelastic solid can also be used for modeling. Usually the rheological model consists of elastic springs and viscous dampers, which are used to derive the constitutive relation from a one-dimensional analogy, for example, the Maxwell model [17], the

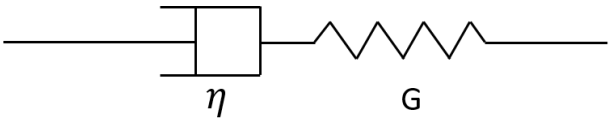

Figure 2.10: Schematic of Maxwell model.

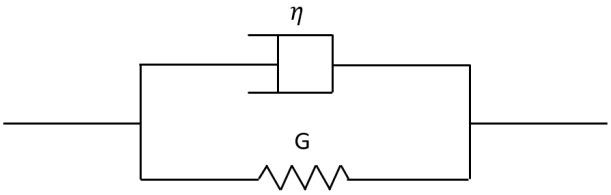

Figure 2.11: Schematic of Kelvin model.

Kelvin model [32], the standard solid model [33], and the Oldroyd-B model [34]. The schematic plot for these models are shown in Figure 2.10, 2.11, 2.12, 2.13, respectively. The constitutive models derived can be used to simulate creep and relaxation.

The Maxwell model can be interpreted as a viscous damper and an elastic spring in a serial arrangement (see Figure 2.10), which is usually used to model polymers.

For the Maxwell model, the following equations hold:

$$\begin{aligned} \varepsilon &= \varepsilon_e + \varepsilon_v \\ \tau &= 2G\varepsilon_e = 2\eta\dot{\varepsilon}_v \end{aligned} \tag{2.8}$$

where ε is the total strain and ε_v, ε_e are the viscous strain and elastic strain, respectively. τ is the shear stress. η and G are dynamic viscosity and shear modulus for the elements. Using engineering strain rate notation, this equation is

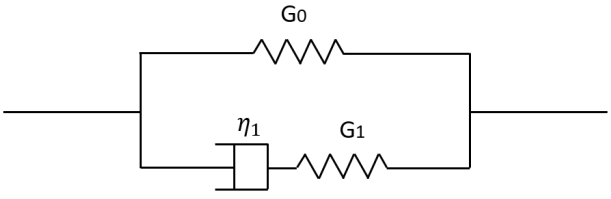

Figure 2.12: Schematic of standard solid model.

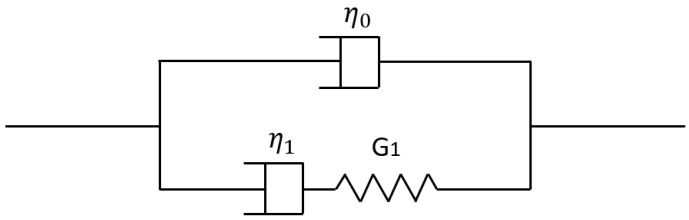

Figure 2.13: Schematic of Oldroyd-B model.

rewritten as:

$$\tau + \lambda\dot{\tau} = \eta\dot{\gamma} \tag{2.9}$$

where $\lambda = \frac{\mu}{G}$ is the relaxation time of Maxwell model.

The Maxwell model can be extended to the so-called generalized Maxwell model by employing a linear spring in parallel with many Maxwell elements [17], which is adopted as the constitutive law for the computational modeling in present work.

Similar equations can be derived following the same procedures and analogies as in the Maxwell model, and are briefly summarized as follows.

For Kelvin model, the following relations hold:

$$\begin{aligned} &\varepsilon_e = \varepsilon_v = \varepsilon \\ &\tau = 2G\varepsilon_e + 2\eta\dot{\varepsilon}_v \end{aligned} \tag{2.10}$$

For standard solid model, the following relations hold:

$$\begin{aligned} &\tau = \tau_0 + \tau_1 \\ &\tau_0 = 2G_0\varepsilon \\ &\tau_1 + \lambda\dot{\tau}_1 = \eta_1\dot{\gamma} \end{aligned} \tag{2.11}$$

where ε is the total strain of the model, τ_0 the shear stress on the elastic spring, and τ_1 the shear stress on the bottom Maxwell element, which can be solved by Equation 2.9. The relaxation time here is $\lambda = \frac{\eta_1}{G_1}$.

Oldroyd-B model is comprised of the Maxwell model and a viscous damper [35].

For this system, the following equations hold:

$$\begin{aligned} \tau &= \tau_0 + \tau_1 \\ \tau_0 &= \eta_0 \dot{\gamma} \\ \tau_1 + \lambda \dot{\tau}_1 &= \eta_1 \dot{\gamma} \end{aligned} \tag{2.12}$$

where τ_0 and τ_1 are shear stresses developed by upper viscous damper and the bottom Maxwell element, respectively. The relaxation time here is $\lambda = \frac{\eta_1}{G_1}$.

2.3.4 Stress and strain decomposition

To model the material behavior of elastoplastic, viscoplastic, or viscoelastic materials, the stress and strain decomposition is typically adopted since materials typically exhibit differing behavior in the volumetric and deviatoric components of the stress. Simply speaking, the volumetric response is characterized by the pressure-volume relation, or response in hydrostatic pressure, while the deviatoric response is characterized by the shear stress and shear strain relationship, or in other words the response under material distortion.

The stress and strain tensors (of various measure to be discussed in detail later) can be expressed as:

$$\boldsymbol{\sigma} = \begin{bmatrix} \sigma_{11} & \sigma_{12} & \sigma_{13} \\ \sigma_{21} & \sigma_{22} & \sigma_{23} \\ \sigma_{31} & \sigma_{32} & \sigma_{33} \end{bmatrix} \tag{2.13}$$

$$\boldsymbol{\varepsilon} = \begin{bmatrix} \varepsilon_{11} & \varepsilon_{12} & \varepsilon_{13} \\ \varepsilon_{21} & \varepsilon_{22} & \varepsilon_{23} \\ \varepsilon_{31} & \varepsilon_{32} & \varepsilon_{33} \end{bmatrix} \tag{2.14}$$

The decomposition into spherical (volumetric) and deviatoric part of stress can be performed as:

$$\mathrm{sph}(\boldsymbol{\sigma}) = \begin{bmatrix} \frac{1}{3}\sigma_{ii} & 0 & 0 \\ 0 & \frac{1}{3}\sigma_{ii} & 0 \\ 0 & 0 & \frac{1}{3}\sigma_{ii} \end{bmatrix} \tag{2.15}$$

$$\mathrm{dev}(\boldsymbol{\sigma}) = \begin{bmatrix} \sigma_{11} - \frac{1}{3}\sigma_{ii} & \sigma_{12} & \sigma_{13} \\ \sigma_{21} & \sigma_{22} - \frac{1}{3}\sigma_{ii} & \sigma_{23} \\ \sigma_{31} & \sigma_{32} & \sigma_{33} - \frac{1}{3}\sigma_{ii} \end{bmatrix} \tag{2.16}$$

where $\sigma_{ii} = \sigma_{11} + \sigma_{22} + \sigma_{33}$.

And for strain:

$$\text{sph}(\boldsymbol{\varepsilon}) = \begin{bmatrix} \frac{1}{3}\varepsilon_{ii} & 0 & 0 \\ 0 & \frac{1}{3}\varepsilon_{ii} & 0 \\ 0 & 0 & \frac{1}{3}\varepsilon_{ii} \end{bmatrix} \tag{2.17}$$

$$\text{dev}(\boldsymbol{\varepsilon}) = \begin{bmatrix} \varepsilon_{11} - \frac{1}{3}\varepsilon_{ii} & \varepsilon_{12} & \varepsilon_{13} \\ \varepsilon_{21} & \varepsilon_{22} - \frac{1}{3}\varepsilon_{ii} & \varepsilon_{23} \\ \varepsilon_{31} & \varepsilon_{32} & \varepsilon_{33} - \frac{1}{3}\varepsilon_{ii} \end{bmatrix} \tag{2.18}$$

where $\varepsilon_{ii} = \varepsilon_{11} + \varepsilon_{22} + \varepsilon_{33}$.

The decomposition in plane strain problems is trivial as 3D cases, but for plane stress (2D) problems, care must be taken for the out-of-plane component [36]. For example, in plane stress linear elastic problems, the component ε_{33} can be solved for by applying the constraint $\sigma_{33} = 0$, which is obtained as:

$$\varepsilon_{33} = -\frac{\nu}{1-\nu}(\varepsilon_{11} + \varepsilon_{22}) \tag{2.19}$$

where ν is the Poisson's ratio of the material.

2.4 Conclusions

A general overview of concrete materials, 3D printing and its special application on concrete materials is introduced in this chapter, including the chemical properties, deposition techniques, and challenges involved. A general overview of rheology of non-Newtonian fluids, and viscoelastic and viscoplastic solids is given, where the various material laws can represent the response of different materials. Some commonly used models are reviewed. The stress and strain decomposition is then given for the application of the viscoplastic, viscoelastic laws, since materials often exhibit different behavior in volumetric and deviatoric response. This review serves as a basis for the choices in numerical simulation of printing concrete materials described in the following chapters.

Chapter 3
Numerical framework: the Reproducing Kernel Particle Method (RKPM)

3.1 Introduction

The Lagrangian finite element method (FEM) [37–39] has enjoyed great success in solving difficult engineering problems since its inception in the 1950s. However, this approach bears some disadvantages in particular classes of problems. For sufficiently large deformations, elements become distorted and the formulation loses accuracy, and stops in the case that the deformations become so large that the mesh becomes entangled [40]. On the other hand, a relatively new class of numerical methods call meshfree methods can circumvent these difficulties, by directly constructing the approximation in the Cartesian coordinates and avoiding the use of a mesh altogether. This section will introduce the meshfree approach with particular emphasis on the reproducing kernel particle method (RKPM), which is the basis for the present work. For a broader review, please refer to refs [40, 41].

In 1977, Gingold and Monaghan [42] and Lucy [43] proposed the first meshfree method called smoothed particle hydrodynamics (SPH). Over time, this method attracted researchers from many different areas, and in particular, in solid mechanics starting in the 1990s. To improve the accuracy of the kernel function in kernel estimate of SPH method, Liu et. al. [16] introduced a correction function to satisfy the reproducing condition for monomials and they called it the reproducing kernel

(RK) approximation.

The construction of the shape function of the RK approximation is done globally on a set of nodes, compared to locally based on a mesh as in FEM. It does not require any mesh connectivity but rather connectivity is defined naturally through distance functions, thus allowing deassociation, and reassociation of nodal connectivity in problems with extreme deformations. The RKPM consists of RK approximation equipped with a Galerkin formulation, which is the approximation of the solution of PDEs by approximation functions.

Though it has many advantages, some drawbacks exist at the same time. The shape function of the RK approximation does not have Kronecker Delta property, hence the essential boundary conditions cannot be directly enforced like FEM. There are, on the other hand, many methods which can resolve this issue, for example, the Lagrange multiplier method [44], the penalty method [45], the Nitsche's method [46–48], and the transformation method [49], to name a few.

Domain integration is another important issue in meshfree methods. In the origonal implementation, a background mesh was used to perform numerical integration, by Gauss quadrature. However, for a truly meshfree, this is not the most favorable approach. For example, direct nodal integration (DNI) is an alternative which avoids a mesh altogether, but it has a numerical instability [50]. To alleviate this drawback, Chen et. al. proposed the stabilized conforming nodal integration (SCNI) method [51] for problems with moderately large deformations, and the stabilized non-conforming nodal integration (SNNI) method [52] for problems with extreme deformations. More recently, Hillman and Chen [53] proposed the naturally stabilized nodal integration (NSNI) method to deal with the instability in direct nodal integration. In this approach, they also introduced an implicit gradient scheme to reduce the computation time significantly.

Convergence is another important issue in numerical methods. For mesfree methods, domain integration has a significant effect on convergence, which is in contrast to FEM. The variationally consistent integration (VCI) method has been introduced by Chen et.al. which can provide arbitrary order exactness [54], and yields associated convergence rates using low order quadrature, such as in direct nodal integration, or stabilized methods such as NSNI [53].

3.2 Methodology of RKPM

The reproducing kernel particle method employs the Galerkin formulation of boundary value problems, and the reproducing kernel approximation. In this section, each of them are discussed.

3.2.1 Reproducing kernel approximation

The RK approximation discretizes a domain into a set of Np nodes. Consider a set of nodes $\mathbf{S} = \{\boldsymbol{x}_1, \boldsymbol{x}_2, ..., \boldsymbol{x}_{Np} | \boldsymbol{x}_I \in \bar{\Omega}\}$, where $\boldsymbol{x}_I$ is the position vector of node I. The RK approximation is then constructed as:

$$u^h(\boldsymbol{x}) = \sum_{I=1}^{Np} \Psi_I(\boldsymbol{x}) d_I \tag{3.1}$$

where $\Psi_I(\boldsymbol{x})$ is the shape function associated with node I, and d_I is the nodal coefficient. The shape function is constructed by the product of a correction function and a kernel function:

$$\Psi_I(\boldsymbol{x}) = C(\boldsymbol{x}; \boldsymbol{x} - \boldsymbol{x}_I)\Phi_a(\boldsymbol{x} - \boldsymbol{x}_I) \tag{3.2}$$

where $\Phi_a(\boldsymbol{x} - \boldsymbol{x}_I)$ is the kernel function with compact support size a, and $C(\boldsymbol{x}; \boldsymbol{x} - \boldsymbol{x}_I)$ is the correction function which is composed of monomial bases to allow the exact reproduction of monomials:

$$C(\boldsymbol{x}; \boldsymbol{x} - \boldsymbol{x}_I) = \boldsymbol{H}^T(\boldsymbol{x} - \boldsymbol{x}_I)\boldsymbol{b}(\boldsymbol{x}) \tag{3.3}$$

where $\boldsymbol{H}(\boldsymbol{x} - \boldsymbol{x}_I)$ is a column vector of complete n^{th} order monomials and $\boldsymbol{b}(\boldsymbol{x})$ is a column vector coefficients. The kernel function provides smoothness (or roughness) of the approximation. The coefficients are obtained by enforcing the following reproducing condition:

$$\sum_{I=1}^{Np} \Psi_I(\boldsymbol{x})\boldsymbol{H}(\boldsymbol{x} - \boldsymbol{x}_I) = \boldsymbol{H}(\boldsymbol{0}) \tag{3.4}$$

Solving equations 3.2, 3.3 and 3.4 yields the shape function construction as:

$$\Psi_I(\boldsymbol{x}) = \boldsymbol{H}(\boldsymbol{0})\boldsymbol{M}^{-1}(\boldsymbol{x})\boldsymbol{H}(\boldsymbol{x}-\boldsymbol{x}_I)\Phi_a(\boldsymbol{x}-\boldsymbol{x}_I) \tag{3.5}$$

where the moment matrix $\boldsymbol{M}(\boldsymbol{x})$ is defined as:

$$\boldsymbol{M}(\boldsymbol{x}) = \sum_{I=1}^{Np} \boldsymbol{H}(\boldsymbol{x}-\boldsymbol{x}_I)\boldsymbol{H}^T(\boldsymbol{x}-\boldsymbol{x}_I)\Phi_a(\boldsymbol{x}-\boldsymbol{x}_I) \tag{3.6}$$

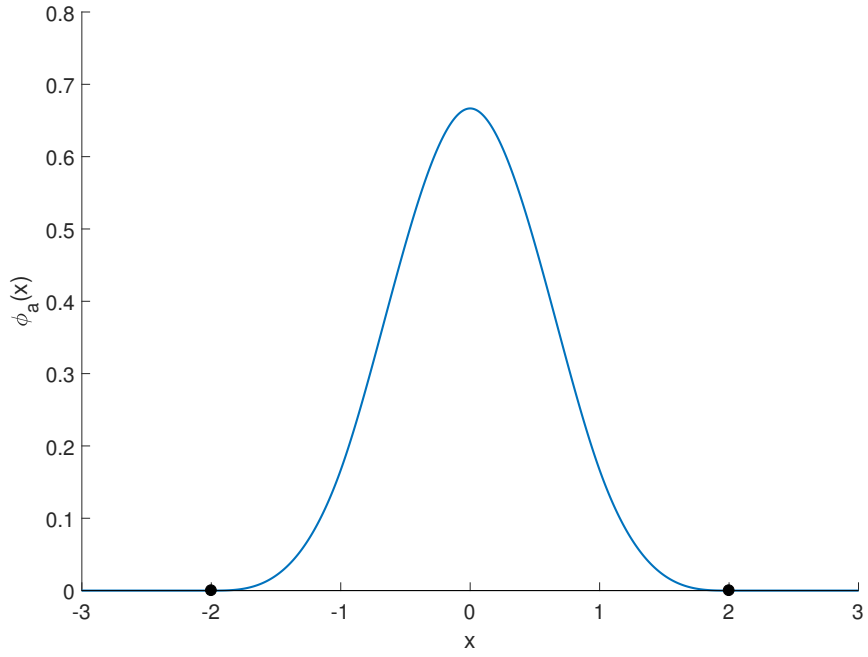

Figure 3.1: Cubic B-spline kernel function with a support size $a = 2$.

3.2.1.1 Kernel functions

From Equation 3.2, one can see that the kernel is an important composition of RK approximation. It decides the smoothness of the RK approximation and the influence domain locally by a support size. The choice of the support size is essential in meshfree methods. If it is very big, then the computational cost is high and it is less approximated to the delta function which induces with bigger errors; if it is very small, then the number of neighbors is not enough to construct

the shape function. One typical kernel function is the cubic B-spline which in one-dimensional space (1-D) is:

$$\phi_a(x-s) = \phi_a(z) = \begin{cases} \frac{2}{3} - 4z^2 + 4z^3 & \text{for } 0 \le z \le \frac{1}{2} \\ \frac{4}{3} - 4z + 4z^2 - \frac{4}{3}z^3 & \text{for } \frac{1}{2} \le z \le 1 \\ 0 & \text{for } z > 0 \end{cases} \tag{3.7}$$

$$z = \frac{|x-s|}{a}$$

Figure 3.1 shows a plot of the kernel function for support size $a = 2$ and $s = 0$.

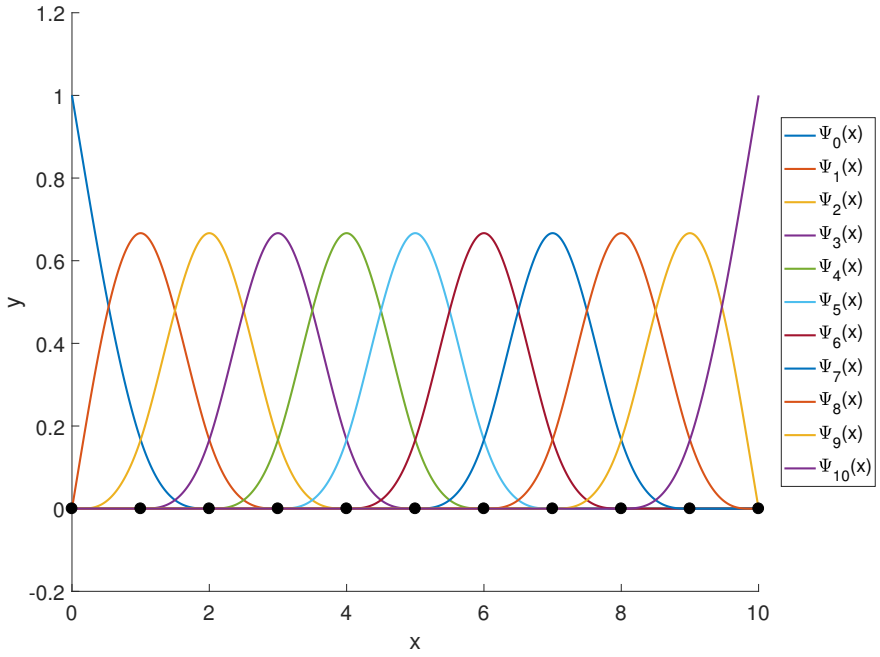

Figure 3.2: RK shape functions with 11 nodes and with linear basis.

3.2.1.2 RK shape functions

As an example of the RK shape function construction, a series of 11 nodes in the range of $[0, 10]$ with nodal spacing $h = 1.0$ is chosen. Linear basis ($n = 1$) and quadratic basis ($n = 2$) and a normalized support size of $a = 2$ are employed. The shape functions $\Psi_I(x)$ at each node for these two cases are shown in Figure 3.2 and Figure 3.3, respectively.

One can see that in general the shape functions of the RK approximation do not have the Kronecker Delta property. Thus when using RK approximation, the boundary conditions should be taken care of by special techniques which will be discussed later in the text.

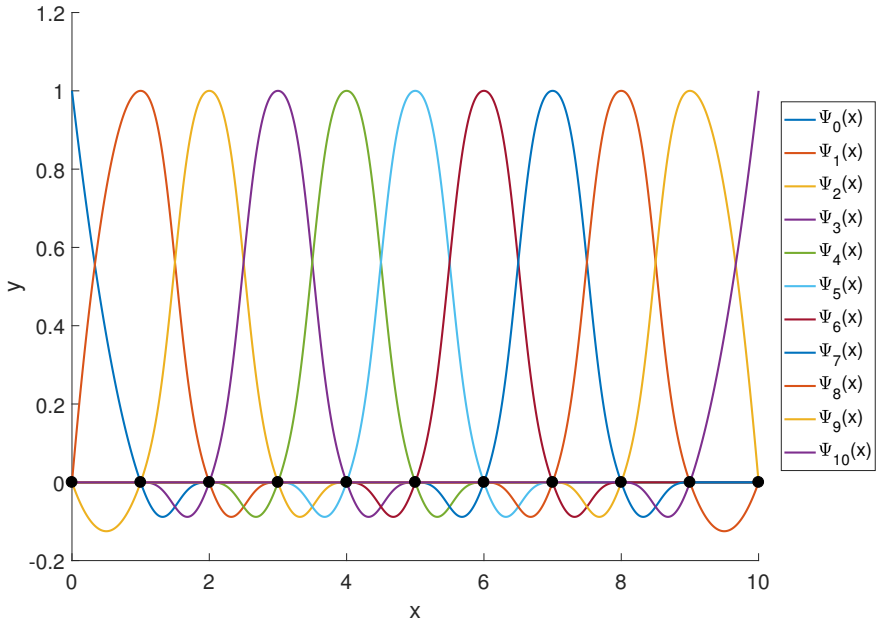

Figure 3.3: RK shape functions with 11 nodes and with quadratic basis.

3.2.1.3 Consistency condition check

In order to check the consistency of the RK approximation, the following reproducing condition should be verified:

$$\sum_{I}^{Np} \Psi_I(x) P^T(x - x_I) = P^T(0) \tag{3.8}$$

The results for linear basis and quadratic basis approximation are plotted in Figure 3.4a and Figure 3.4b, respectively. It is shown that the results are in good agreement with the consistency (reproducing) condition.

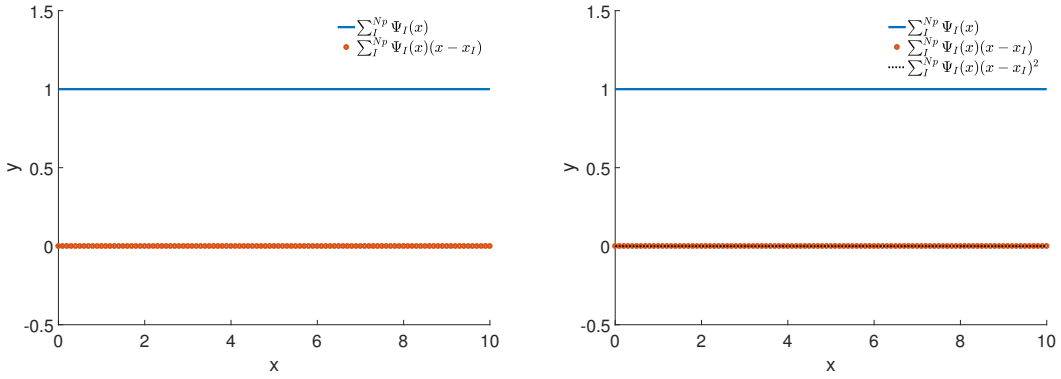

(a) Consistency check with linear basis (b) Consistency check with quadratic basis

Figure 3.4: Consistency check with 11 nodes, with two different basis vectors.

3.2.1.4 Error estimate

In order to evaluate the accuracy and convergence rate of the RK approximation, the L2-norm and H1-norms are typical error measures, which in 1-D are defined as follows:

$$\begin{aligned} \| u - u^h \|_{L2} &= [\int_\Omega (u - u^h)^2 \mathrm{d}\Omega]^{1/2} \\ &= \{\sum_{x_g} [u(x_g) - u^h(x_g)]^2 \omega(x_g)\}^{1/2} \end{aligned} \tag{3.9}$$

and

$$\begin{aligned} \| u - u^h \|_{H1} &= (\int_\Omega (u - u^h)^2 \mathrm{d}\Omega + \int_\Omega (u_{,x} - u^h_{,x})^2 \mathrm{d}\Omega)^{1/2} \\ &= \{\sum_{x_g} [(u(x_g) - u^h(x_g))^2 + (u_{,x}(x_g) - u^h_{,x}(x_g))^2] \omega(x_g)\}^{1/2} \end{aligned} \tag{3.10}$$

where x_g and $\omega(x_g)$ denote the location and weight of a Gauss (numerical integration) point.

For an approximation of a function with $n - th$ order basis, the convergence rate should be $n + 1$ for L2 norm and n for H1 norm. In the solution of boundary value problems the same rates are also expected, under the assumption that the exact solution is sufficiently smooth.

3.2.2 Strong form and weak form of the governing equation

The general governing equations in the context of continuum mechanics can be formulated as the classical initial boundary value problem:

$$\nabla \cdot \boldsymbol{\sigma} + \boldsymbol{f} = \rho \ddot{\boldsymbol{u}} \quad \text{in } \Omega \tag{3.11a}$$

$$\boldsymbol{\sigma} \cdot \boldsymbol{n} = \boldsymbol{h} \quad \text{on } \partial\Omega_h \tag{3.11b}$$

$$\boldsymbol{u} = \boldsymbol{g} \quad \text{on } \partial\Omega_g \tag{3.11c}$$

$$\boldsymbol{u}(0) = \boldsymbol{u}_0 \quad \text{in } \Omega \tag{3.11d}$$

$$\dot{\boldsymbol{u}}(0) = \dot{\boldsymbol{u}}_0 \quad \text{in } \Omega \tag{3.11e}$$

where $\boldsymbol{f}$ is the body force per unit volume in the domain $\bar{\Omega}$ which is bounded by boundary $\partial\Omega$, $\boldsymbol{h}$ is the surface traction on the natural boundary $\partial\Omega_h$, $\boldsymbol{g}$ is the displacement prescribed on the essential boundary $\partial\Omega_g$, and $\boldsymbol{n}$ is the unit outer normal to the boundary. The stress σ is obtained through the constitutive law, which is further related to strain ε obtained by the classical strain-displacement relation $\varepsilon = \nabla^s \boldsymbol{u}$, where ε is the strain and ∇^s denotes the symmetric part of a gradient. The decomposition of the boundary satisfies $\partial\Omega = \partial\Omega_g \cup \partial\Omega_h$ and $\partial\Omega_g \cap \partial\Omega_h = \varnothing$. The initial condition for displacement and velocity is given by $\boldsymbol{u}_0$ and $\dot{\boldsymbol{u}}_0$.

Note that for static or quasi-static problems, the inertia term and thus the initial condition are not present. The corresponding weak form of the governing equation can be obtained by the variational or virtual work principle. For simplicity and without loss of generality, the inertia term is ignored here.

First, the trail solution space for the weak formulation is defined as:

$$\mathbb{S} = \{\boldsymbol{u} : \bar{\Omega} \to \mathbb{R}^{n_{sd}} | \boldsymbol{u} \in [H^1]^{n_{sd}}, \boldsymbol{u}|_{\partial\Omega_g} = \boldsymbol{g}\} \tag{3.12}$$

where n_{sd} is the dimension of the problem.

The corresponding test function space is:

$$\mathbb{V} = \{\boldsymbol{w} : \bar{\Omega} \to \mathbb{R}^{n_{sd}} | \boldsymbol{w} \in [H^1]^{n_{sd}}, \boldsymbol{w}|_{\partial\Omega_g} = \boldsymbol{0}\} \tag{3.13}$$

With these in hand, the weak form asks:

Given $\boldsymbol{f}$, find $\boldsymbol{u} \in \mathbb{S}$, such that for all $\boldsymbol{w} \in \mathbb{V}$ the following holds:

$$a(\boldsymbol{u}, \boldsymbol{w}) = (\boldsymbol{f}, \boldsymbol{w}) + (\boldsymbol{h}, \boldsymbol{w})_{\partial\Omega_h} \tag{3.14}$$

where the compact notation has been introduced in the above:

$$\begin{aligned} a(\boldsymbol{u}, \boldsymbol{w}) &= \int_\Omega w_{i,j}\sigma_{ij} d\Omega \\ (\boldsymbol{f}, \boldsymbol{w}) &= \int_\Omega w_i f_i d\Omega \\ (\boldsymbol{h}, \boldsymbol{w})_{\partial\Omega_h} &= \int_{\partial\Omega_h} w_i h_i dS \end{aligned} \tag{3.15}$$

3.3 Numerical examples by RKPM

Several numerical examples are given to verify the properties of RKPM, which include the approximation of functions in 1-D and 2-D, and solving ordinary and partial differential equations in 1-D and 2-D, and elasticity in 2-D. The accuracy and the convergence of the results will be analyzed.

3.3.1 1-D approximation

In this example, the function $y = \sin(x)$ with the domain $x \in [-\pi, \pi]$ is the function to be approximated. The domain is discretized by evenly distributed 11, 21, 41 and 81 nodes which are given the exact value of the function as nodal coefficients. These nodal coefficients are then used to obtain the approximate value at a series of points.

To evaluate the approximation error, 2-point Gauss quadrature is used. A comparison of the approximated result with the exact value in a case of 21 nodes is shown in Figure 3.5. In this study, the support size $a = 1.5, 2.0, 2.5, 3.0$ and linear basis are used in the convergence analysis to test the influence of the support size on the computation error.

The L2-error of the approximation is plotted in Figure 3.6. One can observe that the convergence rate of the result is nearly $n + 1 = 2$ with linear basis, and agrees well with the theory presented in the previous text. One can also see that increasing the support size tends to increase the level of error in the L2 norm. As

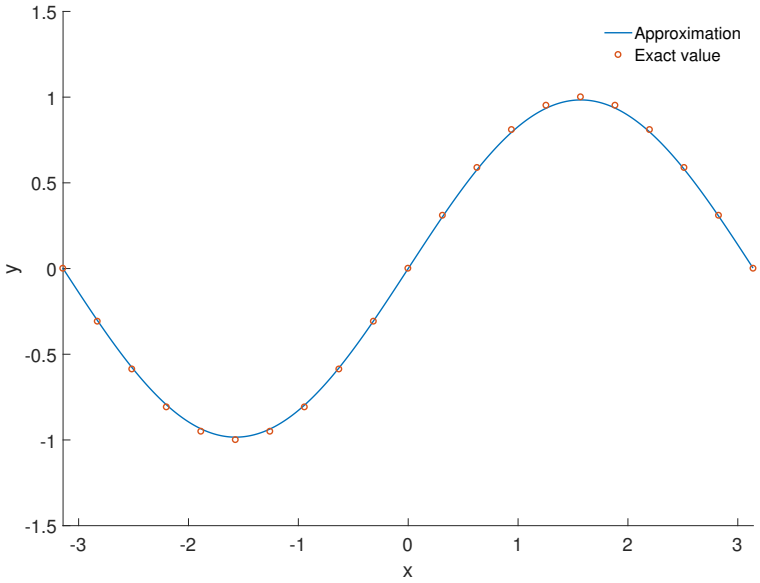

Figure 3.5: Approximated result for $\sin(x)$ with 21 nodes.

mentioned earlier, this is because with a smaller support size, the kernel function is more approximated to the delta function.

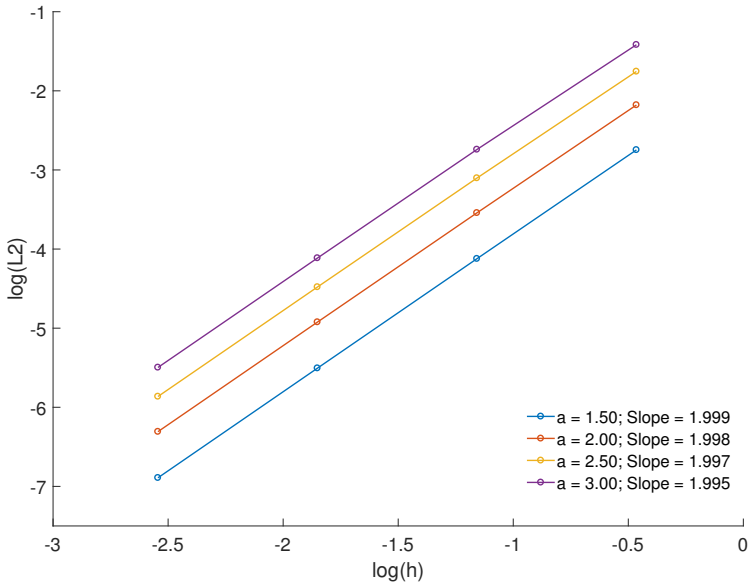

Figure 3.6: L2-norm of the approximation of $\sin(x)$.

3.3.2 1-D two-point boundary value problem

3.3.2.1 Strong form

Next, the 1-D Helmholtz equation is solved by RKPM. The strong form of the second order ordinary differential equation is:

$$\frac{\partial^2 u}{\partial x^2} + k^2 u = 0 \tag{3.16}$$

where k is the wave number. The domain is $x \in [0, L]$ with the essential boundary condition $u(0) = u_0 = 1.0$ and $u(L) = u_L = 0.0$.

The exact solution for these conditions are:

$$u(x) = \frac{\sin(k(L-x))}{\sin(kL)} \tag{3.17}$$

which will provide reference values for assesing the numerical results.

3.3.2.2 Weak form

The weak form of the Helmholtz equation can be obtained by weighted residual formulation as follows:

$$\int_\Omega w(\frac{\partial^2 u}{\partial x^2} + k^2 u) d\Omega = \int_\Omega w \frac{\partial^2 u}{\partial x^2} d\Omega + \int_\Omega w k^2 u d\Omega = 0 \tag{3.18}$$

where w is the test function, or weight function. Let the set of the test functions, or test function space, be denoted as:

$$\mathbb{V} = \{w | w \in H^1, w(0) = w(L) = 0\} \tag{3.19}$$

Similarly, the space of trail solutions, expressed as $\mathbb{S}$ is:

$$\mathbb{S} = \{u | u \in H^1, u(0) = 1, u(L) = 0\} \tag{3.20}$$

Introducing integration by parts and the essential boundary conditions yields:

$$\frac{\partial u}{\partial x} \cancel{w} 0 |_0^L - \int_\Omega \frac{\partial w}{\partial x} \frac{\partial u}{\partial x} d\Omega + \int_\Omega w k^2 u d\Omega = 0 \tag{3.21}$$

Written in a more compact form using the notation introduced earlier, the weak form is expressed: find $u \in \mathbb{S}$ such that for all $w \in \mathbb{V}$, the following equation holds

$$a(u, w) - (k^2 u, w) = 0 \tag{3.22}$$

where

$$a(u, w) = \int_\Omega \frac{\partial w}{\partial x} \frac{\partial u}{\partial x} d\Omega \tag{3.23}$$

and

$$(k^2 u, w) = \int_\Omega w k^2 u d\Omega \tag{3.24}$$

3.3.2.3 Galerkin form and matrix form

The Galerkin form is obtained by applying the RK approximation to both the trial function and test function, namely:

$$\begin{aligned} u^h &= \sum_I^{Np} \Psi_I d_I = \boldsymbol{N}^T \boldsymbol{D} \\ w^h &= \sum_I^{Np} \Psi_I w_I = \boldsymbol{N}^T \boldsymbol{W} \end{aligned} \tag{3.25}$$

where Ψ_I is the shape function at node I and d_I is nodal coefficient. $\boldsymbol{N}^T = [\Psi_1, \Psi_2, ..., \Psi_{Np}]$ is the matrix for RK shape functions for all nodes. $\boldsymbol{D}^T = [d_1, d_2, .., d_{Np}]$ and $\boldsymbol{W}^T = [w_1, w_2, .., w_{Np}]$ are vectored nodal coefficients and weights.

The weak form in Equation 3.22 is then approximated by the Galerkin form:

$$a(u^h, w^h) - (k^2 u^h, w^h) = 0 \tag{3.26}$$

Substituting the approximation for trial and test functions into Equation 3.26 gives:

$$\boldsymbol{W}^T \left(\int_\Omega \boldsymbol{N}_{,x} \boldsymbol{N}_{,x}^T \boldsymbol{D} d\Omega - k^2 \int_\Omega \boldsymbol{N} \boldsymbol{N}^T \boldsymbol{D} d\Omega \right) = 0 \tag{3.27}$$

where $\boldsymbol{N}_{,x} = \frac{\partial \boldsymbol{N}}{\partial x}$ stands for the derivatives of $\boldsymbol{N}$ with respect to x.

Since $\boldsymbol{W}$ is arbitrary, Equation 3.27 can be cast in a matrix system of equations:

$$\boldsymbol{K} \boldsymbol{D} = \boldsymbol{0} \tag{3.28}$$

where the stiffness matrix $\boldsymbol{K}$ is:

$$\boldsymbol{K} = \int_{\Omega} \boldsymbol{N}_{,x} \boldsymbol{N}_{,x}^{T} d\Omega - k^2 \int_{\Omega} \boldsymbol{N}\boldsymbol{N}^{T} d\Omega \tag{3.29}$$

3.3.2.4 Imposing boundary condition by transformation method

As discussed previously, the shape function of the RK approximation does not exhibit the Kronecker Delta property. The transformation method is used in this study to impose the boundary condition.

The transformation method can be derived as follows. By the approximation in Equation 3.25, one has:

$$\boldsymbol{U} = \begin{bmatrix} u_1 \\ u_2 \\ \vdots \\ u_{Np} \end{bmatrix} = \begin{bmatrix} \Psi_1(x_1) & \Psi_2(x_1) & \dots & \Psi_{Np}(x_1) \\ \Psi_1(x_2) & \Psi_2(x_2) & \dots & \Psi_{Np}(x_2) \\ \vdots & \vdots & \vdots & \vdots \\ \Psi_1(x_{Np}) & \Psi_2(x_{Np}) & \dots & \Psi_{Np}(x_{Np}) \end{bmatrix} \begin{bmatrix} d_1 \\ d_2 \\ \vdots \\ d_{Np} \end{bmatrix} = \boldsymbol{\Lambda}\boldsymbol{D} \tag{3.30}$$

where $u_I \equiv u^h(x_I)$ and $\boldsymbol{\Lambda}$ is the so-called transformation matrix.

The nodal coefficient vector can thus be expressed as:

$$\boldsymbol{D} = \boldsymbol{\Lambda}^{-1}\boldsymbol{U} \tag{3.31}$$

The matrix form in Equation 3.28 is then rewritten as:

$$(\boldsymbol{K}\boldsymbol{\Lambda}^{-1})\boldsymbol{U} = \boldsymbol{0} \tag{3.32}$$

The boundary condition can then be imposed directly by plugging $u_1 = 1$ and $u_{Np} = 0$. After the nodal values are solved, one can recover the numerical approximation at arbitrary point x by reconstructing the coefficient vector, or solving for the solution directly reconstructed as:

$$u^h(x) = \boldsymbol{N}^{T}\boldsymbol{D} = \boldsymbol{N}^{T}\boldsymbol{\Lambda}^{-1}\boldsymbol{U} \tag{3.33}$$

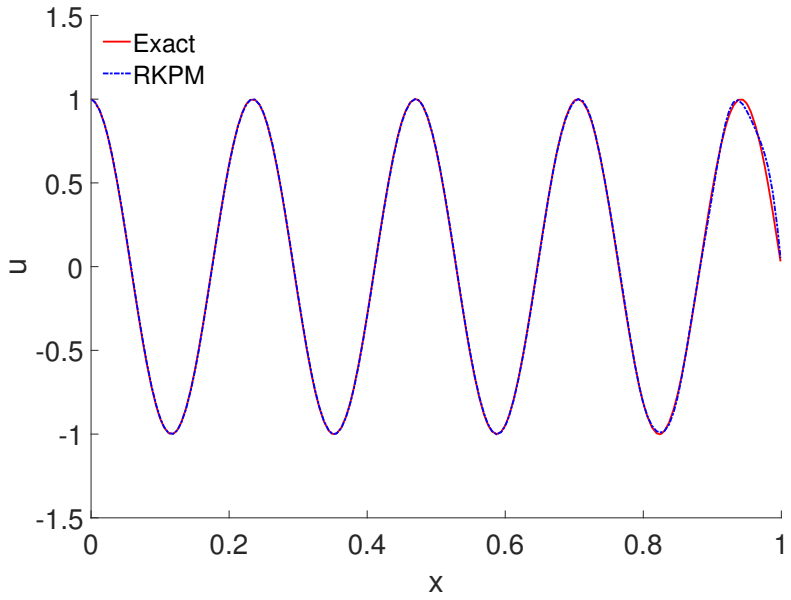

Figure 3.7: Comparison of the numerical result and the exact result for the wave bar problem.

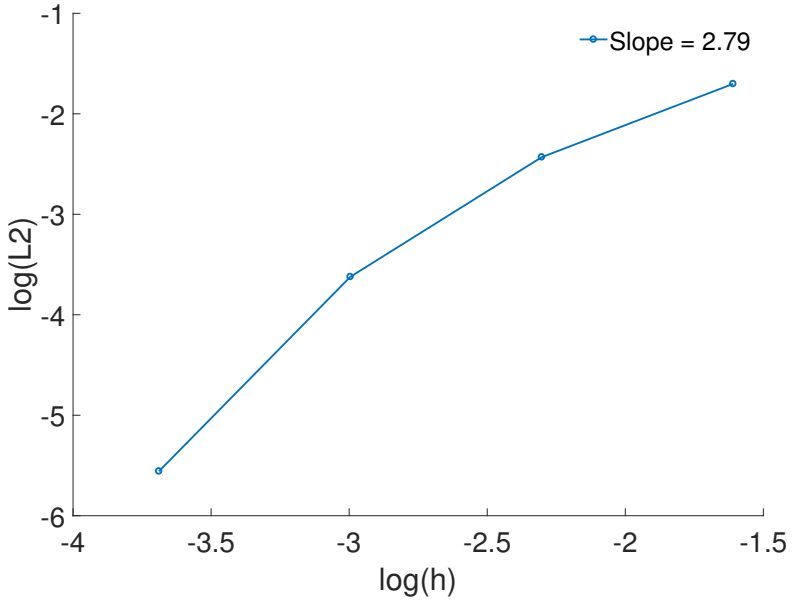

Figure 3.8: L2 norm of the numerical result by RKPM for 1D wave bar problem.

3.3.2.5 Numerical results

The length of the problem domain is chosen as $L = 1.0$. A discretization of the domain by 6, 11, 21, and 41 nodes is used for this example. A normalized

support size $a = 3.0$ and wave number $k = 2/h$ are chosen, where h is the uniform nodal spacing. The cubic spline kernel and linear basis are employed for the shape function. 5-point Gauss quadrature is used to evaluate the L2-norm error.

The numerical result by RKPM with 41 nodes, compared to the exact solution with is shown in Figure 3.7. It can be seen that good agreement between the RKPM and the exact solution is obtained. The L2-norm of the error for various nodal spacing is shown in Figure 3.8, where it can be seen that the optimal convergence rate of two is achieved by RKPM, and also that even superconvergence is observed.

3.3.3 2-D approximation

The function $z = \sin(x)\sin(y)$ with the domain $(x, y) \in [-\pi, \pi] \times [-\pi, \pi]$ is chosen as a function to be approximated. The domain is discretized by evenly distributed 11×11, 21×21, 41×41 and 81×81 nodes. A rectangular kernel $\phi_a(x, y) = \phi_a(x) \cdot \phi_a(y)$ with support size $a = 3$ is chosen, along with linear basis $P = [1, x, y]^T$.

2-point Gauss quadrature is used to evaluate the approximation error. The comparison of the approximated result to the exact value in 21×21 nodes case is shown in Figure 3.9, where good agreement is observed.

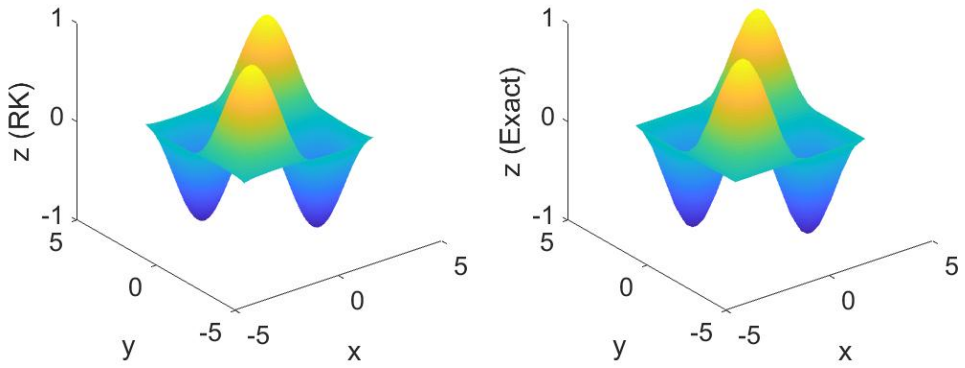

Figure 3.9: Comparison of approximated result (left) and exact plot (right) for $z = \sin(x)\sin(y)$ with 21×21 nodes.

The L2-error estimate of the approximation is plotted in Figure 3.10. It is easy to see that the convergence rate of the result is nearly $n + 1 = 2$ with linear basis, again in good agreement with the expected rate.

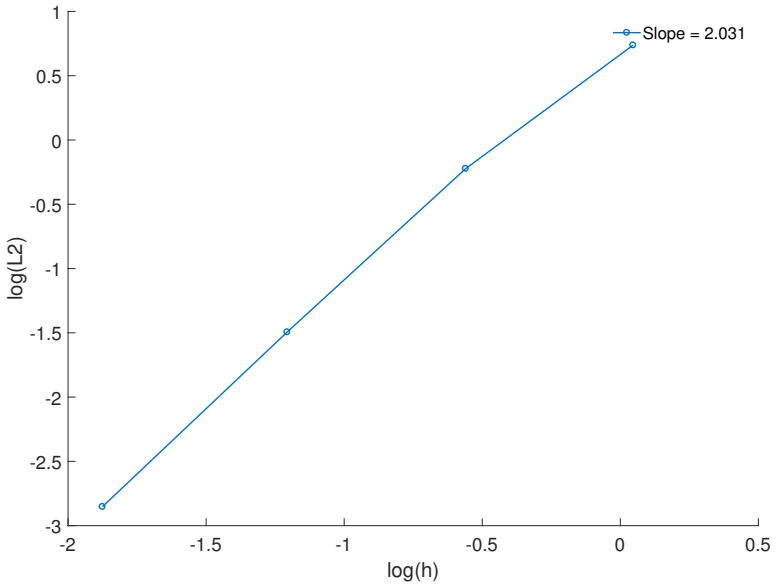

Figure 3.10: L2-norm of the 2-D approximation of $\sin(x)\sin(y)$.

3.3.4 2-D second order PDE

3.3.4.1 Strong form

Next, the Poisson equation is solved to examine the performance of RKPM in a second-order PDE in two-dimensions:

$$\Delta u + f = 0 \tag{3.34}$$

where Δ is the Laplacian operator and the source term f is chosen as:

$$f = -(x^2 + y^2)e^{xy} \tag{3.35}$$

A domain $(x, y) \in [0, 1] \times [0, 1]$ and boundary condition $u = g = e^{xy}$ on $\partial\Omega$.

The exact solution of this Poisson problem is:

$$u = e^{xy} \tag{3.36}$$

3.3.4.2 Weak form

The weak form of the Poisson equation can be derived similar to Section 3.3.2. Using the weighted residual formulation gives:

$$\int_\Omega w(\frac{\partial^2 u}{\partial x^2} + \frac{\partial^2 u}{\partial y^2})d\Omega + \int_\Omega w f d\Omega = 0 \tag{3.37}$$

where w is the test function or weighted function.

The trail solutions space is:

$$\mathbb{S} = \{u | u \in [H^1], u = g \text{ on } \partial\Omega_g\} \tag{3.38}$$

and the corresponding test function space is:

$$\mathbb{V} = \{w | w \in [H^1], w = 0 \text{ on } \partial\Omega_g\} \tag{3.39}$$

Introducing integration by parts and the essential boundary condition yields:

$$\int_{\partial\Omega} (\nabla u \cdot \boldsymbol{n}) \cancelto{0}{w} \mathrm{d}S - \int_\Omega \nabla u \cdot \nabla w d\Omega + \int_\Omega w f d\Omega = 0 \tag{3.40}$$

In compact form as before, the weak form is formulated as: find $u \in \mathbb{S}$ such that for all $w \in \mathbb{V}$, the following equation holds

$$a(u, w) - (f, w) = 0 \tag{3.41}$$

3.3.4.3 Galerkin form and matrix form

To obtain the Galerkin equation, the RK approximation is introduced for both the trial function and test function, as before:

$$\begin{aligned} u^h &= \sum_I^{Np} \Psi_I d_I = \boldsymbol{N}^T \boldsymbol{D} \\ w^h &= \sum_I^{Np} \Psi_I w_I = \boldsymbol{N}^T \boldsymbol{W} \end{aligned} \tag{3.42}$$

where Ψ_I, $\boldsymbol{N}^T$, $\boldsymbol{D}^T$ and $\boldsymbol{W}^T$ are the same as Section 3.3.2.

The weak form in Equation 3.41 can then be approximated as the Galerkin

form:

$$a(u^h, w^h) - (f, w^h) = 0 \tag{3.43}$$

Plugging the RK approximation for trial and test functions into Equation 3.43 yields:

$$\boldsymbol{W}^T\{\int_\Omega [\boldsymbol{N}_{,x}, \boldsymbol{N}_{,y}] \cdot [\boldsymbol{N}_{,x}^T, \boldsymbol{N}_{,y}^T]^T \boldsymbol{D} d\Omega + \int_\Omega \boldsymbol{N}^T \boldsymbol{f} d\Omega\} = 0 \tag{3.44}$$

Since $\boldsymbol{W}$ is arbitrary, then Equation 3.44 can be solved using the following matrix form:

$$\boldsymbol{K}\boldsymbol{D} = \boldsymbol{b} \tag{3.45}$$

where the stiffness matrix $\boldsymbol{K}$ and the force vector $\boldsymbol{b}$ are:

$$\begin{aligned} \boldsymbol{K} &= \int_\Omega (\boldsymbol{N}_{,x}\boldsymbol{N}_{,x}^T + \boldsymbol{N}_{,y}\boldsymbol{N}_{,y}^T) d\Omega \\ \boldsymbol{b} &= \int_\Omega \boldsymbol{N} f d\Omega \end{aligned} \tag{3.46}$$

Again, this system equation can be solved by using the transformation method. Instead, this study will study the other classical techniques as follows.

3.3.4.4 Imposing essential boundary conditions in meshfree methods

In order to impose the essential boundary conditions, the Lagrange multiplier method, the penalty method and Nitsche's method are used in this study.

1. Lagrange multiplier

The solution of a self-adjoint PDE can be obtained from a minimization problem, with constraints also introduced as needed, enforced using a Lagrange multiplier. Since the RK approximation lacks the Kronecker Delta property, the essential boundary condition (a constraint) can be imposed by the Lagrange multiplier method rather than the transformation method. In this case, the functional at hand is:

$$\Pi_P = \Pi + \int_{\partial\Omega_g} \lambda(u - g) \mathrm{d}S \tag{3.47}$$

where the conventional term Π is:

$$\Pi = \frac{1}{2}\int_\Omega \nabla u \cdot \nabla u \, \mathrm{d}\Omega - \int_\Omega uf \, \mathrm{d}\Omega - \int_{\partial\Omega_h} uh dS \tag{3.48}$$

The trail function space for u and λ are:

$$\begin{aligned}\mathbb{S}_u &= \{u|u \in [H^1], u = g \text{ on } \partial\Omega_g\} \\ \mathbb{S}_\lambda &= \{\lambda|\lambda \in [H^0]\}\end{aligned} \tag{3.49}$$

and their corresponding test function spaces are

$$\begin{aligned}\mathbb{V}_u &= \{w|w \in [H^1], w = 0\} \\ \mathbb{V}_\lambda &= \{v|v \in [H^0]\}\end{aligned} \tag{3.50}$$

The weak form of this method can then be obtained by taking variational derivative of the functional in Equation 3.47. Employing the notation w for δu and v for $\delta\lambda$ one obtains:

$$\int_\Omega \nabla u \cdot \nabla w \, \mathrm{d}\Omega - \int_\Omega wf \, \mathrm{d}\Omega - \int_{\partial\Omega_h} wh \mathrm{d}S + \int_{\partial\Omega_g} (u-g)v \mathrm{d}S + \int_{\partial\Omega_g} \lambda\delta u \mathrm{d}S = 0 \tag{3.51}$$

In compact notation, the weak form can then be obtained as:

$$a(u,w) - (f,w) - (h,w)_{\partial\Omega_h} + (\lambda,w)_{\partial\Omega_g} - (u-g,v) = 0 \tag{3.52}$$

The approximation for u, w, λ and v are then introduced to obtain the Galerkin formulation:

$$\begin{aligned}u^h &= \sum_I^{Np} \Psi_I u_I = \boldsymbol{N}^T \boldsymbol{U} \\ w^h &= \sum_I^{Np} \Psi_I w_I = \boldsymbol{N}^T \boldsymbol{W} \\ \lambda^h &= \sum_I^{Np} \tilde{N}_I \lambda_I = \tilde{\boldsymbol{N}}^T \boldsymbol{\lambda} \\ v^h &= \sum_I^{Np} \tilde{N}_I v_I = \tilde{\boldsymbol{N}}^T \boldsymbol{V}\end{aligned} \tag{3.53}$$

Note here, the shape function $\tilde{N}_I$ for approximation of λ can be chosen as a finite element approximation, which is the option chosen in this example.

Following similar procedures as before, one can obtain the Galerkin form and

matrix form. For simplicity, the final matrix form is cast as:

$$\begin{bmatrix} \boldsymbol{K} & \boldsymbol{A}^T \\ \boldsymbol{A} & 0 \end{bmatrix} \begin{bmatrix} \boldsymbol{U} \\ \boldsymbol{\lambda} \end{bmatrix} = \begin{bmatrix} \boldsymbol{b} \\ \boldsymbol{q} \end{bmatrix} \tag{3.54}$$

where $\boldsymbol{K}$ and $\boldsymbol{b}$ are the same as Equation 3.46. The newly introduced matrices and vectors are:

$$\begin{aligned} \boldsymbol{A} &= \int_{\partial\Omega_g} \tilde{\boldsymbol{N}} \boldsymbol{N}^T \mathrm{d}S \\ \boldsymbol{q} &= \int_{\partial\Omega_g} \tilde{\boldsymbol{N}} g \mathrm{d}S \end{aligned} \tag{3.55}$$

One can see that extra degree of freedoms are introduced by Lagrange multiplier method, which adds computational cost. However, it does not have any parameters to tune.

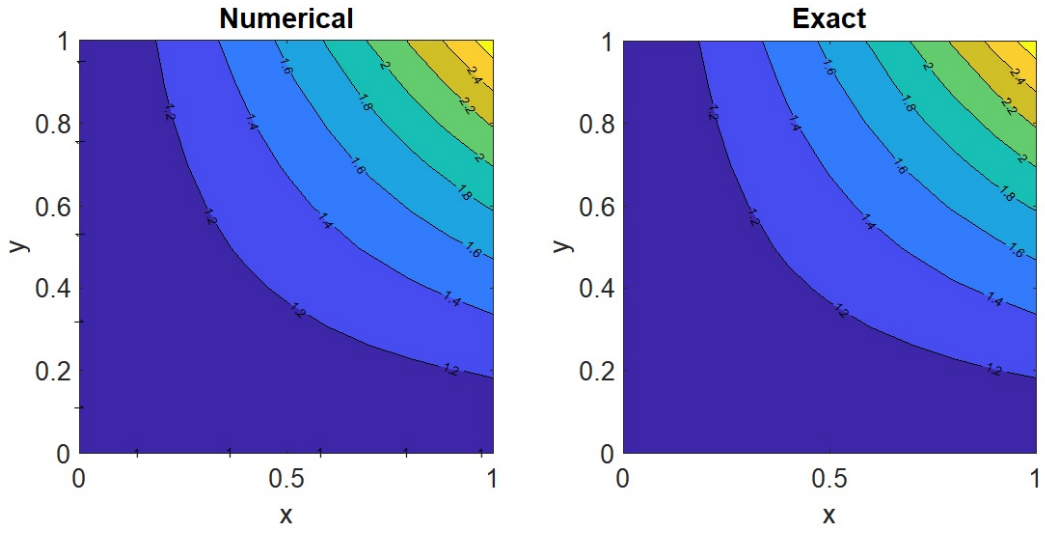

Figure 3.11: Comparison of the numerical solution and exact solution of Poisson equation by Lagrange multiplier.

2. Penalty method

The essence of penalty method is to use a large positive number to impose the essential boundary condition in a modified functional:

$$\Pi_L = \frac{1}{2}\int_\Omega \nabla u \cdot \nabla u \, \mathrm{d}\Omega - \int_\Omega uf \, \mathrm{d}\Omega - \int_{\partial\Omega_h} uh \mathrm{d}S + \frac{\beta}{2}\int_{\partial\Omega_g} (u-g)^2 \mathrm{d}S \tag{3.56}$$

Following similar proceedures as the Lagrange multiplier method, but without introducing new degrees of freedom, the matrix form of the system equation is written as:

$$(\boldsymbol{K} + \beta \boldsymbol{K}^{\beta})\boldsymbol{u} = (\boldsymbol{b} + \beta \boldsymbol{b}^{\beta}) \tag{3.57}$$

where the newly added matrices and vectors are:

$$\begin{aligned} \boldsymbol{K}^{\beta} &= \int_{\Omega} \boldsymbol{N}\boldsymbol{N}^{T} \, \mathrm{d}\Omega \\ \boldsymbol{b}^{\beta} &= \int_{\partial\Omega_g} \boldsymbol{N} g \mathrm{d}S \end{aligned} \tag{3.58}$$

Though no extra degree of freedom is introduced, the implementation of penalty method needs tuning of the penalty parameter β [55]. The advantage of this technique is the ease of implementation and keeps the symmetric property of the stiffness matrix. The drawback is that if the penalty parameter is too small, then the boundary condition is not imposed strictly; if it is too large, the stiffness matrix obtained is ill-conditioned and would result in inaccurate solutions.

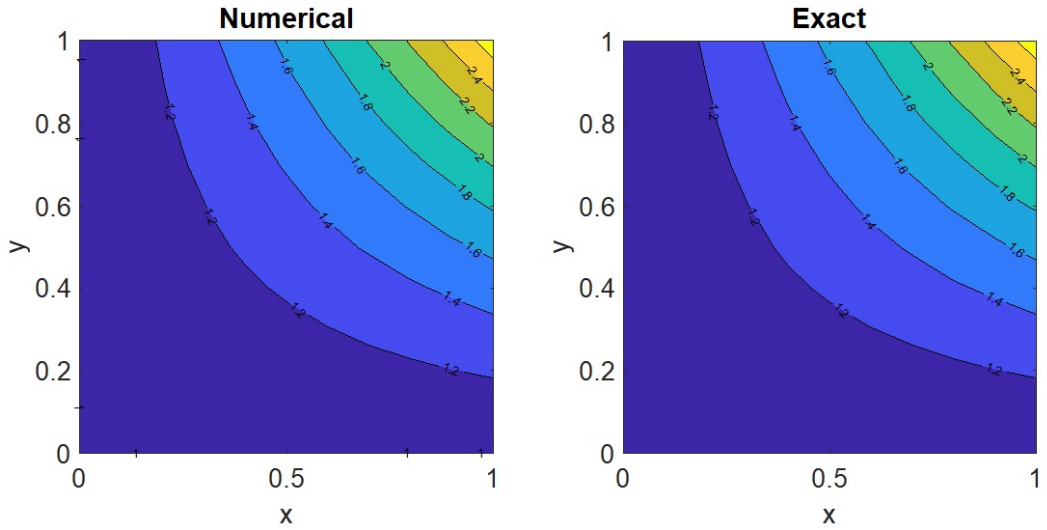

Figure 3.12: Comparison of the numerical solution and exact solution of Poisson equation by penalty method.

3. Nitsche's method

Nitsche's method is considered as a consistent improvement of penalty method

[55]. The weak form of Nitsche's method is:

$$\begin{aligned} a(u,w) - (\nabla u \cdot \boldsymbol{n}, w)_{\partial\Omega_g} - (u, \nabla w \cdot \boldsymbol{n})_{\partial\Omega_g} + \beta(u,w)_{\partial\Omega_g} \\ = (f,w) + (h,w)_{\partial\Omega_h} - (g, \nabla w \cdot \boldsymbol{n})_{\partial\Omega_g} + \beta(g,w)_{\partial\Omega_g} \end{aligned} \tag{3.59}$$

Introducing the approximation function by Galerkin approximation results in the final matrix form as:

$$(\boldsymbol{K} + \beta \boldsymbol{K}^{\beta} - \tilde{\boldsymbol{K}} - \tilde{\boldsymbol{K}}^T)\boldsymbol{u} = (\boldsymbol{b} + \beta \boldsymbol{b}^{\beta} - \tilde{\boldsymbol{b}}) \tag{3.60}$$

where the newly introduced matrices and vectors are:

$$\begin{aligned} \tilde{\boldsymbol{K}} &= \int_{\partial\Omega_g} \boldsymbol{N} \nabla \boldsymbol{N}^T \, \boldsymbol{n} \mathrm{d}S \\ \tilde{\boldsymbol{b}} &= \int_{\partial\Omega_g} g \nabla \boldsymbol{N} \boldsymbol{n} \mathrm{d}S \end{aligned} \tag{3.61}$$

Where $\boldsymbol{n}$ is the normal in vector form.

The advantages of Nitsche's method include that it produces symmetric stiffness matrix; it is less sensitive than the penalty method on the penalty parameter and it is moderately easy to implement; last but not least, it does not introduce additional degrees of freedom. However, it may not be easy to apply to nonlinear problems.

3.3.4.5 Numerical results

The domain is discretized by 3×3, 6×6, 11×11, and 21×21 nodes, respectively. A linear basis and a support size $a = 1.75$ are adopted for RK approximation. 2-point Gauss quadrature is employed to conduct the numerical integration. For penalty method and Nitsche's method, the penalty parameter used is $\beta = 1 \times 10^5$. The numerical results of the solution by Lagrange multiplier, penalty method and Nitsche's method are shown in Figure 3.11, Figure 3.12 and Figure 3.13, respectively. It is easy to see that very good agreement has been made with all three methods. The L2 norm error of these methods is shown in Figure 3.14, where similar error measure and convergence rate are observed, despite the penalty method being sensitive to the choice of parameter.

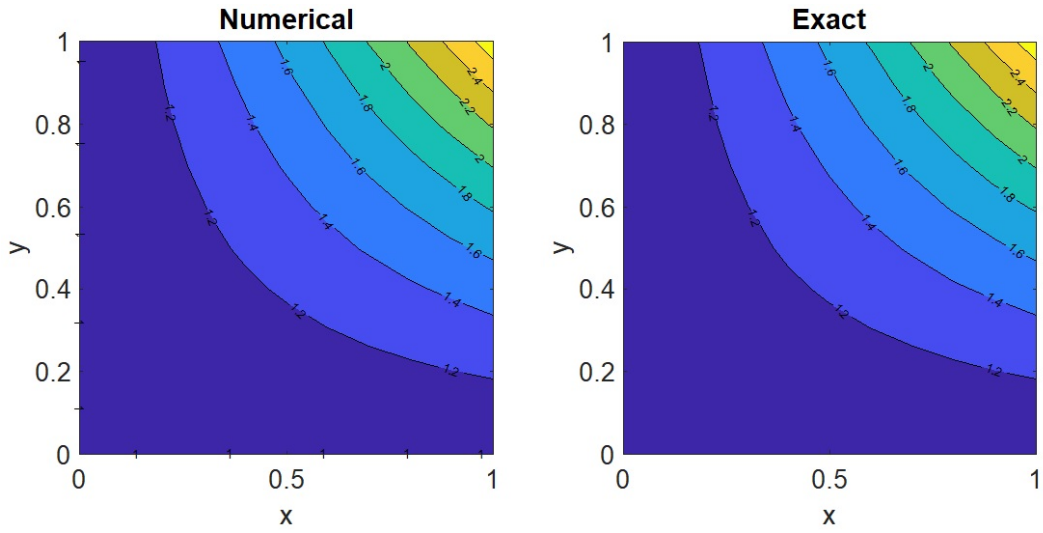

Figure 3.13: Comparison of the numerical solution and exact solution of Poisson equation by Nitsche's method.

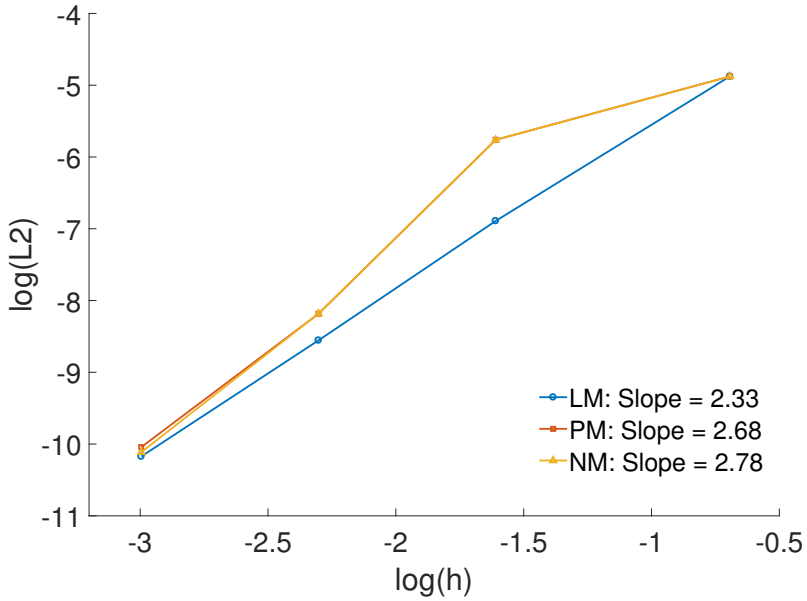

Figure 3.14: Comparison of the L2 norm by Lagrange multiplier (LM), penalty method (PM) and Nitsche's method (NM).

3.3.5 2-D elasticity problem

Next, two elastic problems with linear isotropic elasticity are solved by RKPM. The governing equation in the weak form is Equation 3.14. The Galerkin form

of the governing equation can be obtained by substituting the RK approximation functions into the weak form:

$$a(\boldsymbol{u}^h, \boldsymbol{w}^h) = (\boldsymbol{h}, \boldsymbol{w}^h)_{\partial\Omega_h} + (\boldsymbol{f}, \boldsymbol{w}^h) \tag{3.62}$$

where the compact notation the same as Equation 3.14 and the approximation functions are:

$$\boldsymbol{u}^h = \sum_{I}^{Np} \boldsymbol{\Psi_I u_I} = \boldsymbol{N}^T \boldsymbol{U} \tag{3.63}$$

It should be noted that different from the Poisson problem, elasticity is vector-valued problem. That is, the shape functions and the nodal coefficients are not the same as previous section. Namely,

$$\boldsymbol{\Psi_I u_I} = \begin{bmatrix} \Psi_I & 0 \\ 0 & \Psi_I \end{bmatrix} \begin{bmatrix} u_I \\ v_I \end{bmatrix} \tag{3.64}$$

where u_I and v_I are nodal coefficient of displacement in x- and y-direction for node I.

For an elastic isotropic material, the constitutive equation can be expressed as:

$$\boldsymbol{\sigma} = \mathbb{C} : \nabla^s \boldsymbol{u} \tag{3.65}$$

where $\mathbb{C}$ is the forth order elasticity tensor and $\nabla^s \boldsymbol{u} = \frac{1}{2}(\nabla \boldsymbol{u} + (\nabla \boldsymbol{u})^T)$ is the strain tensor. The corresponding matrix form of the elastic tensor under the plane stress assumption is denoted by $\boldsymbol{D}$, which is:

$$\boldsymbol{D} = \frac{E}{1-\nu^2} \begin{bmatrix} 1 & \nu & 0 \\ \nu & 1 & 0 \\ 0 & 0 & \frac{1-\nu}{2} \end{bmatrix} \tag{3.66}$$

where E and ν are elastic modulus and Poisson's ratio, respectively.

The matrix form is established as:

$$\boldsymbol{KU} = \boldsymbol{b} \tag{3.67}$$

where the stiffness matrix and vectors are:

$$\begin{aligned} \boldsymbol{K} &= \int_{\Omega} \boldsymbol{B}^T \boldsymbol{D} \boldsymbol{B} \, \mathrm{d}\Omega \\ \boldsymbol{b} &= \int_{\Omega} \boldsymbol{N} \boldsymbol{f} \, \mathrm{d}\Omega + \int_{\partial\Omega_h} \boldsymbol{N} \boldsymbol{h} \mathrm{d}S \end{aligned} \tag{3.68}$$

where the strain matrix $\boldsymbol{B} = [\boldsymbol{B}_1, \boldsymbol{B}_2, ..., \boldsymbol{B}_{Np}]$ and for $I-$th node, $\boldsymbol{B}_I$ is:

$$\boldsymbol{B}_I = \begin{bmatrix} \Psi_{I,x} & 0 \\ 0 & \Psi_{I,y} \\ \Psi_{I,y} & \Psi_{I,x} \end{bmatrix} \tag{3.69}$$

3.3.5.1 Plane stress linear patch test

Here a linear patch test is conducted. That is, a problem is designed such as it has a linear solution, and the resulting numerical solution is examined. The domain of the problem is chosen as $(x, y) \in [0, 1] \times [0, 1]$, and an essential boundary condition $\boldsymbol{u} = \boldsymbol{g} = [0.2x + 0.3y; 0.1x + 0.4y]$ on $\partial\Omega$ is prescribed. No body force is prescribed.

The exact solution of this problem is:

$$\boldsymbol{u} = \begin{bmatrix} 0.2x + 0.3y \\ 0.1x + 0.4y \end{bmatrix} \tag{3.70}$$

The domain is discretized by 4×4, 6×6, 11×11, and 21×21 nodes along with 2×2 Gauss quadrature applied. A rectangular kernel with support size $a = 1.75$ and linear basis are used for the RK approximation. The material parameters are $E = 0.3 \times 10^8$Pa and $\nu = 0.3$. The transformation method is adopted to impose the essential boundary condition.

The comparison of the numerical result and exact result for displacement in x- and y-direction in the case of 11×11 nodes discretization are shown in Figure 3.15 and Figure 3.16. One can see that the numerical solutions nearly reproduce the exact solutions.

The L2 norm error of this approximation is plotted in Figure 3.17 for the discretizations chosen. One can see that near machine-precision is achieved for all discretizations.

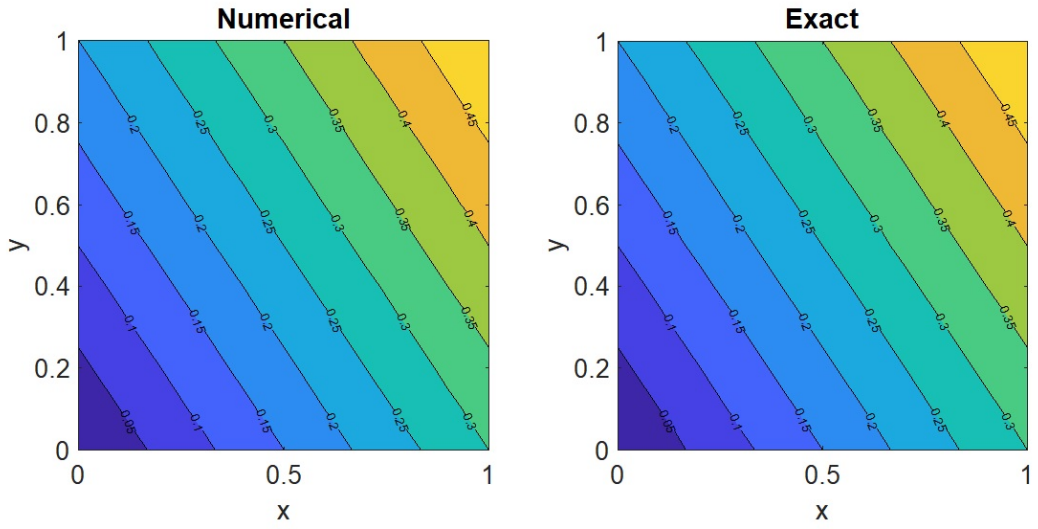

Figure 3.15: Results comparison of the numerical results and exact result of displacement in x-direction.

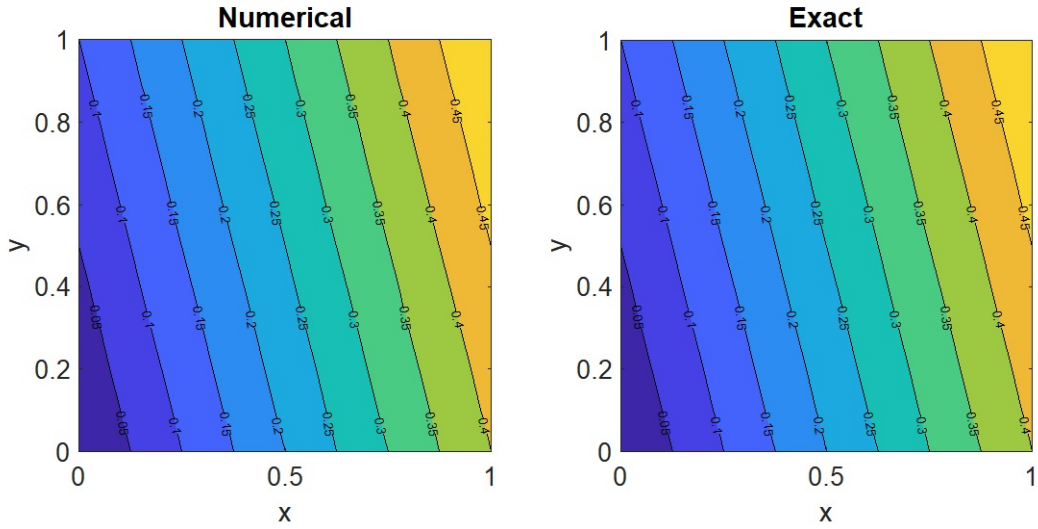

Figure 3.16: Results comparison of the numerical results and exact result of displacement in y-direction.

3.3.5.2 Timoshenko cantilever beam

The Timoshenko cantilever beam is chosen as the next problem. Figure 3.18 presents the geometry of the beam and the tip load applied. The essential bound-

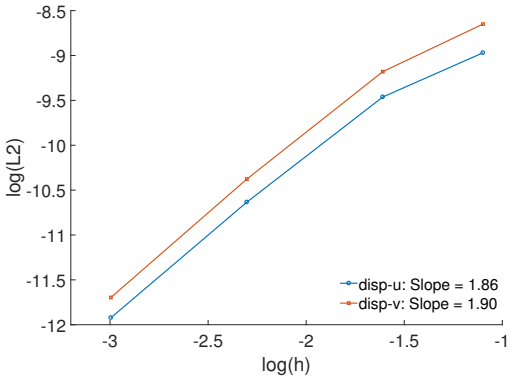

Figure 3.17: L2 norm for displacement.

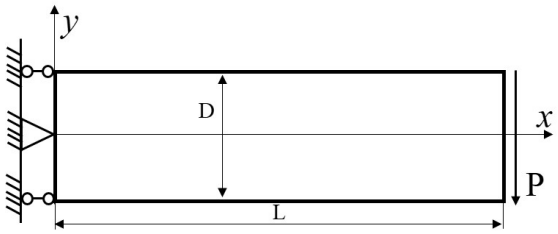

Figure 3.18: Schematic of the Timoshenko beam problem.

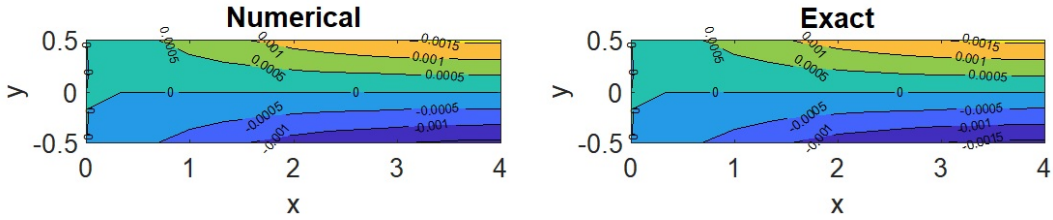

Figure 3.19: Comparison of the numerical result and exact result of displacement in x-direction.

ary conditions and natural boundary conditions are:

$$\begin{aligned} \boldsymbol{u} = \boldsymbol{g} &= \begin{bmatrix} \frac{Py}{6EI}(2+\nu)(y^2 - \frac{D^2}{4}) \\ -\frac{P\nu L}{2EI}y^2 \end{bmatrix} \\ \boldsymbol{\sigma}\cdot\boldsymbol{n} = \boldsymbol{h} &= \begin{bmatrix} 0 \\ -\frac{P}{2I}(\frac{D^2}{4} - y^2) \end{bmatrix} \end{aligned} \tag{3.71}$$

where D and L are the height and length of the beam. $I = \frac{D^3}{12}$ is the moment of inertia of the beam with unit thickness. The parameters used are $P = 1000$N,

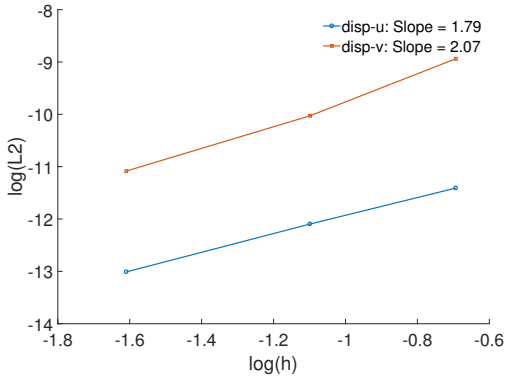

Figure 3.20: L2 norm for displacement in Timoshenko beam problem.

$E = 3 \times 10^7$Pa, $\nu = 0.3$, $D = 1$m, and $L = 4$m.

The exact solution of this problem is:

$$\boldsymbol{u} = \begin{bmatrix} \frac{Py}{6EI}[(6L - 3x)x + (2 + \nu)(y^2 - \frac{D^2}{4})] \\ -\frac{P}{6EI}[3\nu y^2(L - x) + (4 + 5\nu)\frac{D^2 x}{4} + (3L - x)x^2] \end{bmatrix} \tag{3.72}$$

The domain is discretized by 3×9, 4×13, and 6×21 nodes. 2×2 Gauss quadrature is applied. The rectangular kernel with support size $a = 1.75$ and linear basis are adopted for the RK approximation.

The numerical results of the displacement in x-direction are compared to exact values in Figure 3.19 for the case of the 4×13 nodes discretization, which agrees well. Figure 3.20 shows the L2 norm error of this approximation. The optimal convergence rate is achieved for y-displacement, with the rate for the x-displacement similar to the expected rate.

3.4 Conclusions

In this chapter, the methodology of reproducing kernel particle method (RKPM) is presented. The method is the combination of the reproducing kernel approximation and the Galerkin weak form of the partial differential equation at hand.

The RK approximation can be considered a corrected kernel estimate of SPH. The lack of Kronecker delta property requires other approaches to impose the essential boundary condition. Several approaches, like the transformation method, penalty method, Lagrangian multiplier and Nitsche's method were presented and

tested. The pros and cons of each method was compared and contrasted.

Several numerical examples were studied using this method. Namely, the 1-D approximation, 1-D PDE, 2-D approximation, 2-D PDE of the Poisson equation and the 2-D elasticity problem. Good agreement was made which verified the effectiveness and accuracy of the method, and in particular, good accuracy was achieved in simulation of small-strain elastic mechanics problems. This method will be used to model both small and large strain viscoelastic mechanics problems in later chapters.

Chapter 4
RKPM modeling of small-strain viscoelastic problems using the integral form

4.1 Introduction

Viscoelastic modeling is common in industry applications such as creep in concrete structures [56], polymer processing [57], food and drug manufacturing [58], among others. Viscoelastic modeling is employed to model the behavior of these materials which is time-dependent, and that they seem to have memory in that the current response is dependent on the entire history of loading.

The viscoelastic constitutive equation can be expressed in two different forms, namely differential form and convolution integral form. The differential form of the constitutive equation is derived from physical models in which the material response is related to a combination of elastic springs and viscous dashpots. For example, Zienkiewicz etc. [59] derived a differential form of constitutive equation from the generalized Kelvin model. In derivation of the stress-strain relation, the total strain is additively decomposed into an elastic part and viscous part.

The convolution integral form can be obtained in several ways. For example, by using principles of thermodynamics, Schapery [60] introduced a relaxation modulus and creep compliance, and decomposed them into initial and transient components to propose a generalized integral form for both stress relaxation and strain creep. Later, researchers used Prony series [61, 62] to represent the bulk modulus and

shear modulus in viscoelastic problems [63].

Alternatively, Simo and Hughes [31] used the generalized Maxwell model to obtain the integral form by integrating the differential form of the constitutive relation of each Maxwell elements. One problem associated with this model is the inadequacy of physical data for assigning material properties [59]. Thus, in applications, simpler models are typically used, like the Maxwell model, Kelvin model, or the standard solid model. One point worthy of being noted is that in their scheme, the volumetric/deviatoric decomposition used to do update the stress is trivial for 3 dimensional (3D) and plane strain problems, however, for plane stress problems, care must be taken in dealing with the out-of-plane strain component [64].

In recent decades, the finite element method (FEM) has been widely used to study viscoelastic problems. Differential form of constitute equations are implemented weakly in the same way as the momentum equation. Because of the stress splitting involved, mixed finite element formulations are extensively used, for instance, the elastic viscous stress splitting (EVSS), the discrete EVSS (DEVSS), and the discontinuous Galerkin (EVSS-G) or SUPG (EVSS-SUPG) stabilized form. For a detailed literature review of these formulations, see [65]. A direct solution to the integral form of viscoelastic constitutive equation at current step needs to store all the information at quadrature points from entire previous time steps which requires large memory storage [62]. So when using integral form of constitutive equation, a recursive integration method is adopted in which the current stress is only dependent on the information from the previous time step. It can tremendously reduce this storage limitation for simulation of large scale problems. In this chapter, an integral form of constitutive equation is used.

In recent years, meshfree methods have become more and more popular since compared to mesh based methods, they can deal with extremely large deformation problems, such as those involving free surface closure and formation, which would otherwise require remeshing. The smoothed particle dynamics (SPH) method is one of the earliest invented methods. Applications of SPH method to investigate viscoelastic problems can be found in, for example, [66,67]. In order to improve the consistency of kernel approximation, Liu etc. [16] proposed the reproducing kernel particle method (RKPM) by multiplying the kernel function with a correction function. RKPM has since been widely used in computational mechanics problems.

An important issue associated with meshfree methods is the instability problem coming form direct nodal integration [44, 68]. Gauss quadrature avoids the issue, but to make the method to be truly meshfree, a nodal integration method is superior. To deal with this issue, the stabilized conforming nodal integration (SCNI) [51] and stabilized non-conforming nodal integration (SNNI), for example, have been proposed by Chen et al. Another issue of this method is the lack of Kronecker Delta property. But it can be relatively easily resolved by transformation method [49], the Lagrange multiplier method [44], the penalty method [45], and the Nitsche's method [46–48], among others.

To the best of the authors' knowledge, this work is the first time viscoelastic problems are simulated under the RKPM framework. Here it is first presented in small strain regime, and the extension to large strains later in the text will demonstrate the advantages of meshfree methods to deal with very large deformation problems involving viscoelasticity.

The chapter is organized as follows. The problem statement of small-strain viscoelasticity is presented first, in which the governing equations and integral form of constitutive equation will be reviewed. This is followed by a brief description of the RKPM framework, including RK approximation and discretization equations. Next, some numerical examples are provided, followed by conclusions.

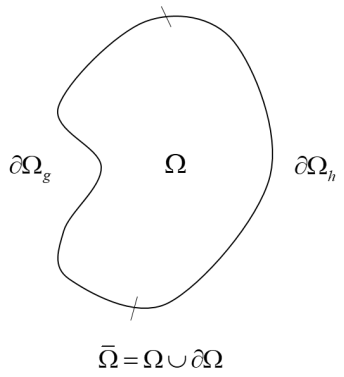

Figure 4.1: Schematic of the domain of 2D problem.

4.2 Problem statement

4.2.1 Governing equations of viscoelasticity

The model problem for present work is assumed to be quasi-static. That is, the governing equation is treated as being in equilibrium (ignoring the inertia effect), while the constitutive equation is time-dependent. In the context of continuum mechanics, the governing equation can be formulated as the classical boundary value problem:

$$\nabla \cdot \boldsymbol{\sigma} + \boldsymbol{b} = \mathbf{0} \quad \text{in } \Omega \tag{4.1a}$$

$$\boldsymbol{\sigma} \cdot \boldsymbol{n} = \boldsymbol{h} \quad \text{on } \partial\Omega_h \tag{4.1b}$$

$$\boldsymbol{u} = \boldsymbol{g} \quad \text{on } \partial\Omega_g \tag{4.1c}$$

where $\boldsymbol{b}$ is the body force on domain $\bar{\Omega}$ which is bounded by boundary $\partial\Omega$, $\boldsymbol{h}$ is the surface traction on the natural boundary $\partial\Omega_h$, $\boldsymbol{g}$ is the displacement on the essential boundary $\partial\Omega_g$, and $\boldsymbol{n}$ is the unit outer normal to the domain. The decomposition of the boundary satisfies $\partial\Omega = \partial\Omega_g \cup \partial\Omega_h$ and $\partial\Omega_g \cap \partial\Omega_h = \varnothing$. An example of decomposition of 2D geometry is showed as Figure 4.1. Note that up to this point, the governing equation is the same, with the exception of how $\boldsymbol{\sigma}$ will be specified in relation to the strains and displacements.

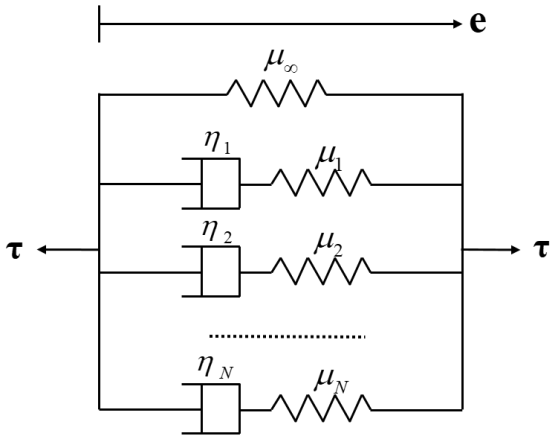

Figure 4.2: Generalized Maxwell model.

4.2.2 Constitutive equation

The bulk response of many viscoelastic materials is typically much stiffer than the deviatoric response, and thus the relaxation effect in bulk component can be ignored [31]. Based on this fact, the relaxation in bulk component will be neglected. However, if needed, viscoelasticity can be easily extended to obtain a bulk response, for example, see [69].

The integral form of constitutive equation for small strain problems used in the present work was derived based on the generalized Maxwell model [31]. The model is a parallel combination of n Maxwell elements and an elastic spring. A schematic view of the model in 1-dimensional space is depicted in Figure 4.2. The idea applies to 3-dimensional space where $\boldsymbol{\tau} = \text{dev}[\boldsymbol{\sigma}]$ and $\boldsymbol{e}$ are deviatoric stress and deviatoric strain tensor, and η_I and μ_I are the dynamic viscosity and shear modulus respectively. The derivation will be briefly reviewed.

First, the transient stress is considered to be the difference between initial stress and internal stress:

$$\boldsymbol{\sigma}(t) = \boldsymbol{\sigma^0}(t) - \sum_{I=1}^{N} \boldsymbol{q_I}(t) \tag{4.2}$$

where $\boldsymbol{q}_I = 2\mu_I \boldsymbol{\alpha}_I$ is an internal stress variable and $\boldsymbol{\alpha}_I$ is the inelastic or viscous strain at the corresponding dashpot.

The initial stress can be derived from the initial free energy. From the fact that most viscoelatic materials behave differently in bulk and deviatoric response, the initial stored energy can be additively expressed as:

$$W^0(\boldsymbol{\varepsilon}) = \bar{W}^0(\boldsymbol{e}) + U^0(\Theta) \tag{4.3}$$

where $\boldsymbol{e} = \text{dev}[\boldsymbol{\varepsilon}] = \boldsymbol{\varepsilon} - \frac{1}{3}\text{tr}[\boldsymbol{\varepsilon}]\mathbf{1}$ and $\Theta = \text{tr}[\boldsymbol{\varepsilon}]$ are deviatoric and volumetric strain in three-dimensional space, respectively. $\bar{W}^0$ and U^0 are the deviatoric and bulk potential energy, respectively.

The initial stress can then be expressed as:

$$\sigma^0_{ij} = \frac{\partial W^0}{\partial \varepsilon_{ij}} \tag{4.4}$$

The variable $\boldsymbol{q}_I$ can be solved for in the following manner. In the $I-$th element,

it is easy to first see

$$\boldsymbol{\tau}_I = 2\eta_I \dot{\boldsymbol{\alpha}}_I = 2\mu_I(\boldsymbol{e} - \boldsymbol{\alpha}_I) \tag{4.5}$$

Then, from Equation $(4.5)_2$ and the relation $\boldsymbol{q_I} = 2\mu_I \boldsymbol{\alpha}_I$, one can derive a first order ODE, and solve it to obtain the inelastic strain. After the internal stress is obtained, the transient stress in Equation (4.2) can be written in a integral form, which can be expressed as:

$$\boldsymbol{\sigma}(t) = U^{0'}(\Theta)\mathbf{1} + \int_{t_0}^{t} g(t-s)\frac{d}{ds}\{\mathrm{dev}[\partial_{\boldsymbol{e}}\bar{W}^0(\boldsymbol{e}(s))]\} \tag{4.6}$$

where the normalized relaxation function $g(t)$ is defined as:

$$g(t) = \gamma_\infty + \sum_{I=1}^{N} \gamma_I e^{-t/\lambda_I} \tag{4.7}$$

where $\lambda_I = \frac{\eta}{\mu}$ is the relaxation time for $I-$th Maxwell element, $\gamma_I = \frac{\mu_I}{\mu_0}$ is the elastic shear modulus fraction of $I-$th element of all the shear moduli $\mu_0 = \sum \mu_I$.

The integral form of the constitutive relation in Equation (4.6) is an analytical form, and it is not suitable in computer implementation. That is, numerical integration needs to be applied. Let a discretized time domain be $[T_0, T] = \cup[t_n, t_{n+1}], t_{n+1} = t_n + \Delta t_n$, using the semigroup property of exponential function and the recurrence relation between $\boldsymbol{\sigma}_n$ and $\boldsymbol{\sigma}_{n+1}$ [31], one reaches a corresponding discrete form of a stress update algorithm as:

$$\boldsymbol{\sigma}_{n+1} = U^{0'}(\Theta_{n+1})\mathbf{1} + \gamma_\infty \boldsymbol{S}^0_{n+1} + \sum_{I=1}^{N} \gamma_I \boldsymbol{h}^{(I)}_{n+1} \tag{4.8}$$

where γ_I is the shear modulus fraction of $I-$th spring, $\boldsymbol{S}^0_{n+1}$ is the initial elastic shear stress at time step n+1, and $\boldsymbol{h}^{(I)}_{n+1}$ is the transient shear stress at time step n+1 in the $I-$th element, which can be calculated by:

$$\boldsymbol{e}_{n+1} = \mathrm{dev}[\boldsymbol{\varepsilon}_{n+1}] \tag{4.9a}$$

$$\boldsymbol{S}^0_{n+1} = \mathrm{dev}[\partial_{\boldsymbol{e}}\bar{W}^0(\boldsymbol{e}_{n+1})] \tag{4.9b}$$

$$\boldsymbol{h}^{(I)}_{n+1} = \exp(-\Delta t_n/\lambda_I)\boldsymbol{h}^{(I)}_n + \exp(-\Delta t_n/2\lambda_I)(\boldsymbol{S}^0_{n+1} - \boldsymbol{S}^0_n) \tag{4.9c}$$

From Equation (4.8), one can see that the total stress is decomposed into three parts: the initial elastic bulk stress, the initial elastic shear stress at the single spring element and the unsteady shear stress from all Maxwell elements.

The stress update scheme can be explained in a similar way to return mapping algorithm used in viscoplasticity problems. Initially, the viscous strain is frozen and the stress state is assumed to be elastic, and then the viscous damper relaxes to the real state at which the real stress is calculated.

4.2.3 Algorithmic tangent moduli

In order for an incremental form, to calculate the stress, the algorithmic tangent moduli is needed, which can be obtained as taking the derivative of the discrete Equation (4.8) with respect to the strain $\boldsymbol{\varepsilon}_{n+1}$:

$$\mathbb{C}_{n+1} = \frac{\partial \boldsymbol{\sigma}_{n+1}}{\partial \boldsymbol{\varepsilon}_{n+1}} \tag{4.10}$$

Introducing a linear isotropic elastic material, that is:

$$\begin{aligned} U^0(\Theta) &= \frac{1}{2} K \Theta^2 \\ \bar{W}^0(\boldsymbol{e}) &= \mu \boldsymbol{e} : \boldsymbol{e} \end{aligned} \tag{4.11}$$

where K and μ are bulk and shear modulus of the material, respectively, and combining Equations (4.8), (4.9), (4.10) and (4.11), one can derive the algorithmic tangent moduli in tensorial form as:

$$\mathbb{C}_{n+1} = K \boldsymbol{I} \otimes \boldsymbol{I} + g^*(\Delta t_n)[2\mu(\mathbb{I} - \frac{1}{3}\boldsymbol{I} \otimes \boldsymbol{I})] \tag{4.12}$$

where $\boldsymbol{I}$ and $\mathbb{I}$ are second order and forth order identity tensor. $g^*(\Delta t_n) = \gamma_\infty + \sum \gamma_I \exp(-\Delta t_n / 2\lambda_I)$ is the algorithmic expression for the relaxation function. In arriving at Equation (4.12), the chain rule is used.

One is easy to see that for a numerical experiment, the algorithmic tangent moduli is constant if the time step Δt_n is unchanged. However, this does not mean that one can update the stress at time step t_{n+1} as simply as $\underline{\sigma}_{n+1} = \boldsymbol{D}\underline{\varepsilon}_{n+1}$ where the underlined variables represent the corresponding variables in Voigt notation.

In fact, from the stress update scheme in Equation (4.8) and (4.9), one can derive:

$$\sigma_{ij}^{n+1} = \sigma_{ij}^{n} + \mathbb{C}_{ijkl}\Delta\varepsilon_{kl}^{n+1} + \sum_{I=1}^{N} \gamma_I h_{ij}^{(I)n}[\exp(-\Delta t_n/\tau_I) - 1] \tag{4.13}$$

which tells us that the current stress depends on the current strain increment and the previous internal variables, which are inherited from earlier values. This explains the characteristic of viscoelastic materials of "memory".

From the expression of the algorithmic tangent moduli shown in Equation (4.12), one can also see that the relaxation term only happens in the shear parts which is consistent with the Generalized Maxwell model and the observed behavior of viscoelastic materials. Another finding is that, by expanding the series terms in the algorithmic tangent moduli, it yields that the moduli can be expressed in a series form similar to the Prony series form which is widely used in the literature.

4.2.4 Deviatoric and spherical decomposition of strain in plane stress problems

The deviatoric and volumetric decomposition should be consistent with the decomposition done in 3D state. Thus, the decomposition can be done in 3D state, and transferred to the 2D notation.

The tensorial form of the stress and strain can be denoted as:

$$\underline{\underline{\sigma}} = \begin{bmatrix} \sigma_{11} & \sigma_{12} & 0 \\ \sigma_{21} & \sigma_{22} & 0 \\ 0 & 0 & 0 \end{bmatrix}, \quad \underline{\underline{\varepsilon}} = \begin{bmatrix} \varepsilon_{11} & \varepsilon_{12} & 0 \\ \varepsilon_{21} & \varepsilon_{22} & 0 \\ 0 & 0 & \varepsilon_{33} \end{bmatrix} \tag{4.14}$$

The decomposition is then, for stress:

$$\text{sph}(\underline{\underline{\sigma}}) = \begin{bmatrix} \frac{1}{3}\sigma_{ii} & 0 & 0 \\ 0 & \frac{1}{3}\sigma_{ii} & 0 \\ 0 & 0 & \frac{1}{3}\sigma_{ii} \end{bmatrix}, \quad \text{dev}(\underline{\underline{\sigma}}) = \begin{bmatrix} \sigma_{11} - \frac{1}{3}\sigma_{ii} & \sigma_{12} & 0 \\ \sigma_{21} & \sigma_{22} - \frac{1}{3}\sigma_{ii} & 0 \\ 0 & 0 & -\frac{1}{3}\sigma_{ii} \end{bmatrix} \tag{4.15}$$

where $\sigma_{ii} = \sigma_{11} + \sigma_{22}$. And for strain:

$$\text{sph}(\underline{\underline{\varepsilon}}) = \begin{bmatrix} \frac{1}{3}\varepsilon_{ii} & 0 & 0 \\ 0 & \frac{1}{3}\varepsilon_{ii} & 0 \\ 0 & 0 & \frac{1}{3}\varepsilon_{ii} \end{bmatrix}, \quad \text{dev}(\underline{\underline{\varepsilon}}) = \begin{bmatrix} \varepsilon_{11} - \frac{1}{3}\varepsilon_{ii} & \varepsilon_{12} & 0 \\ \varepsilon_{21} & \varepsilon_{22} - \frac{1}{3}\varepsilon_{ii} & 0 \\ 0 & 0 & \varepsilon_{33} - \frac{1}{3}\varepsilon_{ii} \end{bmatrix} \tag{4.16}$$

where $\varepsilon_{ii} = \varepsilon_{11} + \varepsilon_{22} + \varepsilon_{33}$.

Under plane stress assumption, the strain component ε_{33} can be determined from the constraint that $\sigma_{33} = 0$. From the Equations (4.8) and (4.9), one can derive the expression for viscoelastic material as:

$$\varepsilon_{33} = \frac{-(K - \frac{2}{3}\mu_0 g^*)(\varepsilon_{11} + \varepsilon_{22}) - f}{K + \frac{4}{3}\mu_0 g^*} \tag{4.17}$$

with

$$f = \sum_{I=1}^{N} \gamma_I \exp(-\Delta t_n/\lambda_I) h_{33}^n - \sum_{I=1}^{N} \gamma_I \exp(-\Delta t_n/2\lambda_I) S_{33}^n \tag{4.18}$$

One can see that, for elastic material in which the internal variables are zeros and the relaxation function $g^* = 1$, the strain component reduces to:

$$\varepsilon_{33} = -\frac{\nu}{1-\nu}(\varepsilon_{11} + \varepsilon_{22}) \tag{4.19}$$

which is consistent with the elastic plane stress problem [64]. With these relations in hand, the strain decomposition can facilitate the stress update.

4.3 Numerical methodology

The basic of reproducing kernel approximation is presented in Section 3.2.1. The formulation starts from the weak form of the governing equation until the discrete matrix form of the system equation is constructed. Because of the linear nature of the constitutive model developed, in each load step, the incremental displacement can be solved in one step, however here, the general formulation is presented. The calculation continues until the total simulation time is reached.

4.3.1 RKPM formulation

4.3.1.1 Weak form

Assume that the configuration at time step t is known, then ones seeks to obtain the configuration at the next time step. By the virtual work principle, we have:

$$\int_\Omega \sigma_{ij}^{n+1}\delta\varepsilon_{ij}^{n+1}dV = \int_\Omega b_i^{n+1}\delta u_i^{n+1}dV + \int_{\partial\Omega_h} \bar{h}_i^{n+1}\delta u_i^{n+1}dS \tag{4.20}$$

Performing linearization, and introducing the RK approximation:

$$\Delta\boldsymbol{u}^h(\boldsymbol{x}) = \sum_{I=1}^{N} \Psi_I(\boldsymbol{x})\Delta\boldsymbol{d}_I \tag{4.21}$$

$$\delta\Delta\boldsymbol{u}^h(\boldsymbol{x}) = \sum_{I=1}^{N} \Psi_I(\boldsymbol{x})\delta\Delta\boldsymbol{d}_I \tag{4.22}$$

and the strain-displacement relation $\boldsymbol{\varepsilon}^n = \nabla^s(\boldsymbol{u}^n)$ where $\nabla^s(\boldsymbol{u}^n)$ is the symmetric part of the gradient of $\boldsymbol{u}^n$, we have the following discrete system to solve at the current step $n+1$:

$$\boldsymbol{K}_{n+1}(\Delta\boldsymbol{d}) = \boldsymbol{F}_{n+1}^{\text{ext}} - \boldsymbol{F}_n^{\text{int}} \tag{4.23}$$

where the stiffness matrix and the force vector are:

$$\begin{aligned}
\boldsymbol{K}_{n+1} &= \int_\Omega \boldsymbol{B}^T\boldsymbol{D}_{n+1}\boldsymbol{B}dV \\
\boldsymbol{F}_{n+1}^{\text{ext}} &= \int_\Omega \boldsymbol{\Psi}^T\boldsymbol{b}^{n+1}dV + \int_{\partial\Omega_h} \boldsymbol{\Psi}^T\bar{\boldsymbol{h}}^{n+1}dS \\
\boldsymbol{F}_n^{\text{int}} &= \int_\Omega \boldsymbol{B}^T\boldsymbol{\sigma}^n dV
\end{aligned} \tag{4.24}$$

where the material stiffness matrix $\boldsymbol{D}_{n+1}$ is the Voigt notation of the algorithmic tangent moduli $\mathbb{C}_{n+1}$, obtained from Equation (4.12). Iteration on (4.23) is performed until convergence. For linear models as in the present formulation, no iteration is needed.

In solving the system algebraic equations, the transformation method is used to alleviate the drawback of lacking Kronecker Delta property.

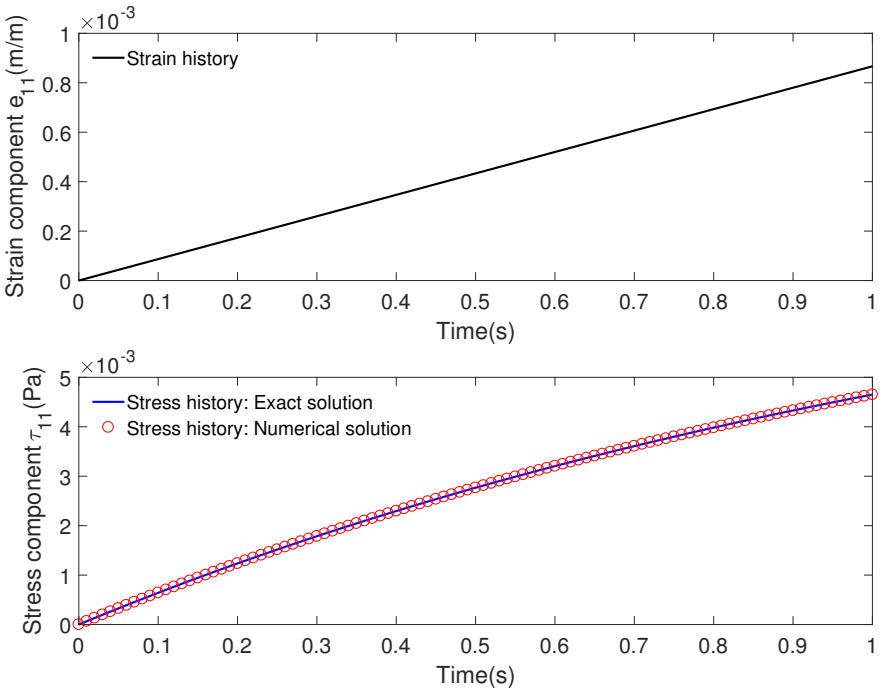

Figure 4.3: Results comparison for uni-axial tension example with $E = 10\text{Pa}, \eta = 5\text{Pa} \cdot \text{s}$.

4.4 Numerical Examples

Three numerical examples are used to verify the stress update algorithm and the numerical methodology. Firstly, a uniaxial tension example and a stress relaxation example are presented to validate the stress update algorithm, which are followed by the cantilever beam bending problem with tip load. In this work, the RKPM framework with Gauss integration is employed to study the viscoelastic problem.

4.4.1 Uniaxial tension example

In this example, the Maxwell element is used as the constitutive model. Two different cases are tested in which one case has a high relaxation time and the other has a low relaxation time to see how the material behaves under the same load. The material properties are $\eta = 5\text{Pa} \cdot \text{s}$ with $E = 10\text{Pa}$ and $E = 100\text{Pa}$ for the comparison. Unless stated explicitly, Poisson ratio is $\nu = 0.3$.

Suppose a bar is stretched purely uniaxially in the x-direction. The prescribed

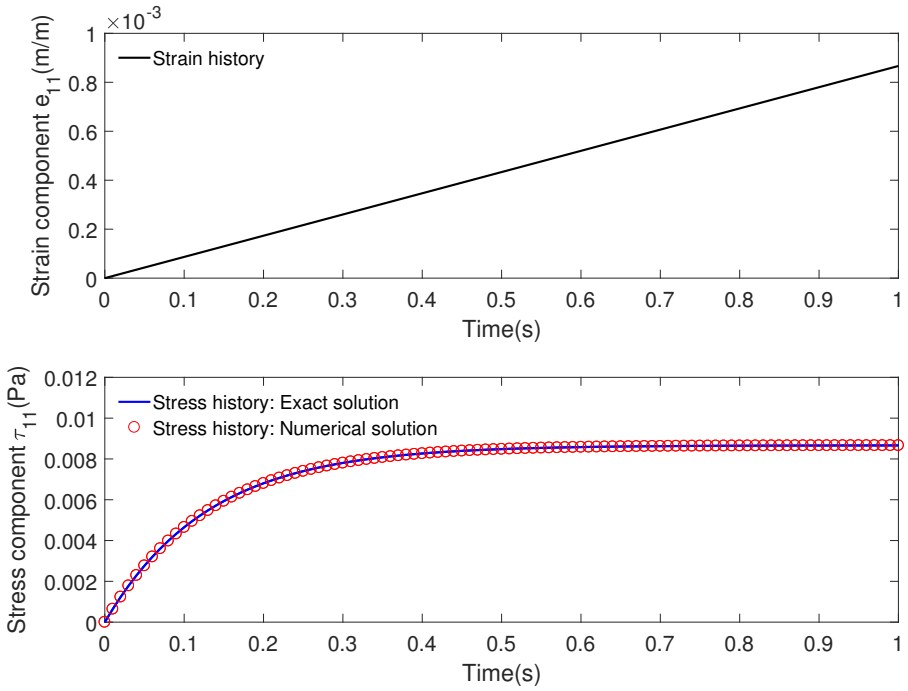

Figure 4.4: Results comparison for uni-axial tension example with $E = 100\text{Pa}, \eta = 5\text{Pa} \cdot \text{s}$.

uniaxial tensile strain is:

$$\varepsilon_{11} = \frac{t}{1000} \quad (0\text{s} \leq t \leq 1\text{s}) \tag{4.25}$$

The other two normal strains can be obtained by the Poisson effect, while all the shear strains are zero, thus one has $\varepsilon_{22} = \varepsilon_{33} = -\nu\varepsilon_{11}$.

The exact solution can be found by solving an ordinary differential equation, and can be obtained in a similar manner as Equation (4.5):

$$\dot{\boldsymbol{\tau}} + \frac{\boldsymbol{\tau}}{\lambda} = 2\mu\dot{\boldsymbol{e}} \tag{4.26}$$

The deviatoric strain component e_{11} is obtained from the relation:

$$e_{11} = \varepsilon_{11} - \frac{\varepsilon_{ii}}{3} = \frac{2(1+\nu)}{3}\varepsilon_{11} \tag{4.27}$$

With the initial condition $\tau_{11} = 0$ at $t = 0\text{s}$, the exact solution for the deviatoric

stress component τ_{11} is:

$$\tau_{11} = \frac{\eta(1+\nu)}{750}(1 - e^{-t/\lambda}) \tag{4.28}$$

where $\lambda = \frac{\eta}{\mu} = \frac{\eta}{E/2(1+\nu)}$ is the relaxation time.

The comparison between the numerical solution and exact solution of the deviatoric stress component τ_{11} in different cases are shown in Figure 4.3 and Figure 4.4. From the result, one can see very good agreement is made between the stress update algorithm and the exact solution.

Also, from the standpoint of material behavior, one can qualitatively verify the results. It is well known that dashpots needs time to initialize; that is, it can not react to stress with certain strain immediately like a spring does. So the elastic spring works first, then the dashpot takes effects gradually. What is more, if the spring is "more stiff" than the dashpot (easy to move), then the viscous dashpot will move easily. Otherwise, the elastic spring will tend to move more. This explains why the stresses at initial stage goes linearly with strain in both cases; while case 1 ($E = 10Pa$) is more elastic dominant and case 2 ($E = 100Pa$) is more viscous dominant (stress is near constant with the strain is increasing).

4.4.2 Stress relaxation example

A uniaxial stress relaxation problem is examined as the second example. The Maxwell element is still used as the constitutive model and the same material properties as the first example are employed here.

The prescribed strain in the x-direction is:

$$\varepsilon_{11} = \varepsilon_0 H(t - t_1) \tag{4.29}$$

where $\varepsilon_0 = 1 \times 10^{-3}$, $t_1 = 0.5$s and $H(t)$ is Heaviside function which equals to 1 when $t > 0$, otherwise it is zero. The other two normal strains can be obtained, again by the Poisson effect, again with the shear strains being zero.

With above initial condition, the exact solution for the deriatoric stress component τ_{11} can be obtained similar to before, and is expressed as:

$$\tau_{11} = \frac{4(1+\nu)\mu\varepsilon_0}{3} H(t - t_1) e^{-\frac{t-t_1}{\lambda}} \tag{4.30}$$

where the component e_{11} can be solved by Equation (4.27). In deriving the exact solution of Equation (4.30), the integration by parts technique is used.

The comparison between the numerical solution and exact solution is shown as Figure 4.5 and Figure 4.6. One can see that very good agreement is made between the stress update algorithm and the exact solution. Again, the same trend in material behavior is observed as the first example.

These two examples of constitutive modeling verified the stress update algorithm of the integral form of the viscoelasticity constitutive equation obtained from the generalized Maxwell model.

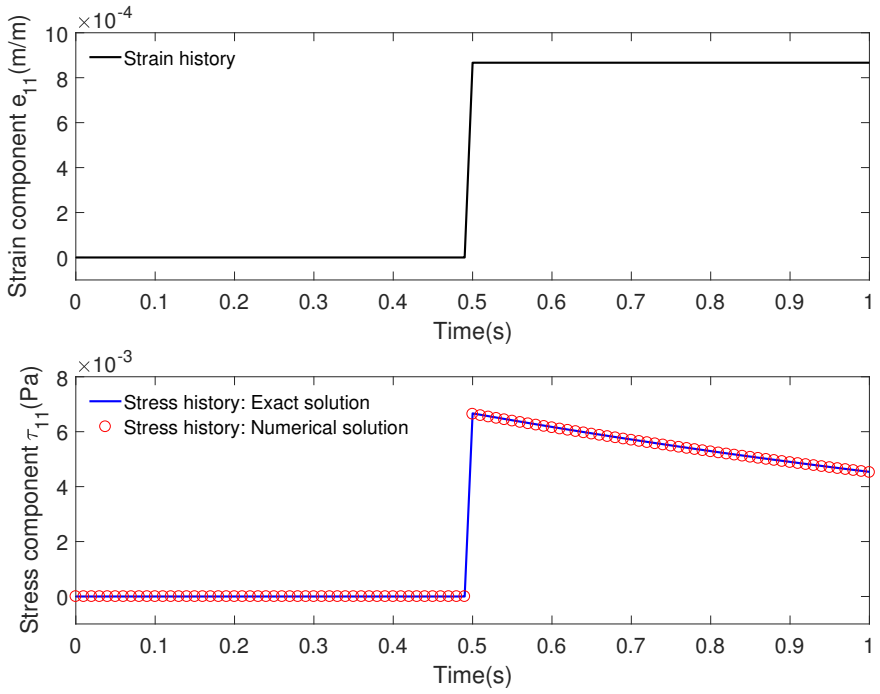

Figure 4.5: Results comparison for stress relaxation example with $E = 10\text{Pa}, \eta = 5\text{Pa} \cdot \text{s}$.

4.4.3 Cantilever beam with tip load

A 2-D cantilever beam of viscoelastic material under tip load under plane stress assumption is studied in this example. The geometry of the problem is displayed in Figure 4.7. The length of the beam is $L = 20\text{m}$ with a cross-section area $A = 1\text{m}^2$

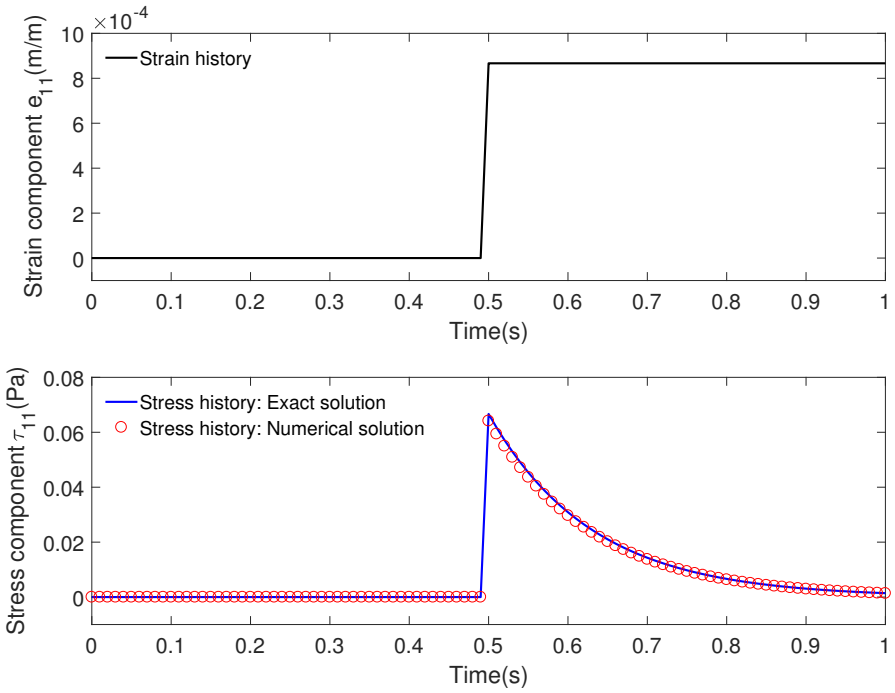

Figure 4.6: Results comparison for stress relaxation example with $E = 100\text{Pa}, \eta = 5\text{Pa} \cdot \text{s}$

(the width and height are both 1m). The load is given as:

$$P = P_0[H(t) - H(t - t_1)] \tag{4.31}$$

where $P_0 = 1\text{N}$ and the applied time of the load is $t_1 = 10\text{s}$.

The material model is the so-called standard solid model which is comprised of one Maxwell element in the generalized Maxwell model (see Figure 4.2). The values of the model are $E_\infty = 0.1\text{MPa}$, $E_1 = 0.4\text{MPa}$, and relaxation time $\lambda_1 = \frac{\eta_1}{\mu_1} = 1.0\text{s}$. Poisson's ratio is 0.3, and constant. The analytical solution of the response for the beam tip can be derived, which is [62]:

$$w_L = \frac{P_0 L^3}{3I}[D(t) - D(t - t_1)H(t - t_1)] \tag{4.32}$$

where I is the area moment of inertia of the beam. D is the creep compliance and defined as:

$$D(t) = D_0 + D_1(1 - e^{-t/\lambda}) \tag{4.33}$$

where

$$D_0 = \frac{1}{E_0}, \quad E_0 = E_\infty + E_1, \quad D_1 = \frac{1}{E_\infty} - \frac{1}{E_0}, \quad \lambda = \frac{E_0 \lambda_1}{E_\infty}. \tag{4.34}$$

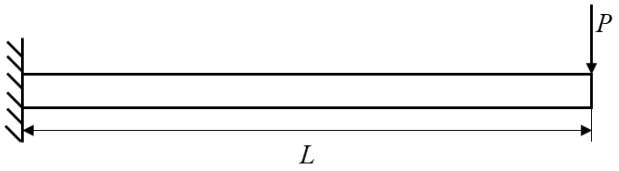

Figure 4.7: Schematic of the geometry of the cantilever beam with tip load.

It must be stressed that the analytical solution is derived based on the assumption that the relaxation effect happens on both bulk and deviatoric component. To verify the numerical method presented by this analytical solution, the constitutive relation needs also to be adjusted accordingly for the bulk part [69]. For this specific beam problem, the stress update scheme of the stress, and the bulk component are:

$$\boldsymbol{\sigma}_{n+1} = \gamma_\infty \boldsymbol{P}^0_{n+1} + \sum_{I=1}^{N} \gamma_I \boldsymbol{m}^{(I)}_{n+1} + \gamma_\infty \boldsymbol{S}^0_{n+1} + \sum_{I=1}^{N} \gamma_I \boldsymbol{h}^{(I)}_{n+1} \tag{4.35}$$

and

$$\Theta_{n+1} = \mathrm{tr}[\boldsymbol{\varepsilon}_{n+1}] \tag{4.36a}$$

$$\boldsymbol{P}^0_{n+1} = U^{0'}(\Theta_{n+1})\mathbf{1} \tag{4.36b}$$

$$\boldsymbol{m}^{(I)}_{n+1} = \exp(-\Delta t_n/\lambda_I)\boldsymbol{m}^{(I)}_n + \exp(-\Delta t_n/2\lambda_I)(\boldsymbol{P}^0_{n+1} - \boldsymbol{P}^0_n) \tag{4.36c}$$

where $\boldsymbol{P}^0_{n+1}$ is the initial elastic bulk stress and $\boldsymbol{m}^{(I)}_{n+1}$ the internal stress of $I-$th element. In the derivation, it has assumed that the relaxation time in bulk and shear component are the same.

The corresponding algorithmic tangent moduli and out-of-plane strain ε_{33} are:

$$\mathbb{C}_{n+1} = Kg^* \boldsymbol{I} \otimes \boldsymbol{I} + 2\mu g^* (\mathbb{I} - \frac{1}{3}\boldsymbol{I} \otimes \boldsymbol{I}) \tag{4.37}$$

and

$$\varepsilon_{33} = -\frac{(Kg^* - \frac{2}{3}\mu_0 g^*)(\varepsilon_{11} + \varepsilon_{22}) + f_1 + f_2}{Kg^* + \frac{4}{3}\mu_0 g^*} \tag{4.38}$$

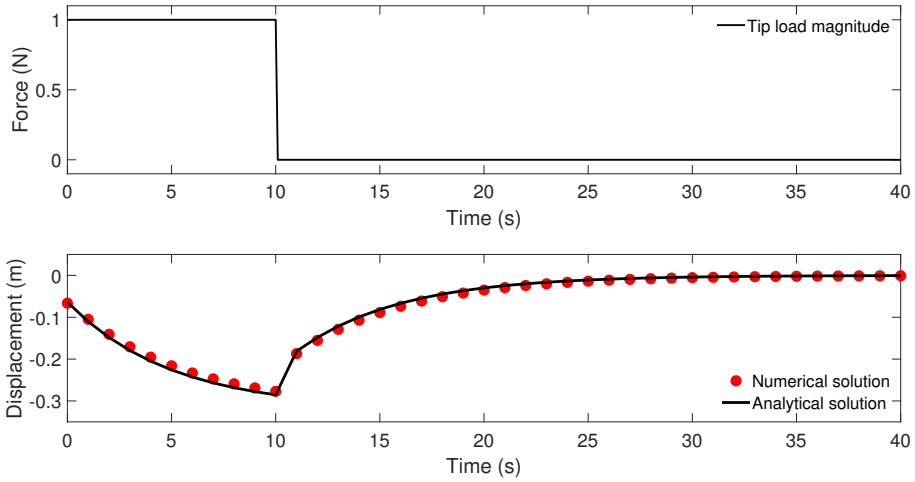

Figure 4.8: Result comparison of the tip y-displacement.

with the new term f_1 and f_2 being

$$\begin{aligned} f_1 &= \sum_{I=1}^{N} \gamma_I \exp(-\Delta t_n/\lambda_I) h_{33}^n - \sum_{I=1}^{N} \gamma_I \exp(-\Delta t_n/2\lambda_I) S_{33}^n \\ f_2 &= \sum_{I=1}^{N} \gamma_I \exp(-\Delta t_n/\lambda_I) m_{33}^n - \sum_{I=1}^{N} \gamma_I \exp(-\Delta t_n/2\lambda_I) p_{33}^n \end{aligned} \tag{4.39}$$

where m_{33}^n and p_{33}^n are the counterparts of the internal stress and initial bulk stress, in bulk component, to that of the shear components, respectively.

The discretization of the domain is performed with 41×3 nodes, with 2×2 Gauss quadrature employed for numerical integration. The time step used for iteration is 0.1s. The comparison between numerical result and the analytical solution of the tip displacement in the y-direction is shown in Figure 4.8, with good agreement obtained. In the time period $0 \leq t \leq 10$s, the creep phenomenon is observed. The beam relaxes to its original state gradually after the load is removed.

One can see that good agreement has been made for the overall trend of the relaxation processes in all the examples. The numerical framework presented is thus verified to be effective.

4.5 Conclusions

The integral form of viscoelastic constitutive relation is implemented under the RKPM framework in this chapter. To implement the stress update algorithm, the strain decomposition into volumetric and deviatoric component is necessary. It was considered that the relaxation effect happens in the shear component in the derivation, due to the fact the relaxation effect in bulk can be ignored for many real viscoelastic materials. However, it can be easily extended to the bulk component following the same fashion, as it was in the cantilever beam example.

Three numerical examples were tested to verify the implementation of the constitutive equation numerically. The results from uniaxial tension examples showed the effectiveness of the stress update scheme; with the help of reproducing kernel particle method (RKPM), the cantilever beam problem with tip load was studied. In order to compare the numerical result with the analytical solution, the extension of the relaxation effect to the bulk component of stress was performed. Very good agreement was made between the numerical and analytical solutions. These examples show that the numerical framework constructed in this chapter is effective for modeling small-strain viscoelastic problems.

Chapter 5
A large strain viscoelastic modeling by the reproducing kernel particle method

5.1 Introduction

For large strain viscoelasticity modeling, Green and Tobolsky [70] proposed a pioneering work based on multiplicative decomposition of the deformation gradient into volumetric and isochoric component motivated by the signifcant differece between bulk and deviatoric response of this type of material. Subsequently, Simo [71], Simo and Hughes [31], and Holzapfel [72] developed formulations based on decomposition. In these works, the internal state variable is used to track the history, origonating from Coleman and Gurtin [73]. A linear rate-type of the evolution equation of the internal variables was derived from a generalized Maxwell rheological model. Simo [71] also considered the damage effects. To consider the fully coupled thermo-mechanical response, Hozapfel and Simo derived a thermodynamically-consistent constitutive equation for thermoviscoelasticity [74]. Lubliner [75] extended this multiplication decomposition approach by further decomposing the isochoric deformation gradient into elastic and viscous components.

Numerical simulation of viscoelastic phenomena by conventional finite element method will encounter the locking problem because of near incompressibility. Multifield formulations are often employed to deal with this issue. For example, Holzapfel adopted the Hu-Washizu variational principle [72].

The constitutive laws are obtained by integrating the rate evolution equations in each Maxwell element. In order to numecially calculate the stress history, a recurrence relation [76] is adopted to avoid direct integration, which requires large memory storage for each quadrature point.

It should be noted that when performing time integration on the rate equations, not only objectivity should be satisfied, but also so-called incremental objectivity. The Hughes-Winget scheme [77] is one popular scheme to satisfy this condition. Another possibility is to simply use the material configuration stress measures and rates, and objectivity nor incremental objectivity are necessary [31].

For extremely large, finite strains, such as in problems like material deposition in 3D printing, the Lagrangian finite element method will encounter mesh distortion and entanglement issues which can even stop the simulation. Meshfree methods, on the other hand, are adept at modeling these types of problems. The reproducing kernel particle method (RKPM) [16], a popular meshfree method invented in the 90s, is adept at dealing with this situation.

This work is developed based on a truly meshfree method on the quadrature level: using nodal integration, in which the typical route of using Gauss quadrature which employs a mesh, is not used for numerical integration. In order to obtain stable results, the stabilized non-conforming nodal integration (SNNI) method [52] is implemented. For very large deformation problems with free surface formation and closure, the mapping between undeformed configuration and the deformed configuration is no longer one-to-one. The semi-Lagranginan formulation proposed by Guan et. al. [7, 78] is adopted to deal with the issue, in which approximations and the Lagrangian formulation only employs the current configuration as its basis. This numerical framework has been coded in the Penn State in-house meshfree explicit galerkin analysis (MEGA) program [79].

This chapter is organized as follows. The problem statement of dynamic viscoelastic finite strain problem is first introduced. The governing equations and integral form of the constitutive equations are then presented to close the system of governing equations. This is followed by a brief description of the RKPM framework, including discretization process, stabilization techniques, and time integration. Next, a large-strain viscoelastic drop test is simulated to demonstrate the effectiveness in modeling large deformation viscoelastic problems, and concluding remarks are given.

5.2 Governing equations for large-strain viscoelastic mechanics

5.2.1 Strong form

The governing equations in the context of continuum mechanics with dynamic response can be formulated as a classical initial boundary value problem. Cast in the current configuration, we have:

$$\rho\ddot{\boldsymbol{u}} = \nabla_{\boldsymbol{x}} \cdot \boldsymbol{\sigma} + \boldsymbol{b} \quad \text{in } \Omega \times [0,T] \tag{5.1a}$$

$$\boldsymbol{\sigma} \cdot \boldsymbol{n} = \boldsymbol{h} \quad \text{on } \partial\Omega_h \times [0,T] \tag{5.1b}$$

$$\boldsymbol{u} = \boldsymbol{g} \quad \text{on } \partial\Omega_g \times [0,T] \tag{5.1c}$$

$$\boldsymbol{u}(0) = \boldsymbol{u}_0 \quad \text{in } \Omega, t = 0 \tag{5.1d}$$

$$\dot{\boldsymbol{u}}(0) = \dot{\boldsymbol{u}}_0 \quad \text{in } \Omega, t = 0 \tag{5.1e}$$

where $\boldsymbol{u}$ is the displacement field, $\boldsymbol{\sigma}$ the Cauchy stress tensor, ρ the density at current configuration, $\boldsymbol{b}$ the body force per unit volume on the current domain $\bar{\Omega}$ which is bounded by boundary $\partial\Omega$, $\boldsymbol{h}$ is the current surface traction on the natural boundary $\partial\Omega_h$, $\boldsymbol{g}$ is the current displacement on the essential boundary $\partial\Omega_g$, and $\boldsymbol{n}$ is the unit outer normal to the current domain. The initial condition for displacement and velocity is given by $\boldsymbol{u}_0$ and $\dot{\boldsymbol{u}}_0$. The decomposition of the boundary satisfies $\partial\Omega = \partial\Omega_g \cup \partial\Omega_h$ and $\partial\Omega_g \cap \partial\Omega_h = \varnothing$. The operator $\nabla_{\boldsymbol{x}} = \partial_{\boldsymbol{x}} = \frac{\partial}{\partial \boldsymbol{x}}$ is the gradient operator in the spatial configuration.

5.2.2 Weak form

To derive the weak form of the problem, the space for trial solutions is defined as:

$$\mathbb{S} = \{\boldsymbol{u} : \bar{\Omega} \to \mathbb{R}^{n_{sd}} | \boldsymbol{u} \in [H^1]^{n_{sd}}, \boldsymbol{u}|_{\partial\Omega_g} = \boldsymbol{g}\} \tag{5.2}$$

The corresponding space for test functions is:

$$\mathbb{V} = \{\boldsymbol{w} : \bar{\Omega} \to \mathbb{R}^{n_{sd}} | \boldsymbol{w} \in [H^1]^{n_{sd}}, \boldsymbol{w}|_{\partial\Omega_g} = \boldsymbol{0}\} \tag{5.3}$$

Introducing the weight function and substituting into the weighted residual formulation yields:

$$\int_{\Omega_{\boldsymbol{x}}} \boldsymbol{w} \cdot (\nabla_{\boldsymbol{x}} \cdot \boldsymbol{\sigma} + \boldsymbol{b} - \rho \ddot{\boldsymbol{u}}) d\Omega = 0 \tag{5.4}$$

Using integration by part and Gauss Theorem into Equation (5.4), one can obtain the weak form of the governing equation as: find $\boldsymbol{u} \in \mathbb{S}$ such that for any $\boldsymbol{w} \in \mathbb{V}$,

$$\int_{\Omega_{\boldsymbol{x}}} w_{i,j} \sigma_{ij} d\Omega + \int_{\Omega_{\boldsymbol{x}}} w_i \rho \ddot{u}_i d\Omega - \int_{\Omega_{\boldsymbol{x}}} w_i b_i d\Omega - \int_{\partial \Omega_h x} w_i h_i dS = 0 \tag{5.5}$$

always holds.

5.2.3 Constitutive equation

Before describing the large strain constitutive law, the multiplicative split of the deformation gradient [80] needs to be introduced. The deformation gradient is defined as:

$$\boldsymbol{F} = \frac{d\boldsymbol{x}}{d\boldsymbol{X}} \tag{5.6}$$

The volumetric and deviatoric multiplicative decomposition of the deformation gradient is performed as [31]:

$$\boldsymbol{F} = \boldsymbol{F}^{\text{vol}} \boldsymbol{F}^{\text{dev}} \tag{5.7}$$

where the volumetric component $\boldsymbol{F}^{\text{vol}}$ and deviatoric component $\boldsymbol{F}^{\text{dev}}$ are defined as:

$$\begin{aligned} \boldsymbol{F}^{\text{vol}} &= J^{\frac{1}{3}} \boldsymbol{I} \\ \boldsymbol{F}^{\text{dev}} &= \bar{\boldsymbol{F}} = J^{-\frac{1}{3}} \boldsymbol{F} \end{aligned} \tag{5.8}$$

where $J = \det \boldsymbol{F}$ is the determinant of the deformation gradient and $\boldsymbol{I}$ is the identity tensor. It is easy to see that $\det \bar{\boldsymbol{F}} = 1$ which is why the deviatoric component is also called volume-preserving component.

The right Cauchy-Green strain tensors associated with Equation (5.8) is:

$$\begin{aligned} \boldsymbol{C} &= \boldsymbol{F}^T \boldsymbol{F} \\ \bar{\boldsymbol{C}} &= \bar{\boldsymbol{F}}^T \bar{\boldsymbol{F}} \end{aligned} \tag{5.9}$$

which will be used in the large strain viscoelastic constitutive equation.

The extension of the constitutive law from small strain to large strain in material configuration is simple, provided that the same generalized Maxwell model is adopted. In this work, the bulk response is considered to be purely elastic and no relaxation effect is taken into account.

Similarly, the initial free-energy function of the material is assumed to be:

$$W^0(\boldsymbol{C}) = U^0(\Theta) + \bar{W}^0(\bar{\boldsymbol{C}}) \tag{5.10}$$

where $\Theta \equiv J$. The functions U^0 and $\bar{W}^0$ define the initial volumetric and volume-preserving contributions to the stored-energy function.

Differentiating the free energy with respect to the Lagrange strain gives the initial 2nd PK stress:

$$\boldsymbol{S}^0 = 2\partial_{\boldsymbol{C}} W^0(\boldsymbol{C}) = JU^{0'}(\Theta)\boldsymbol{C}^{-1} + J^{-\frac{2}{3}}\mathrm{DEV}[2\partial_{\bar{\boldsymbol{C}}}\bar{W}^0(\bar{\boldsymbol{C}})] \tag{5.11}$$

The unsteady 2nd PK stress is the difference of initial stress and the time dependent internal stresses:

$$\boldsymbol{S}(t) = \boldsymbol{S}^0(t) - J^{-\frac{2}{3}}\mathrm{DEV}[\sum_{i=1}^{N}\boldsymbol{Q}_i] \tag{5.12}$$

where the internal stress $\boldsymbol{Q}_i$ satisfies the linear rate form of evolution equation:

$$\begin{aligned} \dot{\boldsymbol{Q}}_i(t) + \frac{1}{\tau_i}\boldsymbol{Q}_i &= \frac{\gamma_i}{\tau_i}\mathrm{DEV}\{2\partial_{\bar{\boldsymbol{C}}}\bar{W}^0[\bar{\boldsymbol{C}}(t)]\} \\ \lim_{t\to-\infty}\boldsymbol{Q}_i &= \boldsymbol{0} \end{aligned} \tag{5.13}$$

The solution of this first order ordinary differential equation is:

$$\boldsymbol{Q}_i(t) = \frac{\gamma_i}{\tau_i}\int_{-\infty}^{t}\exp[-(t-s)/\tau_i]\mathrm{DEV}\{2\partial_{\bar{\boldsymbol{C}}}\bar{W}^0[\bar{\boldsymbol{C}}(t)]\}ds \tag{5.14}$$

And thus the formula for 2nd PK stress is deduced by substituting Equation (5.14) into Equation (5.12):

$$\boldsymbol{S}(t) = JU^{0'}(\Theta)\boldsymbol{C}^{-1} + J^{-\frac{2}{3}}\int_{-\infty}^{t} g(t-s)\frac{d}{ds}(\mathrm{DEV}\{2\partial_{\bar{\boldsymbol{C}}}\bar{W}^0[\bar{\boldsymbol{C}}(s)]\})ds \tag{5.15}$$

where the relaxation function is $g(t) = \gamma_\infty + \sum_{i=1}^{N}\gamma_i\exp(-t/\tau_i)$.

Finally, here we recall the push-forward operation between the Kirchhoff stress and second PK stress to facilitate calculations in the current configuration:

$$\boldsymbol{\sigma} = \frac{1}{J}\boldsymbol{\tau} = \frac{1}{J}\boldsymbol{F}\boldsymbol{S}\boldsymbol{F}^T \tag{5.16}$$

where $\boldsymbol{\tau}$ is the Kirchhoff stress tensor.

5.3 Numerical methodology

The reproducing kernel particle method is employed as the numerical framework for the dynamic large strain viscoelastic modeling. The basic of reproducing kernel approximation has already been presented in Section 3.2.1. The Galerkin formulation, stabilized non-conforming nodal integration scheme, the time integration scheme and the numerical stress update scheme will next be presented.

5.3.1 Galerkin formulation

Applying the RK approximation to both trial and test functions, one obtains:

$$\begin{aligned} \boldsymbol{u}^h &= \sum_I^{Np} \boldsymbol{\Psi}_I \boldsymbol{D}_I = \boldsymbol{N}\boldsymbol{D} \\ \boldsymbol{w}^h &= \sum_I^{Np} \boldsymbol{\Psi}_I \boldsymbol{W}_I = \boldsymbol{N}\boldsymbol{W} \end{aligned} \tag{5.17}$$

where $\boldsymbol{N}$ is the assembled matrix for shape functions of each node, with linear basis employed here. $\boldsymbol{D}$ and $\boldsymbol{W}$ are vectors containing nodal coefficients. The construction of these shape functions for finite-strain problems will be discussed later in the text.

Substituting the approximation functions into the Equations in (5.5) leads to the following semi-discrete system equation [38]:

$$\boldsymbol{M}\ddot{\boldsymbol{u}} = \boldsymbol{F}^{\text{ext}} - \boldsymbol{F}^{\text{int}} \tag{5.18}$$

where the matrices and vectors are:

$$\begin{aligned} \boldsymbol{M} &= \int_{\Omega} \rho \boldsymbol{N}^T \boldsymbol{N} d\Omega \\ \boldsymbol{F}^{\text{ext}} &= \int_{\Omega} \boldsymbol{N}^T \boldsymbol{b} d\Omega - \int_{\partial\Omega_h} \boldsymbol{N}^T \boldsymbol{h} dS \\ \boldsymbol{F}^{\text{int}} &= \int_{\Omega} \boldsymbol{B}^T \boldsymbol{\sigma} d\Omega \end{aligned} \tag{5.19}$$

where $\boldsymbol{B}$ is the strain-displacement matrix, which is obtained by the strain displacement kinematic relation. The Voigt notation is used for the stress vector $\boldsymbol{\sigma}$ as well as the other matrices and vectors.

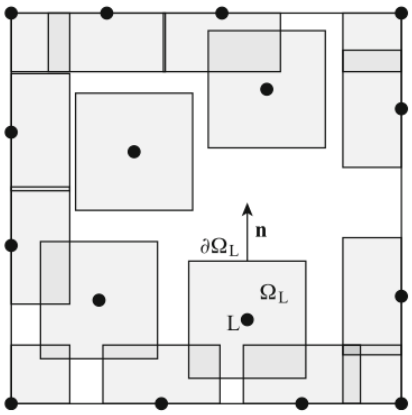

Figure 5.1: The smoothing domain in SNNI [6].

5.3.2 Stabilized non-conforming nodal integration (SNNI)

Direct nodal integration (DNI) suffers from low convergence rates, poor accuracy and rank instability. To alleviate the problems associated with DNI, Chen et. al. proposed the stabilized conforming nodal integration (SCNI) [51]. But for problems with large strain or fragmentation, reconstructing conforming domain continuously is difficult. Instead, the non-conforming counterpart is proposed in [52]. The schematic of employing non-conforming domains is showen in Figure 5.1.

In SNNI, the gradient is calculated in a smoothed way in which the smoothed gradient operator $\tilde{\nabla}$ is defined as:

$$\tilde{\nabla}(\cdot)|_{\boldsymbol{x_L}} = \frac{1}{V_L} \int_{\Omega_L} \nabla(\cdot) d\Omega = \frac{1}{V_L} \int_{\partial\Omega_L} (\cdot) \boldsymbol{n} dS \tag{5.20}$$

where $\boldsymbol{x_L}$ is the nodal point, V_L the volume of the domain and Ω_L the smoothing domain. The gradient on a node is smoothed in the domain and then the domain integral is converted to a surface integral using the divergence theorem.

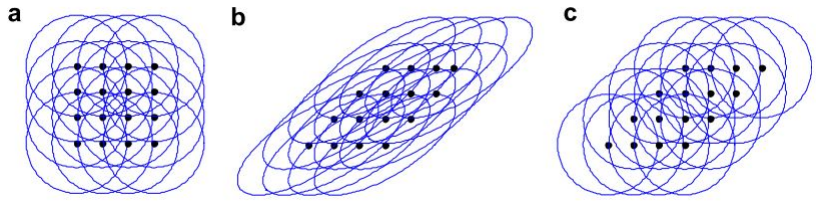

Figure 5.2: The comparison between Lagrangian and semi-Lagrangian kernel [7]: (a) undeformed configuration, (b) Lagrangian kernel, and (c) semi-Lagrangian kernel.

5.3.3 Lagrangian and semi-Lagrangian formulation

For the Lagrangian reproducing kernel function, the shape function is constructed based on the undeformed configuration. While for semi-Lagrangian, the shape function is constructed in the deformed configuration [78]. A comparison of the Lagrangian and semi-Lagrangian approximations is schematically shown in Figure 5.2. One can see that for Lagrangian RK, the kernel is deformed with the material and thus each node has the same neighbors throughout the computation. But for semi-Lagrangian, the kernel is undeformed to allow for different neighbors pass through the kernel, and disassociation, and reassociation is possible.

The shape function of the reproducing kernel approximation in the Lagrangian formulation is constructed as:

$$\Psi_I(\boldsymbol{X}) = \boldsymbol{H}^T(\boldsymbol{0})\boldsymbol{M}^{-1}(\boldsymbol{X})\boldsymbol{H}(\boldsymbol{X}-\boldsymbol{X}_I)\phi_a(\boldsymbol{X}-\boldsymbol{X}_I) \tag{5.21}$$

where $\boldsymbol{X}$ is the material point in the undeformed configuration.

Using the Lagrangian RK shape function with updated Lagrangian formulation, the spatial derivative of shape function which is required by the discretization of the equation of motion is computed as:

$$\frac{\partial \Psi_I(\boldsymbol{X})}{\partial \boldsymbol{x}} = \frac{\partial \Psi_I(\boldsymbol{X})}{\partial \boldsymbol{X}}\frac{\partial \boldsymbol{X}}{\partial \boldsymbol{x}} = \Psi_I(\boldsymbol{X})_{,\boldsymbol{X}}\boldsymbol{F}^{-1} \tag{5.22}$$

where the deformation gradient $\boldsymbol{F}$ can be numerically calculated as:

$$\boldsymbol{F} = \frac{\partial \boldsymbol{x}}{\partial \boldsymbol{X}} = \frac{\partial(\boldsymbol{X} + \boldsymbol{u})}{\partial \boldsymbol{X}} = \boldsymbol{I} + \sum_I \boldsymbol{\Psi}_I(\boldsymbol{X})_{,\boldsymbol{X}} \boldsymbol{u}_I \tag{5.23}$$

Or, in index form, it can be denoted as:

$$F_{ij} = \delta_{ij} + \sum_I \Psi_{I,X_j} u_{Ii} \tag{5.24}$$

Then $\boldsymbol{F}^{-1}$ can be solved directly from the inversion of $\boldsymbol{F}$. However, it breaks down if $\boldsymbol{F}$ is not invertible, which may happen when the mapping is no longer one-to-one in surface closure or surface generation, in very large deformation problems. Instead, the semi-Lagrangian formulation can be adopted to deal with this issue.

The shape function in semi-Lagrangian formulation is constructed as :

$$\Psi_I(\boldsymbol{x}) = \boldsymbol{H}^T(\boldsymbol{0}) \boldsymbol{M}^{-1}(\boldsymbol{x}) \boldsymbol{H}(\boldsymbol{x} - \boldsymbol{x}_I) \phi_a(\boldsymbol{x} - \boldsymbol{x}_I) \tag{5.25}$$

where $\boldsymbol{x}$ is the spatial point in the deformed configuration, and $\boldsymbol{x}_I \equiv \boldsymbol{x}(\boldsymbol{X}_I)$. Thus the particles follow the motion of the material, while the influence is defined in the spatial configuration.

In this case, the deformation gradient (if desired) can be calculated numerically in the following way. Recall the deformation mapping as:

$$\boldsymbol{x} = \boldsymbol{X} + \boldsymbol{u} \tag{5.26}$$

One can get the inverse of the deformation gradient then directly as:

$$\begin{aligned} \boldsymbol{F}^{-1} &= \frac{\partial \boldsymbol{X}}{\partial \boldsymbol{x}} = \frac{\partial(\boldsymbol{x} - \boldsymbol{u})}{\partial \boldsymbol{x}} \\ &= \boldsymbol{I} - \frac{\partial \boldsymbol{u}}{\partial \boldsymbol{x}} \\ &= \boldsymbol{I} - \sum_I \boldsymbol{\Psi}_I(\boldsymbol{x})_{,\boldsymbol{x}} \boldsymbol{u}_I \end{aligned} \tag{5.27}$$

or in the index form,

$$F^{-1}_{ij} = \delta_{ij} - \sum_I \Psi_{I,x_j} u_{Ii} \tag{5.28}$$

With the inverse of deformation gradient at hand, one can get the deformation

gradient to do the stress update procedure necessary for material laws defined in the undeformed configuration such as the viscoelastic laws presented here.

5.3.4 Boundary treatment

Typically, large deformation meshfree problems employ the semi-Lagrangian formulation, in which contact is naturally induced by kernel overlap. In the drop test problem to be presented, the test is characterized by contact, and for the Lagrangian formulation, a special treatment for contact should be introduced. That is, since the algorithm searches neighbors and calculates the shape functions and the derivatives once, at the beginning of the computation, a special boundary treatment should be implemented to allow for the contact.

Toward this end, a spring boundary condition treatment is proposed which is similar to the widely used repulsive force boundary in SPH [81]. The advantage of using this boundary condition is that it keeps the merit of Lagrangian formulation which just calculates the shape function and the derivatives once and thus saves computing time.

The idea is that when a drop particle approaches to the boundary of the wall (rigid in the y-direction here), a spring-like force exerts force on the particle to repulse it away. Physically, the force can be derived from a simple spring-mass analogy as:

$$f_y = K \cdot |y - y_c| \quad \text{if} \quad y < y_c \tag{5.29}$$

where f_y is the vertical repulsive force acting on a particle if the vertical coordinate y is lower than a critical height y_c, and K the spring stiffness.

For semi-Lagrangian formulation, the overlapping of kernels between particles induces repulsive force naturally which is called natural kernel contact [82], and thus no special treatment is needed unless a frictionless surface is desired, but this is not considered here.

It can be seen from the construction that the Lagrangian formulation is more computationally efficient, but tuning the spring constant is needed; while semi-Lagrangian formulation naturally realizes the contact, it is more computationally costly.

5.3.5 Time integration scheme

The explicit central difference time integration scheme is introduced using the Newmark-β algorithm ($\beta = 0$ and $\gamma = 1/2$) for the semi-discrete equation in Equation 5.18. The row-sum technique is used for a lumped mass to make the integration fully explicit.

The predictor-corrector algorithm for the time integration from a given time step t_n to t_{n+1} is carried out first by a predictor:

$$\begin{aligned} \tilde{\boldsymbol{d}}_{n+1} &= \boldsymbol{d}_n + \boldsymbol{v}_n \Delta t + \frac{\Delta t^2}{2} \boldsymbol{a}_n \\ \tilde{\boldsymbol{v}}_{n+1} &= \boldsymbol{v}_n + \frac{\Delta t}{2} \boldsymbol{a}_n \end{aligned} \tag{5.30}$$

based on the predicted physical values, then the generalized acceleration can be calculated from the momentum equation for each node. The corrector then is computed as:

$$\begin{aligned} \boldsymbol{d}_{n+1} &= \tilde{\boldsymbol{d}}_{n+1} \\ \boldsymbol{v}_{n+1} &= \tilde{\boldsymbol{v}}_{n+1} + \frac{\Delta t}{2} \boldsymbol{a}_{n+1} \end{aligned} \tag{5.31}$$

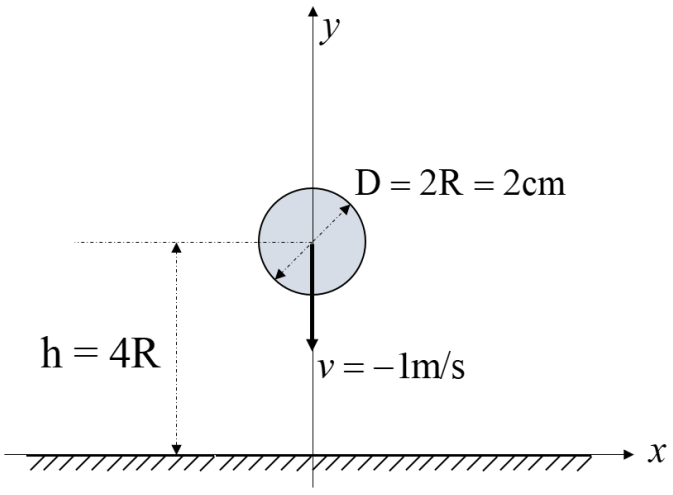

Figure 5.3: Schematic of the geometry of the drop test.

5.3.6 Stress update scheme

The classical strain driven technique is employed in this work, which results in a stress update scheme. The numerical procedure for this process is summarized as follows:

$$\begin{aligned} p_{n+1} &= U^{o'}(J) \\ \bar{\boldsymbol{\tau}}^0 &= \mathrm{dev}[2\bar{\boldsymbol{F}}_{n+1}\partial_{\bar{\boldsymbol{C}}}\bar{W}^0(\bar{\boldsymbol{C}}_{n+1})\bar{\boldsymbol{F}}_{n+1}^T] \\ \bar{\boldsymbol{h}}_n &= \sum_{I=1}^{N}\gamma_I \mathrm{dev}[\bar{\boldsymbol{F}}_{n+1}\widetilde{\boldsymbol{H}}_n^{(i)}\bar{\boldsymbol{F}}_{n+1}^T] \\ \boldsymbol{\tau}_{n+1} &= J_{n+1}p_{n+1}\boldsymbol{I} + g^*(\Delta t)\bar{\boldsymbol{\tau}}^0 + \bar{\boldsymbol{h}}_n \end{aligned} \tag{5.32}$$

where p_{n+1} is the bulk stress, $\bar{\boldsymbol{\tau}}^0$ the initial stress deviator of Kirchhoff stress, $\bar{\boldsymbol{h}}_n$ the internal shear stress, and $g^*(\Delta t_n) = \gamma_\infty + \sum \gamma_I \exp(-\Delta t_n/2\lambda_I)$ the algorithmic expression for the relaxation function. $\widetilde{\boldsymbol{H}}_n^{(i)}$ is a internal variable of $i-$th Maxwell element and can be updated as:

$$\begin{aligned} \widetilde{\boldsymbol{H}}_n^{(i)} &= \exp(-\Delta t_n/\tau_i)\boldsymbol{H}_n^{(i)} - \exp(-\Delta t_n/2\tau_i)\widetilde{\boldsymbol{S}}_n^0 \\ \widetilde{\boldsymbol{S}}_{n+1}^0 &= \bar{\boldsymbol{F}}_{n+1}^{-1}\bar{\boldsymbol{\tau}}^0\bar{\boldsymbol{F}}_{n+1}^{-T} \\ \boldsymbol{H}_{n+1}^{(i)} &= \widetilde{\boldsymbol{H}}_n^{(i)} + \exp(-\Delta t_n/2\tau_i)\widetilde{\boldsymbol{S}}_{n+1}^0 \end{aligned} \tag{5.33}$$

The neo-Hookean hyperelasticity law is introduced to calculate the initial stress:

$$\begin{aligned} U^o(J) &= \frac{1}{2}\kappa(\frac{J^2-1}{2} - \ln J) \\ \bar{W}^o(\bar{\boldsymbol{C}}) &= \frac{1}{2}\mu[\mathrm{tr}(\bar{\boldsymbol{C}}) - 3] \end{aligned} \tag{5.34}$$

where κ and μ are bulk and shear modulus, respectively. Then the initial elastic Kirchhoff stress can be derived by Equation (5.12) and a push-forward operation, which gives:

$$\boldsymbol{\tau}^o = \frac{\kappa}{2}(J^2-1)\boldsymbol{I} + \mu\mathrm{dev}(\bar{\boldsymbol{F}}\bar{\boldsymbol{F}}^T) \tag{5.35}$$

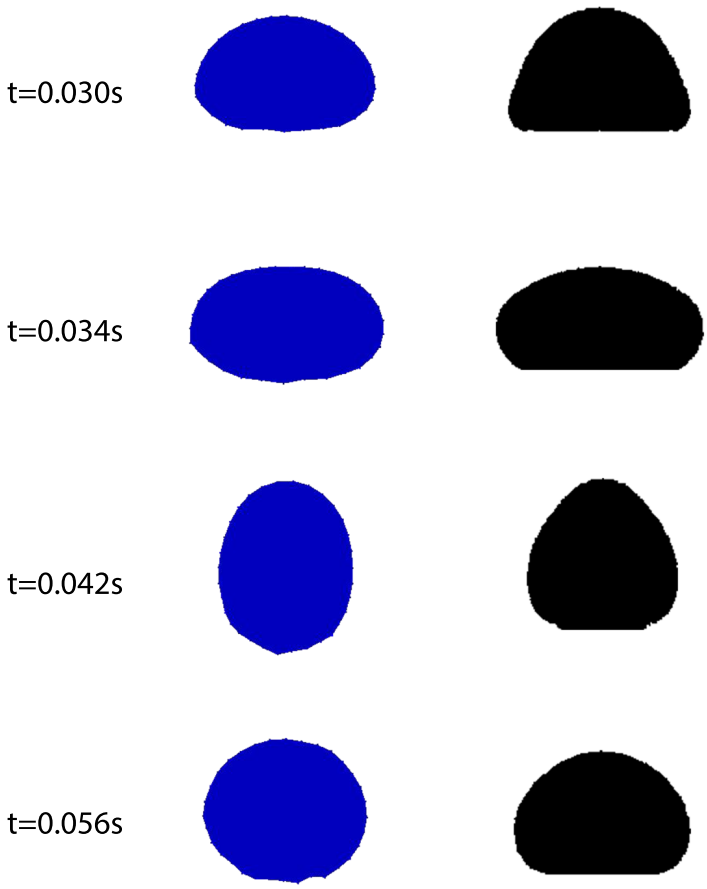

Figure 5.4: Comparison of drop test by semi-Lagrangian formulation with SPH result. Left: semi-Lagrangian; right: SPH [8].

5.4 Numerical example

A 3-D drop test of a viscoelastic material is studied in this example, taken from [8]. The geometry of the problem is shown in Figure 5.3. At the initial time, a drop with a diameter of $D = 0.02$m is above a rigid wall, with a height of $h = 2D$. The acceleration due to gravity is $g = -9.81\text{m/s}^2$ and acts on the body in the $y-$direction. The drop moves with an initial velocity v=1m/s downward at time $t = 0.0$s. The drop then moves downward and impacts with the rigid ground. The material model for the drop can be represented by a single Maxwell element which has a viscosity $\eta = 40\text{Pa} \cdot \text{s}$ and relaxation time $\lambda = 0.02$s. The Poisson's ratio

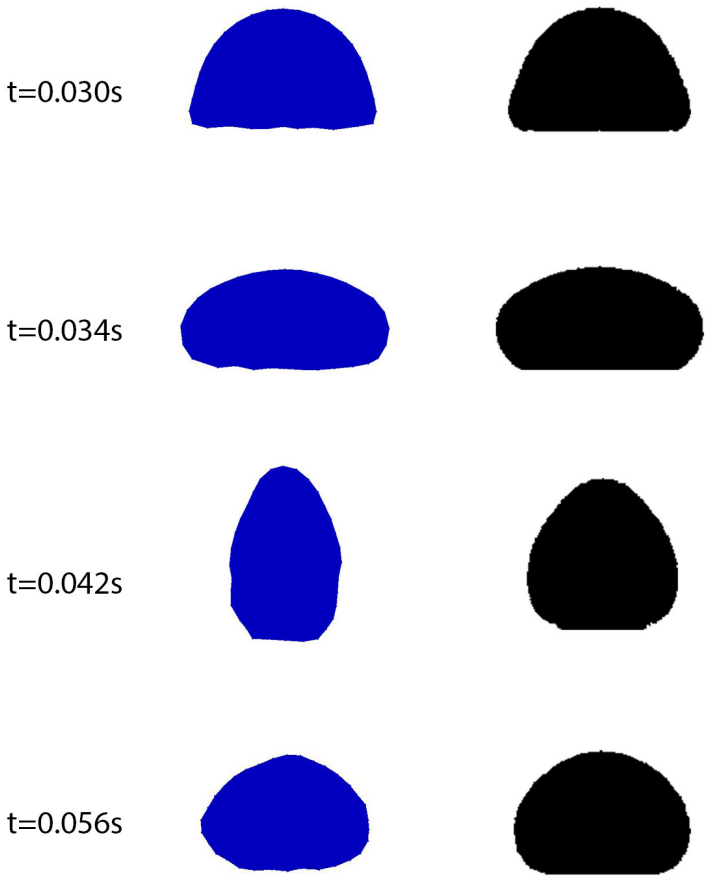

Figure 5.5: Comparison of drop test by Lagrangian formulation with SPH result. Left: Lagrangian; right: SPH [8].

is $\nu = 0.4$. A coarse discretization of the domain is employed with the particle spacing $dx = 0.002$m. In the MEGA setup, the $z-$direction is fixed to model this 2D plane-strain problem.

A small time step $\Delta t = 5 \times 10^{-6}$s for computation is set for semi-Lagrangian formulation in order to get stable result based on iteration of the simulation. The time history of the shape of the drop by semi-Lagrangian formulation is compared in Figure 5.4 to the reference results from Xu et.al using SPH [8]. For a viscoelastic material characterized by both viscous and elastic property, the drop bounces back, in contrast to that in a purely viscous drop, where there is no bounce back [8,83,84]. One can observe that the results from the current meshfree method agree well with

the referenced results. The current error comes from the computation of bulk force (or pressure). In the referenced SPH formulation, the pressure is treated nearly incompressible and solved by the state equation which assumes that the pressure is dependent on the density via an nearly incompressible equation of state. While in this work, the bulk force is purely elastic and computed directly through the hyperelastic constitutive equation with a high bulk modulus, although the explicit formulation limits the value of the modulus.

From this examples, it is found that using the Lagrangian formulation with the same time step as the semi-Lagrangian formulation, the drop blows up when it bounces back, which seems to indicate that it is more sensitive to the time step. In order to get stable results by Lagrangian formulation, the time step should be smaller than semi-Lagrangian counterpart. This may be due to the spring force introduced in the formulation, which adds an additional restriction on the time tep. In this case, the time step used was $\Delta t = 5 \times 10^{-8}$s. The spring constants used are $K = 50$N/m, $y_c = 0.001$m. Figure 5.5 shows the comparison of the shape profile during the motion. One can see that the overall shape agrees well with the SPH results except the one at time $t = 0.042$s. The simulation verifies the effectiveness of the proposed boundary treatment in the Lagrangian formulation. It is also observed that moderate oscillation happens in the simulation, and further stabilization may be needed [53].

Figure 5.6 shows the comparison of the width of the drop for the various formulations. In all the results, one can observe both increasing stage and decreasing stage, when the drop is impacting on the ground the width is expanded, while when bouncing back, the width shrinks. In contrast to the moderate change of the width of the drop by semi-Lagrangian formulation, it changes to a larger extent by the Lagrangian formulation.

Overall, the numerical results by both semi-Lagrangian and Lagrangian formulations match with the referenced results qualitatively for the shape, and the temporal history of the drop's width.

5.5 Discussion

The model developed in this chapter showed some effectiveness in dealing with the large strain viscoelastic problem, however, it does not mean it is sufficient enough

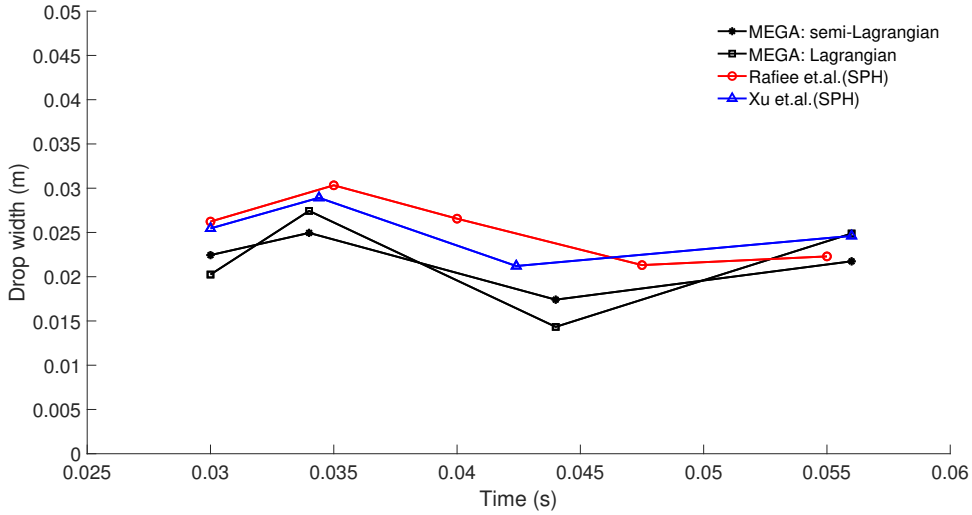

Figure 5.6: Comparison of the width of the drop.

for real modeling of concrete deposition. Several questions should be addressed before the real applications.

Firstly, the viscosity of the material in this work is time- and rate-independent, which is not the case in real application of concrete deposition process. In a long time scale like several hours elapsed in a circular wall sample printing, the constitutive law for concrete could be time- and rate-dependent as shown in Figure 2.7 and Figure 2.8 in Chapter 2. However, in a short time period as studied in this work (total simulation time is 0.056s), it is applicable to assume that it is rate- and time-independent. Thus, in this study with a short time simulation, the linear viscoelastic law is employed to model concrete deposition process, meaning we assume it obeys the Newtonian fluids law for the viscous part. However, for long time period modeling, it may not be suitable, under which circumstance, nonlinear viscoelastic laws could be used.

In addition, one can see that since the hyperelasticity is employed for the elastic stress computation, it inherits the disadvantage of using a free energy density, other than the neo-Hookean law adopted in this work, in a general form:

$$W = W(\boldsymbol{F}) \tag{5.36}$$

Which indicates that the calculation of the stress depends on the calculation of

deformation gradient $\boldsymbol{F}$. However, the mapping between the initial configuration and the current configuration does not exist any longer when two inter-layers close up together to become one layer during the deposition process. That is to say, the deformation gradient does not exist any longer in this case.

In order to model the deposition process in a large time scale, the material law employed cannot involve the deformation gradient. Namely, in calculation of the internal force or the Cauchy stress, the hyperelasticity laws can hardly be used for calculation of the elastic stress. The following extension of the Maxwell viscoelasticity law provides a possibility.

The true stress is decomposed into bulk and shear component as:

$$\boldsymbol{\sigma} = -p\boldsymbol{I} + \boldsymbol{\tau} \tag{5.37}$$

where p is the pressure and $\boldsymbol{\tau}$ is the shear stress. The pressure is calculated by the equation of state through the relation with density as $p = p(\rho)$ rather than from an energy density function $W(\boldsymbol{F})$, which can be denoted as [8]:

$$p(\rho) = \frac{\rho_0 c_0^7}{7}[(\frac{\rho}{\rho_0})^7 - 1] \tag{5.38}$$

where c_0 is the reference velocity.

The shear stress is calculated by:

$$\overset{\triangledown}{\boldsymbol{\tau}} + \frac{\boldsymbol{\tau}}{\lambda} = \mu\dot{\boldsymbol{\gamma}} \tag{5.39}$$

where the objective rate for the stress $\overset{\triangledown}{\boldsymbol{\tau}}$ should be used for large deformation problem and is expressed as:

$$\overset{\triangledown}{\boldsymbol{\tau}} = \frac{d\boldsymbol{\tau}}{dt} - \boldsymbol{L}^T\boldsymbol{\tau} - \boldsymbol{\tau}\boldsymbol{L} \tag{5.40}$$

where $\boldsymbol{L} = \frac{\partial \boldsymbol{v}}{\partial \boldsymbol{x}}$ is the spatial velocity gradient.

Equation (5.38) and (5.39), along with Equation (5.37) close the Maxwell model based viscoelastic constitutive relation for computation. One can see that this approach avoids using the deformation gradient.

Alternatively, other forms of viscoelasticity law could also be considered, for example, the power law [85], which is a nonlinear viscoelastic constitutive law.

Instead of Equation (5.39), the shear stress is calculated by:

$$\boldsymbol{\tau} = \eta(\dot{\gamma})\dot{\boldsymbol{\gamma}} \tag{5.41}$$

where $\eta(\dot{\gamma}) = K\dot{\gamma}^{n-1}$ indicates that the viscosity is dependent on the shear rate in a power law form with K being the consistency index, n the flow behavior index [86]. The pressure is also calculated through the equation of state [87]. When using this material law in real applications, the two material parameters, namely the consistency index K and the flow behavior index n need to be calibrated by experiment, which could be done through a shear test by a rheometer.

5.6 Conclusions

The integral form of finite strain viscoelastic constitutive relation is implemented under the RKPM framework in this work. The stress is considered to be the difference between the initial elastic stress and the internal stress. A hyperelastic material model is introduced to calculate the initial elastic stress at the finite strain regime. The constitutive law is cast in the material configuration in which the stress update scheme is carried out, and the state variables are pushed forward to the counterparts in spatial configuration, which avoids objectivity issues.

The updated Lagrangian formulation is adopted in this work and an explicit central difference time integration is chosen for temporal discretization. To formulate a truly meshfree method, the stabilized non-conforming nodal integration technique is used to circumvent the unstable results from direct nodal integration.

A drop test is studied by the numerical framework developed. The bouncing phenomenon is observed in this example which is the result of elastic portion of the material. The numerical results agree well with the results reported in literature, which verifies the effectiveness of the framework constructed. Some suggestions are put forward in order to model the actual 3D concrete printing.

Chapter 6
Conclusion

6.1 Conclusions

A numerical framework consisting of a viscoelastic constitutive relation based on the generalized Maxwell model and the reproducing kernel particle method is developed, aimed at modeling concrete behavior in the fresh state and solidified state. To model the creep or relaxation behavior of concrete structures at solidified state, the small strain version may be used; while for fresh concrete modeling, the large strain version should be chosen, and at extreme deformations, the semi-Lagrangian formulation should be employed rather than a pure Lagrangian formulation which would otherwise need special boundary treatment.

Several important points are observed:

1. The deviatoric and volumetric decomposition of strain/stress is a key ingredient of the modeling and stress update scheme of the viscoelastic model;

2. For small strain modeling with plane stress assumption, the out-of-plane strain component is essential in accurately computing the stress;

3. The large strain viscoelastic numerical framework stabilized by the SNNI algorithm is specially adept to model viscoelastic phenomenon in finite deformation and thus has the potential to model the deposition in 3D printing of fresh concrete mixtures.

6.2 Future directions

For a short time period modeling and thus in a short deposition process, the model developed is good enough to simulate the viscoelastic behavior of the concrete, since the assumption of constant elastic modulus and viscosity stand more valid and the merging interface is not considered in the short deposition process. However, as a preliminary study of 3D printing of concrete, the numerical framework built is not complete enough for modeling any actual concrete printing. The deficiencies of the study lie in the material model adopted and other factors:

- The model is not sufficient for large time scale and thus long time deposition process modeling as mentioned in Chapter 5. In this case, the elastic modulus and the viscosity are time-dependent. The later is also rate-dependent. When choosing or developing the proper material law, this condition should be considered;
- For actual concrete deposition process, the mapping between the initial configuration and the current configuration does not exist, and thus the hyperelastic-based viscoelasticity law does not work;
- The constitutive model is just based on the simple Maxwell element and purely numerical. In addition, the material parameters are not obtained by actual experiments;
- The constitutive law adopted is phenomenological in the macroscale but not physically or chemically driven in a microscale. It ignored the chemical hydration reaction which is the main driven factor that determines the macroscale viscosity and elastic modulus values;
- Only one constitutive law is considered in this work though there are many others as described in the literature review (Chapter 2). Whether which one is superior than another is not studied.

The limitations listed above also give suggestions for future work. Specifically, directions for future studies include:

- For long time period simulation, the equation of state can be adopted to calculate the bulk stress or pressure rather than the hyperelasticity law. This

kind of constitutive law (Maxwell model based or the power law) can also be studied and implemented;

- For actual concrete deposition modeling, the material model adopted should be calibrated by experiments which could help build a more accurate model for modeling of 3D concrete printing. Take the popular Bingham as an example. Prepare the concrete mixtures to be 3D printed and conduct rheological experiments by a rheometer in different time, for instance, in 1h, 2h, ... etc. The time history of viscosity and the yield stress values can be collected through the experiment. In this way, the rate-dependent and time-dependent relation could be determined;

- For actual modeling in a small time scale, experimental work is needed to find out the actual material parameters, for example, see ref [88]. The Maxwell model or the standard solid model is the most used form which can be reproduced from the generalized Maxwell model, and thus is enough for modeling. Since a lot more material parameters are needed to be fitted by experiments when using a more complicated network [59], it is not widely used;

- Control the viscoelastic material parameters and find an optimum mixture. It is reported that higher alkali content in the concrete mixture can highly decrease the value of elastic modulus and viscosity while a higher density of calcium can increase those values [88];

- Try other classical constitutive relations like the Bingham/viscoplastic law or the power law viscoelastic law to model the response of fresh concrete mixtures and make a comparison;

- Optimization of the printing variables involved in real 3D concrete printing;

- Microscale modeling of the chemical reaction by, for example, the molecule dynamics (MD) method to obtain material parameters like viscosity and elastic modulus;

- Multiscale modeling of the 3D concrete printing problem combining the chemical hydration and rheology.

Bibliography

[1] Khoshnevis, B. (2004) "Automated construction by contour craftingrelated robotics and information technologies," *Automation in construction*, **13**(1), pp. 5–19.

[2] Le, T. T., S. A. Austin, S. Lim, R. A. Buswell, R. Law, A. G. Gibb, and T. Thorpe (2012) "Hardened properties of high-performance printing concrete," *Cement and Concrete Research*, **42**(3), pp. 558–566.

[3] Lim, S., R. Buswell, T. Le, R. Wackrow, S. Austin, A. Gibb, and T. Thorpe (2011) "Development of a viable concrete printing process," *Proceedings of the 28th International Symposium on Automation and Robotics in Construction (ISARC2011)*, **2**, pp. 665–670.

[4] Colla, V. and E. Dini (2013) "Large scale 3D printing: From deep sea to the moon," *Low-Cost 3D Printing, for Science, Education & Sustainable Development; Canessa, E., Fonda, C., Zennaro, M., Eds*, pp. 127–132.

[5] Wangler, T., E. Lloret, L. Reiter, N. Hack, F. Gramazio, M. Kohler, M. Bernhard, B. Dillenburger, J. Buchli, N. Roussel, and R. Flatt (2016) "Digital Concrete: Opportunities and Challenges," *RILEM Technical Letters*, **1**, p. 67.

[6] Marcus, R., M. Hillman, and J. S. Chen (2013) "Corrected Stabilized Non-conforming Nodal Integration in Meshfree Methods," in *Meshfree Methods for Partial Differential Equations VI*, vol. 89, Springer, pp. 75–92.

[7] Guan, P. C., S. W. Chi, J. S. Chen, T. R. Slawson, and M. J. Roth (2011) "Semi-Lagrangian reproducing kernel particle method for fragment-impact problems," *International Journal of Impact Engineering*, **38**(12), pp. 1033–1047.

[8] Xu, X. and X. L. Deng (2016) "An improved weakly compressible SPH method for simulating free surface flows of viscous and viscoelastic fluids," *Computer Physics Communications*, **201**, pp. 43–62.

[9] Mehta, P. K. (2002) "Greening of the Concrete Industry for Sustainable Development," *Concrete International*, **24**(7), pp. 23–28.

[10] Miller, S. A., A. Horvath, and P. J. Monteiro (2018) "Impacts of booming concrete production on water resources worldwide," *Nature Sustainability*, **1**(1), p. 69.

[11] Lothenbach, B., T. Matschei, G. Möschner, and F. P. Glasser (2008) "Thermodynamic modelling of the effect of temperature on the hydration and porosity of Portland cement," *Cement and Concrete Research*, **38**(1), pp. 1–18.

[12] Stark, J. (2011) "Recent advances in the field of cement hydration and microstructure analysis," *Cement and Concrete Research*, **41**(7), pp. 666–678.

[13] Thomas, J. J., J. J. Biernacki, J. W. Bullard, S. Bishnoi, J. S. Dolado, G. W. Scherer, and A. Luttge (2011) "Modeling and simulation of cement hydration kinetics and microstructure development," *Cement and concrete research*, **41**(12), pp. 1257–1278.

[14] Scrivener, K. L., P. Juilland, and P. J. Monteiro (2015) "Advances in understanding hydration of Portland cement," *Cement and Concrete Research*, **78**, pp. 38–56.

[15] Marchon, D. and R. J. Flatt (2015) "Mechanisms of cement hydration," *Science and Technology of Concrete Admixtures*, **41**(12), pp. 129–145.

[16] Liu, W., S. Jun, and Y. Zhang (1995) "Reproducing kernel particle methods," *International journal for numerical methods in fluids*, **20**(8-9), pp. 1081–1106.

[17] Schiessel, H., R. Metzler, A. Blumen, and T. Nonnenmacher (1995) "Generalized viscoelastic models: their fractional equations with solutions," *Journal of physics A: Mathematical and General*, **28**(23), p. 6567.

[18] Mindess, S., J. F. Young, and D. Darwin (2003) *Concrete*, Prentice Hall.

[19] ASTM International (2013) "F2792-12a - Standard Terminology for Additive Manufacturing Technologies," *Rapid Manufacturing Association*, pp. 10–12.

[20] Bos, F., R. Wolfs, Z. Ahmed, and T. Salet (2016) "Additive manufacturing of concrete in construction: potentials and challenges of 3D concrete printing," *Virtual and Physical Prototyping*, **11**(3), pp. 209–225.

[21] Le, T. T., S. A. Austin, S. Lim, R. A. Buswell, A. G. Gibb, and T. Thorpe (2012) "Mix design and fresh properties for high-performance printing concrete," *Materials and Structures/Materiaux et Constructions*, **45**(8), pp. 1221–1232.

[22] Chhabra, R. P. (2010) "Non-Newtonian fluids: An introduction," *Rheology of Complex Fluids*, pp. 3–34.

[23] Ferraris, C. F. (1999) "Measurement of the rheological properties of high performance concrete: state of the art report," *Journal of research of the national institute of standards and technology*, **104**(5), p. 461.

[24] Wallevik, J. E. (2006) "Relationship between the Bingham parameters and slump," *Cement and Concrete Research*, **36**(7), pp. 1214–1221.

[25] Ferraris, C., F. De Larrard, and N. Martys (2001) "Fresh concrete rheology: recent developments," *Materials Science of Concrete VI, Amer. Cer. Soc. Ed. S. Mindess, J. Skalny*, pp. 215–241.

[26] Roussel, N. (2006) "A theoretical frame to study stability of fresh concrete," *Materials and structures*, **39**(1), pp. 81–91.

[27] Roussel, N., A. Gram, M. Cremonesi, L. Ferrara, K. Krenzer, V. Mechtcherine, S. Shyshko, J. Skocec, J. Spangenberg, O. Svec, L. N. Thrane, and K. Vasilic (2016) "Numerical simulations of concrete flow: A benchmark comparison," *Cement and Concrete Research*, **79**, pp. 265–271.

[28] Herschel, W. and R. Bulkley (1926) "Model for time dependent behavior of fluids," in *Proc. American Society of Testing Materials*, vol. 26, pp. 621–629.

[29] Patzák, B. and Z. Bittnar (2009) "Modeling of fresh concrete flow," *Computers and Structures*, **87**(15-16), pp. 962–969.

[30] Mechtcherine, V., A. Gram, K. Krenzer, J.-H. Schwabe, S. Shyshko, and N. Roussel (2014) "Simulation of fresh concrete flow using Discrete Element Method (DEM): theory and applications," *Materials and structures*, **47**(4), pp. 615–630.

[31] Simo, J. C. and T. J. Hughes (2006) *Computational inelasticity*, vol. 7, Springer Science & Business Media.

[32] Lewandowski, R. and B. Chorążyczewski (2010) "Identification of the parameters of the Kelvin–Voigt and the Maxwell fractional models, used to modeling of viscoelastic dampers," *Computers & structures*, **88**(1-2), pp. 1–17.

[33] Simo, J. C. (1987) "On a fully three-dimensional finite-strain viscoelastic damage model: formulation and computational aspects," *Computer methods in applied mechanics and engineering*, **60**(2), pp. 153–173.

[34] Jiang, T., J. Ouyang, Q. Li, J. Ren, and B. Yang (2011) "A corrected smoothed particle hydrodynamics method for solving transient viscoelastic fluid flows," *Applied Mathematical Modelling*, **35**(8), pp. 3833–3853.

[35] Crochet, M. J. and R. Keunings (1982) "Finite element analysis of die swell of a highly elastic fluid," *Journal of Non-Newtonian Fluid Mechanics*, **10**(3-4), pp. 339–356.

[36] Simo, J. and R. Taylor (1986) "A return mapping algorithm for plane stress elastoplasticity," *International Journal for Numerical Methods in Engineering*, **22**(3), pp. 649–670.

[37] Zienkiewicz, O. C., R. L. Taylor, O. C. Zienkiewicz, and R. L. Taylor (1977) *The finite element method*, vol. 36, McGraw-hill London.

[38] Bathe, K. J. (2006) *Finite element procedures*, Klaus-Jurgen Bathe.

[39] Hughes, T. J. (2012) *The finite element method: linear static and dynamic finite element analysis*, Courier Corporation.

[40] Chen, J. S., M. Hillman, and S. W. Chi (2017) "Meshfree Methods: Progress Made after 20 Years," *Journal of Engineering Mechanics*, **143**(4), p. 04017001.

[41] Li, S. and W. K. Liu (2002) "Meshfree and particle methods and their applications," *Appl. Mech. Rev.*, **55**(1), pp. 1–34.

[42] Gingold, R. A. and J. J. Monaghan (1977) "Smoothed particle hydrodynamics: theory and application to non-spherical stars," *Monthly notices of the royal astronomical society*, **181**(3), pp. 375–389.

[43] Lucy, L. B. (1977) "A numerical approach to the testing of the fission hypothesis," *The astronomical journal*, **82**, pp. 1013–1024.

[44] Belytschko, T., Y. Y. Lu, and L. Gu (1994) "Element-free Galerkin methods," *International journal for numerical methods in engineering*, **37**(2), pp. 229–256.

[45] Zhu, T. and S. Atluri (1998) "A modified collocation method and a penalty formulation for enforcing the essential boundary conditions in the element free Galerkin method," *Computational Mechanics*, **21**(3), pp. 211–222.

[46] Nitsche, J. (1971) "Über ein Variationsprinzip zur Lösung von Dirichlet-Problemen bei Verwendung von Teilräumen, die keinen Randbedingungen unterworfen sind," in *Abhandlungen aus dem mathematischen Seminar der Universität Hamburg*, vol. 36, Springer, pp. 9–15.

[47] Griebel, M. and M. A. Schweitzer (2003) "A particle-partition of unity method part V: boundary conditions," in *Geometric analysis and nonlinear partial differential equations*, Springer, pp. 519–542.

[48] Babuška, I., U. Banerjee, and J. E. Osborn (2003) "Meshless and generalized finite element methods: A survey of some major results," in *Meshfree methods for partial differential equations*, Springer, pp. 1–20.

[49] Chen, J. S., C. Pan, C. T. Wu, and W. K. Liu (1996) "Reproducing kernel particle methods for large deformation analysis of non-linear structures," *Computer methods in applied mechanics and engineering*, **139**(1-4), pp. 195–227.

[50] Beissel, S. and T. Belytschko (1996) "Nodal integration of the element-free Galerkin method," *Computer methods in applied mechanics and engineering*, **139**(1-4), pp. 49–74.

[51] Chen, J. S., S. Yoon, and C. T. Wu (2002) "A stabilized conforming nodal integration for Galerkin mesh-free methods," *International Journal for Numerical Methods in Engineering*, **53**(12), pp. 2587–2615.

[52] Chen, J. S., W. Hu, M. Puso, Y. Wu, and X. Zhang (2007) "Strain smoothing for stabilization and regularization of Galerkin meshfree methods," in *Meshfree Methods for Partial Differential Equations III*, Springer, pp. 57–75.

[53] Hillman, M. and J. S. Chen (2016) "An accelerated, convergent, and stable nodal integration in Galerkin meshfree methods for linear and nonlinear mechanics," *International Journal for Numerical Methods in Engineering*, **107**(7), pp. 603–630.

[54] Chen, J. S., M. Hillman, and M. Rüter (2013) "An arbitrary order variationally consistent integration for Galerkin meshfree methods," *International Journal for Numerical Methods in Engineering*, **95**(5), pp. 387–418.

[55] Fernández-Méndez, S. and A. Huerta (2004) "Imposing essential boundary conditions in mesh-free methods," *Computer Methods in Applied Mechanics and Engineering*, **193**(12-14), pp. 1257–1275.

[56] Bažant, Z. P. and S. Prasannan (1989) "Solidification theory for concrete creep. II: Verification and application," *Journal of engineering mechanics*, **115**(8), pp. 1704–1725.

[57] Li, Y., S. Tang, B. C. Abberton, M. Kröger, C. Burkhart, B. Jiang, G. J. Papakonstantopoulos, M. Poldneff, and W. K. Liu (2012) "A predictive multiscale computational framework for viscoelastic properties of linear polymers," *Polymer*, **53**(25), pp. 5935–5952.

[58] Ahmed, J. and H. S. Ramaswamy (2006) "Viscoelastic properties of sweet potato puree infant food," *Journal of Food Engineering*, **74**(3), pp. 376–382.

[59] Zienkiewicz, O. C., M. Watson, and I. P. King (1968) "A numerical method of visco-elastic stress analysis," *International Journal of Mechanical Sciences*, **10**(10), pp. 807–827.

[60] Schapery, R. (1969) "On the characterization of nonlinear viscoelastic materials," *Polymer Engineering & Science*, **9**(4), pp. 295–310.

[61] Haj-Ali, R. M. and A. H. Muliana (2004) "Numerical finite element formulation of the Schapery non-linear viscoelastic material model," *International Journal for Numerical Methods in Engineering*, **59**(1), pp. 25–45.

[62] Zocher, M. A., S. E. Groves, and D. H. Allen (1997) "A three-dimensional finite element formulation for thermoviscoelastic orthotropic media," *International Journal for Numerical Methods in Engineering*, **40**(12), pp. 2267–2288.

[63] Miled, B., I. Doghri, and L. Delannay (2011) "Coupled viscoelastic–viscoplastic modeling of homogeneous and isotropic polymers: Numerical algorithm and analytical solutions," *Computer Methods in Applied Mechanics and Engineering*, **200**(47-48), pp. 3381–3394.

[64] Simo, J. C. and R. L. Taylor (1986) "A return mapping algorithm for plane stress elastoplasticity," *International Journal for Numerical Methods in Engineering*, **22**(3), pp. 649–670.

[65] Baaijens, F. P. (1998) "Mixed finite element methods for viscoelastic flow analysis: A review," *Journal of Non-Newtonian Fluid Mechanics*, **79**(2-3), pp. 361–385.

[66] Ellero, M., M. Kröger, and S. Hess (2002) "Viscoelastic flows studied by smoothed particle dynamics," *Journal of Non-Newtonian Fluid Mechanics*, **105**(1), pp. 35–51.

[67] Ellero, M. and R. I. Tanner (2005) "SPH simulations of transient viscoelastic flows at low Reynolds number," *Journal of Non-Newtonian Fluid Mechanics*, **132**(1-3), pp. 61–72.

[68] Beissel, S. and T. Belytschko (1996) "Nodal integration of the element-free Galerkin method," *Computer Methods in Applied Mechanics and Engineering*, **139**(1), pp. 49–74.

[69] Nguyen, T. D. and S. Govindjee (2006) "Numerical study of geometric constraint and cohesive parameters in steady-state viscoelastic crack growth," *International Journal of Fracture*, **141**(1-2), pp. 255–268.

[70] Green, M. and A. Tobolsky (1946) "A new approach to the theory of relaxing polymeric media," *The Journal of Chemical Physics*, **14**(2), pp. 80–92.

[71] Simo, J. C. (1987) "On a fully three-dimensional finite-strain viscoelastic damage model: Formulation and computational aspects," *Computer Methods in Applied Mechanics and Engineering*, **60**(2), pp. 153–173.

[72] Holzapfel, G. A. (1996) "On large strain viscoelasticity: Continuum formulation and finite element applications to elastomeric structures," *International Journal for Numerical Methods in Engineering*, **39**(22), pp. 3903–3926.

[73] Coleman, B. D. and M. E. Gurtin (1967) "Thermodynamics with internal state variables," *The Journal of Chemical Physics*, **47**(2), pp. 597–613.

[74] Holzapfel, G. A. and J. C. Simo (1996) "A new viscoelastic constitutive model for continuous media at finite thermomechanical changes," *International Journal of Solids and Structures*, **33**(20-22), pp. 3019–3034.

[75] Lubliner, J. (1985) "A model of rubber viscoelasticity," *Mechanics Research Communications*, **12**(2), pp. 93–99.

[76] Taylor, R. L., K. S. Pister, and G. L. Goudreau (1970) "Thermomechanical analysis of viscoelastic solids," *International Journal for Numerical Methods in Engineering*, **2**(1), pp. 45–59.

[77] Hughes, T. J. R. and J. Winget (1980) "Finite rotation effects in numerical integration of rate constitutive equations arising in large deformation analysis," *International Journal for Numerical Methods in Engineering*, **15**(12), pp. 1862–1867.

[78] Guan, P. C., J. S. Chen, Y. Wu, H. Teng, J. Gaidos, K. Hofstetter, and M. Alsaleh (2009) "Semi-Lagrangian reproducing kernel formulation and application to modeling earth moving operations," *Mechanics of Materials*, **41**(6), pp. 670–683.

[79] Hillman, M., K. C. Lin, and A. Madra (2019) "The Meshfree Explicit Galerkin Analysis (MEGA) Code," , pp. 1–9.

[80] Truesdell, C. and W. Noll (1992) *The non-linear field theories of mechanics*, Springer.

[81] Crespo, A., M. Gómez-Gesteira, R. A. Dalrymple, et al. (2007) "Boundary conditions generated by dynamic particles in SPH methods," *CMC-TECH SCIENCE PRESS*, **5**(3), p. 173.

[82] Chi, S. W., C. H. Lee, J. S. Chen, and P. C. Guan (2015) "A level set enhanced natural kernel contact algorithm for impact and penetration modeling," *International Journal for Numerical Methods in Engineering*, **102**(3-4), pp. 839–866.

[83] Fang, J., R. G. Owens, L. Tacher, and A. Parriaux (2006) "A numerical study of the SPH method for simulating transient viscoelastic free surface flows," *Journal of Non-Newtonian Fluid Mechanics*, **139**(1-2), pp. 68–84.

[84] Rafiee, A., M. T. Manzari, and M. Hosseini (2007) "An incompressible SPH method for simulation of unsteady viscoelastic free-surface flows," *International Journal of Non-Linear Mechanics*, **42**(10), pp. 1210–1223.

[85] BAGLEY, R. L. (2008) "Power law and fractional calculus model of viscoelasticity," *AIAA Journal*, **27**(10), pp. 1412–1417.

[86] Rehm, B., A. Haghshenas, A. Paknejad, A. Al-Yami, J. Hughes, and J. Schubert (2012) "CHAPTER 2 - Flow Drilling: Underbalance Drilling with Liquid Single-Phase Systems," in *Underbalanced Drilling: Limits and Extremes*, Gulf Publishing Company, pp. 39 – 108.

[87] Bellini, A. (2002) *Fused Deposition of Ceramics : A Comprehensive Experimental , Analytical and Computational Study of Material Behavior , Fabrication Process and Equipment Design*, Ph.D. thesis, `arXiv:1011.1669v3`.

[88] Gholizadeh-Vayghan, A., F. Rajabipour, M. Khaghani, and M. Hillman (2019) "Characterization of viscoelastic behavior of synthetic alkalisilica reaction gels," *Cement and Concrete Composites*, **104**, p. 103359.